Quantitative technique analysis in XC-skiing

by

Øyvind Nøstdahl Gløersen

Thesis

for the degree of

Master of Science

(Master of Physics, Computational Physics programme)

UNIVERSITAS OSLOENSIS
MDCCCXI

Spring 2014

Abstract

Due to the complexity of human locomotion, a quantitative analysis of technique in sports is often difficult. For that reason a qualitative approach is most widespread, in particular amongst practitioners. The qualitative approach offers fast and individually adjusted feedback from a technical coach. However, it is also prone to bias due to the coaches (or researchers) prior assumptions. A quantitative approach is less prone to such bias.

This thesis suggests two different methods for a quantitative approach to technique analysis. Both methods are applied to a group of 6 elite cross country skiers using the V2 (or double dance) technique on a roller skiing treadmill. The methods are used to assess links between technique and performance, quantified by FIS-points.

The first method was an extensive analysis of the skiers 3D movement patterns, quantified by the coordinates of 41 markers positioned on the athletes skin and equipment. These markers determined the skiers *posture*. A dimensional reduction technique (PCA) was used to decompose the complex, but highly redundant set of postures into a comprehensible amount of uncorrelated variables. Each of these uncorrelated variables represented multi-segment movements, which could be visualized as movements by a stick figure. Also, the center of mass (COM) of the athletes were determined by a segment model based on the markers, which enabled an assessment of the effect of postural movements to whole body movements. Normalization and weighting procedures novel to the field of sports science enabled a direct comparison of the postural movements between athletes.

The second method used a much simpler approach, and consisted solely of measurements from an accelerometer and a gyroscope (both 3 axis) positioned at the athletes sacrum. The aim was to assess whether such a system could record interesting differences between athletes. If it could, the simplicity of the experimental setup, and the light weight of the sensor suggest that quantitative measurement of technique would be feasible both in regular training, and even in competition situations.

Both methods proved able to identify differences in skiing technique, even in a group consisting solely of elite skiers. Some of the differences appeared to relate to the FIS-point ranking of the athletes, which suggested that these features could be important for performance. In particular, the coordination between major hip flexor musculature and vertical COM motion appeared relevant, and suggested a more beneficial utilization of potential in the best ranked skiers. A second aspect appeared to be a preference in the best ranked skiers to use a smaller lateral COM excursion, which was closely linked to the axial rotation of the pelvis during the leg push.

Also included in this thesis are two appendices. Appendix A outlines the method used to obtain drift free measurements of displacements from the accelerometer and gyroscope output, and assess the accuracy of these measurements. Appendix B is included to show that sensors of similar specifications as those used in appendix A are incorporated in current marked smart phones, and investigates the possibility use smart phones as a tool for technique analysis.

Preface

In a way, the path towards this thesis started already seven or eight years ago. I met Jostein Hallén after a test race in Holmenkollen. Jostein was a professor in exercise physiology at the Norwegian School of Sport Science (NIH). He had recently developed an interest for inertial sensors, and wanted to see if this technology could be applied to technique analysis in skiing. I had just started to work on my bachelors degree in physics. As a physics student and a cross country skier, naturally this was compelling to me. We both agreed that it could be an interesting topic for a master's thesis. However, I also wanted to focus on my skiing, which implied that it would take some time to finish my bachelor's degree.

During my bachelor thesis, I spent very limited time on campus. However, one semester I had to take a course in experimental physics, which meant mandatory laboratory exercises. This course was held by professor Dag Kristian Dysthe. Again due to the skiing, I sometimes had to catch up to the other students by doing two lab exercises in one day. This meant longer days for me, and unfortunately for Dag, sometimes also for him. However, this also resulted in some contact between us. I mentioned to him the conversation with Jostein some years earlier, and I believe Dag was immediately interested. Even though this was quite far from his field as a geophysicist, Dag was willing to supervise such a thesis.

When I finally started work on my thesis, the NIH had already done quite a bit of work on inertial sensors. This work was done by Håvard Myklebust, currently PhD student at NIH. Luckily for me, there was still work that could be done. I believe the collaboration with Håvard has been beneficial for both sides: Håvard had already worked a lot with accelerometers, and put much thought into positioning of sensors and limiting constraints. I contributed by incorporating gyroscopic measurements, which resulted in a significant improvement of the measurement accuracy. This collaboration has resulted in a research article intended for publication. The aim of the article is a validation of the use of low cost inertial sensors for movement analysis. Håvard is first author on the paper, I contribute as a co-author. The material presented in appendix A represents my contribution to this paper. Chapter 4 of this thesis represents my interpretations and ideas on how to use the measurements obtained from the method presented in appendix A.

The data collection that forms the basis of all data in this thesis (with the exception of appendix B) was planned and conducted by both Håvard and myself.

During my time a the NIH, I also got into contact with Peter Federolf. Peter was then a post doc at NIH, now he is professor at the Norwegian University of Science and Technology. Peter and I have a similar background in physics, and immediately found a good tone. After the data collection I had a feeling that we did not utilize the dataset to its full potential.

Peter had extensive experience with the analysis of complex, multi-body systems, and had suggestions on how we could extract more information from the data set. The material presented in 3 is the result of this collaboration. This material also forms the foundation for a research article, which follows chapter 3 closely. I am first author on this article, but both the article and the contents of chapter 3 was strongly influenced by Peter and his earlier work.

I would like to express my gratitude to all of my supervisors, who all have contributed with with their experience and advice whenever I needed it. Håvard Myklebust was not an official supervisor of my thesis, but he definitely deserves the same acknowledgement. Finally, I express my gratitude to the athletes who participated in the study. Thank you for taking the time, and adjusting your training schedules to help me out with my thesis.

Oslo, June 11, 2014

Øyvind Nøstdahl Gløersen

Contents

List of Figures

List of Tables

Abbreviations

ASIS	Anterior Superior Iliac Spine
COM	Center of mass
DP	Double poling
FIS	International ski federation
FIS-points	Ranking system used by FIS
GPS	Global Positioning System
IMU	Inertial measurement unit
INS	Inertial navigation system
MEMS	Microelectromechanical system
PCA	Principal component analysis
PC	Principal component
pm	Principal movement
QTM	Qualisys Track Manager
RMS	Root mean square
S1	Os Sacrum
SA	Segment Analysis
SEM	Standard error of the mean
SIN	Strapdown Inertial Navigation
STD	Corrected sample standard deviation
XC	Cross Country

Symbols

General notation

x	Scalar quantity
$\mathbf{x}$	Vector quantity
$\mathbf{X}$	Matrix quantity
$\overline{x}$	Time mean of variable x
$\hat{x}$	Stride cycle mean of variable x
$\mathbf{X}^T$	Transpose of $\mathbf{X}$
$\dot{x}(t)$	First time derivative of x
$\ddot{x}(t)$	Second time derivative of x

Principal component analysis

$\mathbf{M}$	Measurement matrix
$\boldsymbol{\Xi}$	Measurement matrix after change of basis
$\boldsymbol{\Sigma}_{\mathbf{X}}$	Covariance matrix of $\mathbf{X}$
$\mathbf{PC}$	Principal components of $\mathbf{M}$
ξ_k	Column k of $\boldsymbol{\Xi}$
λ_k	Eigenvalue of $\mathbf{PC}_k$ vector
$\mathbf{p}$	Posture vector
$\mathbf{S}$	Scaling matrix
$\mathbf{w}$	Weight vector
$\mathbf{I}_n$	$n \times n$ identity matrix

Inertial navigation

$\mathbf{C}_b^l$	Direction Cosine relating the b-frame to the l-frame	
$\boldsymbol{\omega}^b$	Angular rate in the body frame	[rads^{-1}]
$\boldsymbol{\omega}^l$	Angular rate in the laboratory frame	[rads^{-1}]
$\mathbf{f}$	Specific force vector	[m/s^2]

$\boldsymbol{sigma}$	Angle vector	[rad]
$[\boldsymbol{\sigma}_{\times}]$	Skew symmetric form of vector $\boldsymbol{\sigma}$	

Technique features

α	Amplitude difference
τ	Timing difference
ϕ	None of the above (described in the text)

Chapter 1

Introduction: Technique and performance

The term *technique* is frequently used in sports, and refer to an athletes solution to a given task[1]. In this thesis *technique* is used to denote the specific movement pattern employed by athletes when conducting their sport. By this definition it is reasonable to assume that technique is a determinant for the success for an athlete, along with other determinants such as aerobic capacity, anaerobic capacity and maximal strength[2, 3].

This thesis investigates the relation between technique and performance. It might seem premature to assume that such a relation exists. For instance, Bartlett et al. [4] argued that movement variability and -adaptability are important factors for success, and that one should exert caution when finding relations between technique and performance. However, under the assumption that technique is a determinant of performance, it would be contradictory to assume that no such relations exist. Although some of the variations in technique might be the result of optimal athlete-specific adaptability, it is difficult to imagine this is the case for all variation in technique.

The scope of this thesis is limited to the XC skiing V2[5] technique, also referred to as G3[2] or 1-skate [6] in the literature, or double-dance amongst practitioners. One complete stride cycle of the V2 technique is shown in Figure 1.1. Qualitatively, the movement pattern is comprised of a sideways movement caused by an asynchronous leg push, and a symmetric poling movement that has twice the stride frequency. The duration and timing of the different propulsive phases has been described in the literature, for instance by Bilodeau et al. [6].

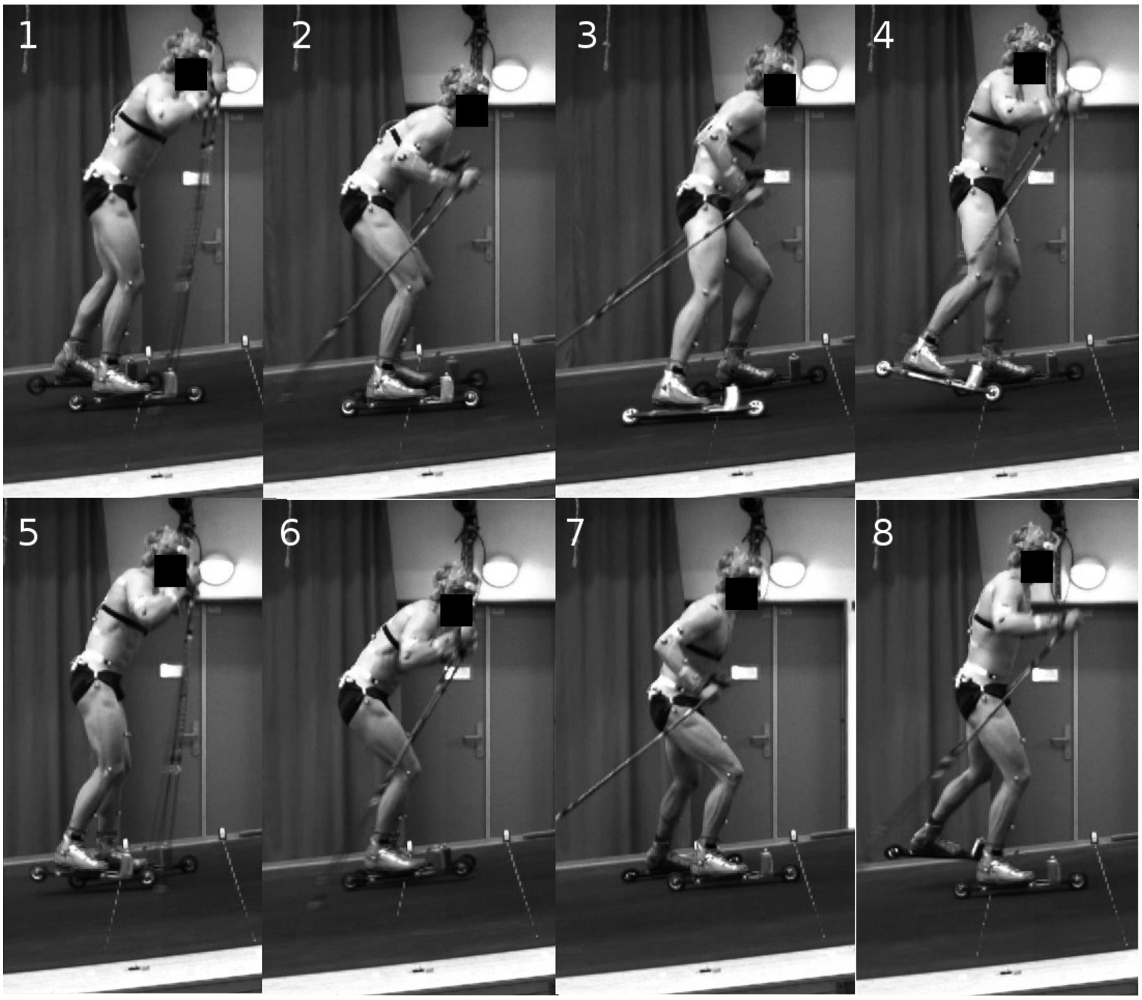

Figure 1.1: Example stride cycle of the V2 technique. Throughout this thesis, the upper left situation (poleplant on the right ski) is defined as the beginning and the end of each stride cycle

1.1 Previous studies on technique and performance in skiing

Several studies have investigated technique differences in the classical styles of cross country skiing such as double poling [7–11] and diagonal stride [12]. Fewer studies have investigated the skating techniques. General technique differences between V1 and V2 styles have been described [13], however, no detailed assessment is yet available that systematically investigates differences in the V2 skating techniques between elite cross country skiers.

From the studies on the classical techniques, the studies by Holmberg et al. [7], Stöggl and Holmberg [11] (double poling) and Lindinger et al. [12] (diagonal stride) all investigated relations between performance and technique. There are few similarities between the diagonal stride technique and skating techniques. On the other hand, double poling (DP, Figure 1.2) has a similar symmetric poling movement as the V2 technique. For that reason,

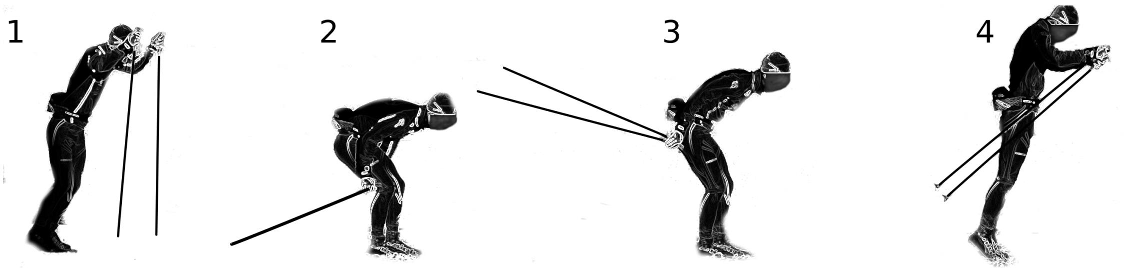

FIGURE 1.2: Example stride cycle of the classical double poling technique. This technique is *not* the topic of this thesis. However, due to the similarity of the poling action in the V2 technique (Fig. 1.1), some of the same basic principles may apply to both techniques

the results of Holmberg et al. [7] and Stöggl and Holmberg [11] might be of relevance for this thesis. The findings of these studies will be the topic for the next few paragraphs.

Holmberg et al. [7] tested a group of 11 athletes performing the DP-technique at 85% of their individual maximal velocity while rollerskiing on a treadmill. They measured selected joint angles, pole and plantar forces, cycle characteristics, and muscle activation (electromyography, EMG) of selected muscles. Furthermore, two different DP strategies were determined by a group of researchers from a 2D camcorder analysis of the skiers techniques. One strategy was characterized by *"more abducted*[1] *shoulder joints (character 1), smaller elbow angles at pole plant (character 2), faster (character 3), and more distinctly flexed elbow (character 4) and hip joints (characters 5 and 6) during an altogether more dynamic poling phase (character 7). This pattern was named "wide elbow" (WE) . . . "*[7, page 813]. The skiers that followed this strategy also included the faster skiers. The strategy that was opposite of these criteria was labelled the narrow elbow (NE) strategy.

Skiers using the WE strategy showed a higher relative pole force, a faster force development (time to peak pole force), and a higher relative force impulse. In addition to the elbow and shoulder differences described in the previous paragraph, the WE approach was also linked to a smaller knee and hip joint angle during the pole ground contact period, and a smaller hip joint angle at the time of pole plant. Finally, muscle activation patterns revealed that the WE approach was connected to a higher activation in Teres major, and a lower activation of Latissimus dorsi, compared to skiers who used the NE strategy.

Stöggl and Holmberg [11] tested sixteen male skiers at national and international level during double poling on a treadmill close to maximal intensity. They measured pole forces and 3D kinematics of skis and poles. Their findings included that faster skiers generated longer cycle lengths, and longer recovery phases (i.e. the time of no pole-ground contact) relative to the poling phase. The main determinant of maximal skiing velocity was the

---

[1] Readers that are not familiar with anatomical terminology are encouraged to consult chapter 2 for a short introduction to the terms necessary to follow the argumentation in this thesis.

duration of a "preparation phase" prior to the pole plant. The "preparation phase" was described qualitatively as:

"This phase was marked by almost a null velocity in the pole tip's resultant velocity, with the pole tip being 18.1 ± 7.2 cm above the treadmill at the end of the forward swing of the poles and in a horizontal direction 21.0 ± 9.6 cm ahead of the pole tip position at the pending pole plant. This instant was defined as the "preparation point". The subsequent backward and downward motion of the pole tip to the pole plant was defined as the "preparation phase," with a duration of 82 ± 31 ms."

The fastest skiers showed a distinct preparation phase, while slower skiers showed a less distinct or absent preparation phase (i.e. the preparation point coincided with the pole plant). The preparation phase was linked to a large impulse of pole forces, and a beneficial timing of the force evolution: A more distinct preparation phase correlated to a later peak pole force, and a smaller impact pole force relative to the peak force. This is beneficial because only a small fraction of the pole forces contribute to propulsion when the pole is directed approximately perpendicular to the ground (which the case at the pole plant), while it is more parallel to the ground later in the poling cycle[11, 14]. The peak pole force also correlated significantly to performance, but the correlation was less than that of the preparation phase duration.

In summary both studies emphasize the ability to produce a high force impulse, which facilitates a shorter poling period relative to the recovery period. The findings of the two studies propose slightly different approaches used by skiers to generate such higher impulses. The findings of Stöggl and Holmberg [11] suggest that a relatively low impact pole force, followed by a slow rate of force development to a high peak pole force is a beneficial approach. On the other hand, Holmberg et al. [7] found that the fastest skiers preferred the WE approach, which was connected to a short time to peak pole force[2]. Holmberg et al. [7] argued that the WE approach might lead to a higher loading on the poles due to a more accentuated lowering of the center of mass (due to smaller minimum hip and knee angles). On the other hand, Stöggl and Holmberg [11] argued that the aim should be to combine focus on high pole forces with appropriate timing of the forces, and that this was dependent on a preparation phase prior to the pole plant.

Exactly how (or if) these findings apply to V2 skating technique is not obvious. The aim of the V2 technique should be to optimize the cumulative propulsion generated from both poling and skating movements. This probably places some constraints on the movements

---

[2] It should be pointed out that Holmberg et al. [7] observed no direct correlation between performance (quantified by an incremental maximal speed test) and time to peak pole force. The two groups differed significantly, but these were selected on basis of the athletes techniques, not their performance. The authors argued that the WE group included the fastest skiers, however, the exact content of this statement was not specified.

with respect to DP, where all propulsion is generated by poling. Nonetheless, a similarity between the two techniques with regards to the use of potential energy is assumed in this thesis. As suggested by Holmberg et al. [7], skiers gain potential energy prior to the pole plant by a ”high hip, high heel” strategy (evident in Figure 1.2, 4. position). This energy is transferred to the poles during the poling action. The ”high heel”-part is not as evident in the V2 technique (Figure 1.1), but the hip is clearly elevated prior the the pole plant. Hence, a similar argument based on potential energy can be applied also to this situation. Such use of potential energy in V2 has also been proposed by Myklebust et al. [13].

1.2 Structure

The data collection that forms the basis for this thesis was done using two very different measurement systems, each with its own benefits and limitations: A camera based system gave high quality kinematic measurements of the complete movement pattern of the athletes by tracking the position of 41 markers attached to the athletes and equipment. These measurements were analysed using a method that utilized a large amount of the information that was gathered, yet made it possible to quantify the movement using only a comprehensible amount of uncorrelated variables. The second measurement system was an inertial measurement unit (IMU). In contrast to the camera based system, the IMU could measure only a small fraction of the complex movement pattern that makes up the V2 technique. The advantage of such a system is that it is low cost, light weight and small size, and has essentially an unlimited capture volume.

In summary, the two measurements systems had more or less the same pros and cons, but with reversed signs. One aim of this thesis was thus exploit the advantages from both systems. In the author’s opinion, this was best achieved by structuring the thesis as two independent, yet fulfilling studies. The first part was to analyse the complete movement patterns from the camera based measurements, with loss of as little detail as possible. This study is presented in chapter 3. The second part was to investigate the measurements from the IMU, and in particular view these results in comparison with the much more detailed results obtained from the camera system. This study is presented in chapter 4, followed by a combined conclusion of the two studies.

However, one aspect remained. The accuracy the IMU measurements were uncertain, and needed to be determined. The validation study presented in appendix A presents the method used to obtain the data in chapter 4, and the accuracy of the measurements. However, since it does not provide any insight to the main topic of this thesis (i.e. the relation between performance and technique), the study has been relegated to an appendix.

Lastly, results from an experiment with inertial sensors contained in a smart phone is provided in appendix B. This experiment was done before I started work on the main part of this thesis, in order to get a ”hands on” feeling with inertial sensors. However, it does fit into this thesis, because it shows some of the possibilities and limitations by use of equipment widely available for the general public.

1.3 Notation

The following notation is used consistently throughout this thesis:

- Bold font and capital letters (e.g. $\mathbf{M}$) represent matrices
- Bold font and lower case letters ($\mathbf{p}$) represent vectors
- Overlines ($\overline{p}$) denote the time average
- A hat (i.e. $\hat{x}$) denote the stride cycle average
- ^{T} indicates the transposed matrix or vector

Chapter 2

Anatomical terminology

This thesis is written under the assumption that the reader possess basic knowledge of human anatomy and anatomical terminology. For the reader that is not familiar with this field, this chapter should cover the necessary terminology, and might be consulted for explanations of unfamiliar terms.

The contents of this chapter is restricted to explain terms that are needed to understand the material presented in this thesis. For a more complete introduction, the reader is referred to any introductory textbook in physiology and anatomy, for instance the book by Waugh and Grant [15]. To improve readability with respect to positioning of figures, the rest of this page is left empty.

2.1 Planes and directions

The human body is divided into three planes: the *sagittal plane*, the *coronal plane*, and the *transverse plane.* The orientation of these planes should be clear from Figure 2.1. The same goes for the anatomical directions *anterior, posterior, superior, inferior, medial* and *lateral.* The terms *proximal* and *distal* are also used in this thesis. Proximal refers to something that is close to a reference, while distal is more distant from the the reference. Normally, the reference is the point of attachment of a limb. For instance, the foot is distal to the knee.

2.2 Joints

A decrease of a joint angle is denoted *flexion*, while an increased joint angle is called *extension.* Furthermore, the movement of a limb away from the the sagittal plane is denoted *abduction*, and a movement towards the sagittal plane is an *adduction.* A rotation of a limb about its proximal-distal axis is denoted inwards/outwards rotation.

2.3 The pelvis

In the study presented in chapter 4, an IMU was mounted at the sacrum. The sacrum is part of the pelvis, which is consists of two hip bones, the sacrum, and the coccyx (Figure 2.2). The sacrum is connected to the hip bones through the sacroiliac joint, and joined by strong ligaments. This ensures that pelvis can be modelled as a rigid body. The orientation of the pelvis can thus be represented by three angles, each of which describes a rotation about one of the axes apparent in Figure 2.2. Also indicated in Figure 2.2 are the locations of the right and left *anterior superior iliac spine*, abbreviated ASIS. These anatomical landmarks are used both in chapter 3 and appendix A.

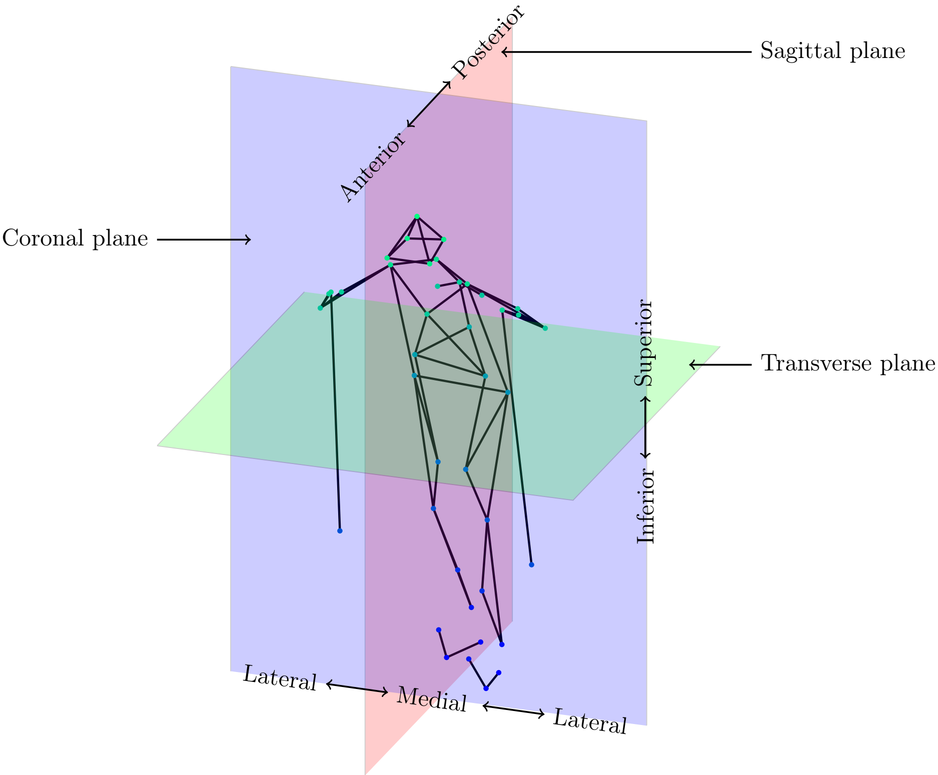

FIGURE 2.1: Definition of anatomical planes and directions. Throughout this thesis, an axis convention is used so that the y-axis is directed in the anterior direction, the z-axis in the superior direction, and the x-axis in the lateral direction, so that the xyz-frame makes up a right handed coordinate system.

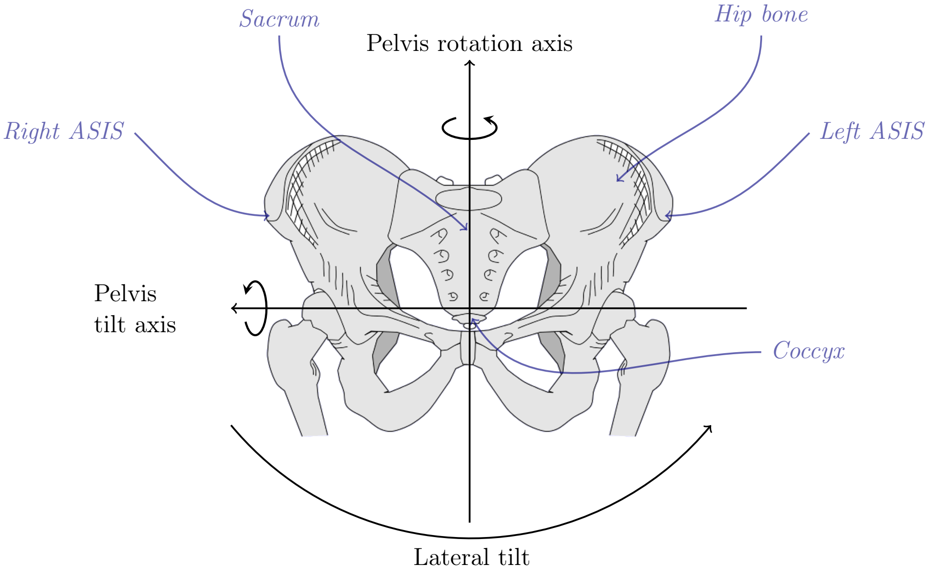

FIGURE 2.2: Anterior view of the pelvis, with rotation and tilt angle definitions. The lateral tilt axis is directed out of the plane in this figure. From these axis definitions, a positive pelvis tilt results in a posteriorly directed pelvis (i.e. the hip bones are moved to a more posterior position). A positive lateral pelvis tilt results in a left tilted pelvis (i.e. the left hip bone is elevated compared to the right hip bone). (This figure is based on an image from Wikimedia commons, provided by Michael Frey. It has been altered for use in this thesis by adding annotations and axis conventions)

Chapter 3

Analysis of skiing technique: a holistic approach

3.1 Introduction

The complexity of the V2 movement pattern makes it a challenge to scientifically analyse the motion. This is particularly true for quantitative analysis. A solution to this problem might be to restrict the focus to include only a few, preselected variables based on prior knowledge. An obvious drawback with this approach is the risk of selection bias, which might result in important relations being overlooked, or confirmatory results. Another approach is to measure a multitude of variables, before determining what variables appear most interesting[7, 12]. However, even this approach is subject to selection bias.

Another approach to manage the high complexity in the analysis of multi-body motion patterns is by conducting a principal component analysis (PCA). A PCA decomposes the high-dimensional multi-body movement patterns into a set of few one-dimensional movement components that represent the main sources of postural variability, and residuals that typically contain a small fraction of the postural variability[16, 17]. PCA has been applied for technique analysis in sports [18, 19], however, an important limitation of previous PCA-based analyses was that the PCA is calculated separately for each individual subject. A direct comparison of the techniques between athletes was compromised by other sources of postural variability such as anthropometric differences. A major methodological advancement introduced in the current study is an improved normalization technique that filters out anthropometric differences and that considers the weight distribution between body segments. This enabled direct comparison of movement components between subjects and it allowed for studying how multi-segment movement components influenced the skiers' center of mass motion.

3.2 Theory

To understand the underlying principles of PCA, basic knowledge of linear algebra is needed. The necessary theory is outlined in this section.

3.2.1 Bases

A *basis* is a set of linearly independent vectors that spans some vector space H. A common basis for the vector space $\mathbb{R}^q$ (i.e. the space of all possible q-dimensional vectors) are the columns of the identity matrix $\mathbf{I}_q$. This is known as the *standard basis*[20]. The standard basis is an example of an orthonormal basis, i.e. a basis where all vectors are orthogonal and of unit length. A q-dimensional vector can be expressed in any basis that spans $\mathbb{R}^q$. However, a clever choice of basis might simplify a problem substantially. This section deals with one way of determining such a basis.

If we represent a point in a laboratory reference frame using three perpendicular axis XYZ, this is equivalent to a vector representation in the standard $\mathbf{I}_3$-basis. If we want to measure m points in the XYZ-frame, we need to define m vectors. Alternatively, we can express the m points as a single $3m$-dimensional vector, using a $3m \times 3m$ basis. This approach was suggested as a method to measure human gait by Troje [17]. He defined a *posture*

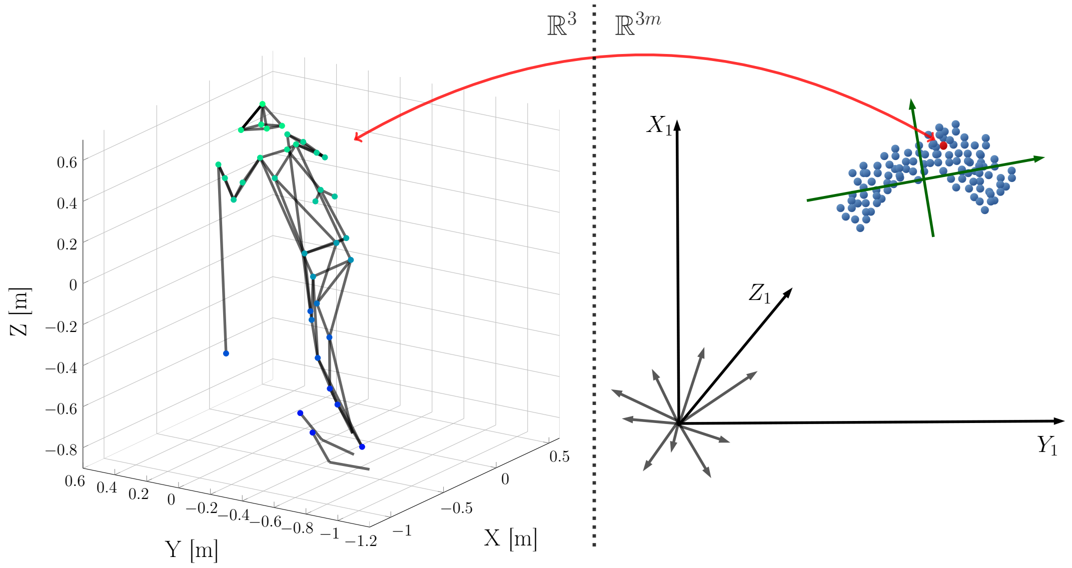

FIGURE 3.1: Illustration of the posture vector. Left side: a cloud of m points in 3D space, representing a skiers posture at a given time. Right side: $3m$-dimensional hyperspace, with the current posture represented as a single vector (red dot). The cloud of all postures generated over time (blue dots) has a characteristic shape which depends on the specific movement pattern, and typically occupy only a small fraction of the $3m$-space. Green lines represent vectors of a new basis, that are directed along the directions of largest postural variance.

vector, which consisted of the spatial coordinates of m points on the human body. Using this terminology, the posture vector $\mathbf{p}(t)$ specifies an individuals posture at any given time point t. If the marker coordinates are all from the XYZ-laboratory coordinate frame, the posture vector is represented in the $\mathbf{I}_{3m}$-basis.

Human movement, although highly complex, is still subject to a large number of constraints. For that reason, the posture vector represented in the $\mathbf{I}_{3m}$-basis is highly redundant, i.e. it occupies only a small fraction of the $3m$-dimensional vector space (figure 3.1). This motivates the definition of a new basis, where the basis vectors are aligned in the directions of large postural variance. Principal component analysis is a decomposition method that can be used to find such a new basis[16, 17].

3.2.2 PCA

PCA is a linear decomposition method with its mathematical foundation based in linear algebra. To outline the mathematical principles of PCA, we need the following five theorems:

Theorem 3.1. *For an orthogonal matrix* $\mathbf{A}$*, then* $\mathbf{A}^T = \mathbf{A}^{-1}$

Theorem 3.2. *The transpose of a product is equal to the product of the transposed matrices, with the order reversed:* $(\mathbf{AB})^T = \mathbf{B}^T\mathbf{A}^T$

Theorem 3.3. *For any matrix* $\mathbf{A}$*, both* $\mathbf{A}^T\mathbf{A}$ *and* $\mathbf{A}\mathbf{A}^T$ *are symmetric matrices*

Theorem 3.4. *A matrix is symmetric if and only if it is orthogonally diagonalizable.*

Theorem 3.5. *A symmetric matrix* $\mathbf{A}$ *is diagonalized by a matrix* $\mathbf{E}$ *of its orthonormal eigenvectors:* $\mathbf{D} = \mathbf{E}^T\mathbf{A}\mathbf{E}$.

For proofs of these theorems, the reader is referred to any introductory linear algebra textbook, for instance the book by Lay [20].

We start by defining the *measurement matrix* $\mathbf{M}$. $\mathbf{M}$ is of size $n \times m$, where n is the number of observations, and m is our number of variables. Assuming that we do not a priori know the relation between the variables, we can still obtain a measure of their inter-dependence by calculating the sample covariance matrix of $\mathbf{M}$: [1]

$$\mathbf{\Sigma_M} = \frac{1}{n-1}\mathbf{M}^T\mathbf{M} \tag{3.1}$$

By theorem 3.3, the covariance matrix is a $m \times m$ symmetric matrix. The off diagonal elements $\Sigma_{i,j}$ are the covariances between measurement i and j, and hence a measure of their dependence, while the diagonal elements $\Sigma_{i,i}$ are simply the variance of variable i. Obviously, if all variables are independent, $\mathbf{\Sigma}$ is a diagonal dominant matrix. Hence, if we can perform a change of basis for the variables of $\mathbf{M}$, so that the covariance matrix of the new matrix is a diagonal matrix, the variables in the new basis are all uncorrelated. Furthermore, if the original variables were redundant in the old basis, the number of uncorrelated variables must be less than the original number of variables. Such a change of basis is expressed as:

$$\mathbf{T}\mathbf{M}^T = \mathbf{\Xi}^T \tag{3.2}$$

where $\mathbf{T}$ is a $m \times m$ matrix who's columns make up an orthonormal basis for $\mathbb{R}^m$. What remains to show is how $\mathbf{T}$ can be determined so that the covariance matrix of $\mathbf{\Xi}$ is diagonalized.

Writing $\mathbf{\Sigma_\Xi}$ in terms of $\mathbf{T}$, we find (by theorem 3.2):

$$\begin{aligned}
\mathbf{\Sigma_\Xi} &= \frac{1}{n-1}\mathbf{\Xi}^T\mathbf{\Xi} \\
&= \frac{1}{n-1}\left(\mathbf{T}\mathbf{M}^T\right)\left(\mathbf{T}\mathbf{M}^T\right)^T \\
&= \frac{1}{n-1}\mathbf{T}\mathbf{M}^T\mathbf{M}\mathbf{T}^T \\
&= \frac{1}{n-1}\mathbf{T}\mathbf{A}\mathbf{T}^T
\end{aligned} \tag{3.3}$$

Where we in the last line defined $\mathbf{A} = \mathbf{M}^T\mathbf{M}$. It follows from theorem 3.3 that the matrix $\mathbf{A} = \mathbf{M}^T\mathbf{M}$ is a symmetric matrix. Furthermore, it follows from theorem 3.4 and 3.5 that $\mathbf{A}$ is diagonalized by a basis of its normalized eigenvectors. Hence, the problem reduces to determining the normalized set of eigenvectors for $\mathbf{A}$. Since $\mathbf{A}$ differ from $\mathbf{\Sigma_M}$ by only a scaling factor, this is equivalent to finding the eigenvectors of $\mathbf{\Sigma_M}$.

It should be clear from theorem 3.5 that if we select $\mathbf{T} = \mathbf{E}^T$, where the columns of $\mathbf{E}$ are the normalized eigenvectors of $\mathbf{A}$, then $\mathbf{\Sigma_\Xi}$ is a diagonal matrix. Hence, the variables of $\mathbf{\Xi}$ are uncorrelated. We call the columns of $\mathbf{E}^T$ the *principal components* of $\mathbf{M}$, and the columns of $\mathbf{\Xi}$ the *time evolution coefficients* . Because $\mathbf{\Sigma_\Xi}$ is diagonal, the variance of the

---

[1] The calculation of the sample covariance matrix only makes sense if $\mathbf{M}$ is in mean-deviation form, i.e. that the rows of $\mathbf{M}$ has zero sample mean

new variables are equivalent to the eigenvalues of the computed eigenvectors (or differ only by a scaling if the eigenvalues are calculated from $\mathbf{\Sigma_\Xi}$ rather than $\mathbf{A}$).

The principal component vectors are sorted by the corresponding eigenvalues. In summary, a PCA is comprised of the following four steps:

1. Calculate the sample covariance matrix $\mathbf{\Sigma_M}$ of $\mathbf{M}$
2. Obtain an orthonormal set of principal component vectors (**PC**) by calculating the eigenvectors of $\mathbf{\Sigma_M}$.
3. Sort the principal component vectors by their eigenvalues in decreasing order.
4. Project the original measurement matrix $\mathbf{M}$ onto the principal component vectors to obtain a set of new, uncorrelated *time evolution coefficients* (denoted $\xi(t)$, the columns of Ξ), whose variance is strictly decreasing with the order of the principal component vectors.

3.2.3 Link to singular value decomposition

The outline of PCA given above underlines the motivation, i.e. to reduce many correlated variables to fewer, uncorrelated variables. However, computation of the sample covariance matrix might lead to loss of precision in numerical calculations[20]. For that reason, the preferred approach in numerical calculations is often to use the *singular value decomposition.*

There is a tight link between PCA and the singular value decomposition, which enables a determination of the principal components and eigenvalues without calculating the sample covariance matrix. The singular value decomposition states that any $n \times m$ matrix $\mathbf{X}$ can be decomposed into a set of three matrices: an orthogonal $n \times n$ matrix $\mathbf{U}$, a rectangular diagonal $n \times m$ matrix $\mathbf{\Lambda}$, and an orthogonal $m \times m$ matrix $\mathbf{V}^T$:

$$\mathbf{X} = \mathbf{U\Lambda V}^T \tag{3.4}$$

No proof of the singular value decomposition will be outlined in this thesis, and again the reader is referred to the book by Lay [20, ch 7.4]. However, the link to PCA is easily verified by calculating the sample covariance matrix of $\mathbf{X}$:

$$
\begin{aligned}
\mathbf{\Sigma_X} &= \frac{1}{n-1}\mathbf{X}^T\mathbf{X} \\
&= \frac{1}{n-1}\left(\mathbf{U\Lambda V}^T\right)^T\left(\mathbf{U\Lambda V}^T\right) \\
&= \frac{1}{n-1}\mathbf{V\Lambda U}^T\mathbf{U\Lambda V}^T \\
&= \frac{1}{n-1}\mathbf{V\Lambda}^2\mathbf{V}^T
\end{aligned}
\tag{3.5}
$$

Where we have used theorems 3.1 and 3.2. From this it should be clear that if we define $\mathbf{X} = \frac{1}{\sqrt{n-1}}\mathbf{M}$, and decompose $\mathbf{X}$ using the singular value decomposition, then the columns of $\mathbf{V}$ are the principal components of $\mathbf{M}$, and the eigenvalues are simply the square root of the diagonal elements in $\mathbf{\Lambda}$.

3.3 Previous studies applying PCA to human movement

As stated in the previous section, the first application of PCA to analyse human movement, at least in a manner similar to what was outlined above, was the study by Troje [17]. The aim of their study was to assess how socially relevant information contained in human movement patterns could be extracted. To investigate this, he analysed differences in the walking patterns of males and females. The method involved two subsequent PCAs. First, he decomposed a set of highly correlated *postures* (determined by a set of marker coordinates) into an average posture vector, and 4 principal component vectors that covered most of (> 98%) of the postural variance. Succeedingly, he fitted sine functions to the four corresponding time evolutions coefficient series. This enabled a representation of each walker by a walk-vector, which consisted of the concatenation of the average posture vector, the 4 principal component vectors, and the frequency and phase of the sine functions. The walk vectors of all individuals formed a new matrix, which was again submitted to a PCA. The result of this PCA was an average walk vector, and a set of *eigenwalkers* that represented the directions of largest walk-vector variance. Finally, a linear classification algorithm was used to classify walkers as male/female, with a varying number of eigenwalkers included. The performance of the algorithm was tested against a set of human observers, and showed a substantially better performance (90% success rate vs 76% success rate).

Daffertshofer et al. [16] did a study showing the applicability of PCA to study coordination and variability in human movement. They pointed out that a normalization of all variables to unit variance prior to conducting a PCA is advisable, due to the inherent sensitivity of PCA to differences in amplitude. This is particularly important if measurements of different unit are submitted to the same analysis. They applied PCA to two different types of data measured during human gait: kinematic data and muscle activation (EMG). Here, only the kinematic analysis will be assessed. They showed that PCA can be used both as a method of dimensional reduction, by an approach very similar to the first PCA performed by Troje [17]. They also showed that it can be used to analyse the variability of human locomotion. This was achieved by excluding the first four principal components, which accounted for most of ($\sim$ 90%) the variance. The remaining components contained for the most part stochastic movements. They showed that for the example subject, substantially higher movement variability was present in the feet and hands than the rest of the body segments during gate.

Federolf et al. [21] used PCA to analyse postural movements during bipedal, tandem and one-leg stance. The analysis procedure was similar to the first PCA described by Troje [17], with one important difference: instead of submitting each subject to an independent PCA, all subjects were *pooled* into one large matrix, which was submitted to a PCA. This resulted in principal components that reflected the directions of the largest combined postural variance, and enabled a direct comparison of the time evolution coefficients between subjects. They developed a method to account for anthropometric differences between the subjects, with the aim of minimizing the influence of such differences to the result of the PCA. The method was comprised of three steps: (1) subtraction of the mean posture, (2) calculation of the vector norm of the of the centered posture vectors, and (3) division of all centered postures with the mean vector norm. This procedure was performed for each subject, and ensured that the size of the cloud of postures (Figure 3.1) for each subject was of uniform size, while its shape remained unchanged.

PCA has also been applied to technique analysis in sports by Federolf et al. [18]. They investigated the applicability of PCA to the movement patterns of elite junior alpine skiers. Two different analysis were performed: (1) an individual PCA for each subject, and (2) a pooled PCA similar to the study described in the previous paragraph [21]. However, no procedure to reduce the effect of anthropometric differences on the pooled PCA was performed. They concluded that PCA worked well in reducing the complex skiing movement to a small set of uncorrelated principal movements, which had both and accurate quantification (through the time evolution coefficients), and could be interpreted qualitatively by movements of a stick figure. They suggested that this method should be applicable to a wide range of sports.

In summary, PCA has proved a powerful tool to analyse complex movement patterns in a holistic manner. It can be used both as a method to reduce dimensionality, and to investigate motion variability. For the purpose of this thesis, the focus was restricted to dimensional reduction. Furthermore, emphasis was put on a direct comparison of movement components between athletes, which suggested use of the pooling procedure presented by Federolf et al. [21].

3.4 Materials and Methods

The following section describes the participating athletes, experimental procedures, equipment, and the data analysis methods used in the current study.

3.4.1 Participants

Six elite cross country skiers (male, age 26 ± 2 years, height 180 ±5 cm, weight 79.5 ± 5 kg) volunteered for this study, and gave their written informed consent prior to participating. All athletes had finished in the top 30 in the Norwegian national championships, all but one of the skiers had FIS[2] World Cup experience, and three had multiple World Cup podium finishes. At the time of the measurement, their FIS sprint point ranking ranged from 14-157 points on the FIS points list. In the current study we interpreted the athletes' FIS points as an indicator of their skill level. However, one of the issues that have to be considered is that skiers with less than five FIS-races get penalized in the official FIS point ranking. This affected one of our athletes. Without this penalty the athletes' FIS points would range from 14-116, which, in our opinion, is a more appropriate representation of our athletes' skill level. The results of the current study were therefore compared to the adjusted FIS points.

3.4.2 FIS-point calculations

FIS-points is a ranking system developed by FIS. All skiers that participate in a FIS-approved race are awarded FIS-points. The points are calculated from the following relation[22, page 19]:

$$\text{FIS-points} = \left(\frac{t_x}{t_0} - 1\right) \cdot F + P_{\text{race}} \tag{3.6}$$

where t_x is the finishing time of the competitor, t_0 is the finishing time of the winner, and $F = 1200$ is a scale factor. P_{race} is a race penalty, and is either determined from the FIS-points of the five first athletes in the race, or by a fixed penalty. FIS world cup races, olympic races, or FIS world championship races are the only races with a fixed penalty of $P_{\text{race}} = 0$. The FIS-points of an athlete is the average of his five best ranked races during a period of 12 months. As mentioned above, a competitor with less than five races

---

[2] International Ski Federation

is penalized, however, this penalty has been removed for use in this thesis. Hence, the FIS-points should be an approximately linear measure of an athletes long time performance.

3.4.3 Experimental protocol

The measurements for the current study were collected during a submaximal load and a maximal time trial test on a roller skiing treadmill, described in detail by Losnegard et al. [3]. All subjects were familiar with treadmill testing and the testing protocols, as they had used such tests regularly for monitoring of their training progress. Preparation of the athletes, which included anthropometric measurements and mounting of markers, lasted approximately 45 minutes. After a short warm up on the treadmill, a 5-minute submaximal bout was performed at a inclination of 4° and speed 3 m/s. Thereafter, two additional 5 min submaximal bouts at higher inclination were performed, followed by a 10 min brake before the time trail. The time trail was a 1000 m performance test at constant treadmill inclination of 6°. The speed was initially set to 3.25 m/s for the first 100 meters and then to 3.5 m/s from 100 to 200 meters. Thereafter, the athlete was free to choose his own speed, with increments of ± 0.25 m/s. The athletes were informed of the distance travelled by both visual feedback on a monitor and oral feedback from the test leader.

For the technique analysis in the current study, two datasets were collected for each skier: (a) when skiing at 3 m/s and a treadmill inclination of 4°, and (b) when skiing at the individually chosen maximum speed. This speed was achieved between $200 - 440$ m of the performance test, ranged from 4.00 to 4.75 m/s, and was constant during the analysed time period. Both sets included at least 12 consecutive stride cycles.

3.4.4 Data collection and instrumentation

The testing took place on a treadmill specially designed for roller skiing, with belt dimensions of 3×4.5 m (Rodby, Södertalje, Sweden). All skiers used the same pair of roller skis (Swenor Skate 65-000, Sport Import AS, Sarpsborg, Norway). The athletes were allowed to use their own ski poles, modified with a tip specially adapted for use on a roller skiing treadmill.

The athletes' movements were recorded at a frame rate of 250 Hz using a 3D motion analysis system consisting of nine cameras (Oqus 400, Qualisys AB, Gothenburg, Sweden) controlled by the Qualisys Track Manager (QTM) software (Qualisys AB, Gothenburg, Sweden). The motion capture system was calibrated dynamically using a wand with two retro reflective markers at a fixed separation, which resulted in an accuracy < 2 mm RMS. A sketch of the experimental setup is presented in Figure 3.2

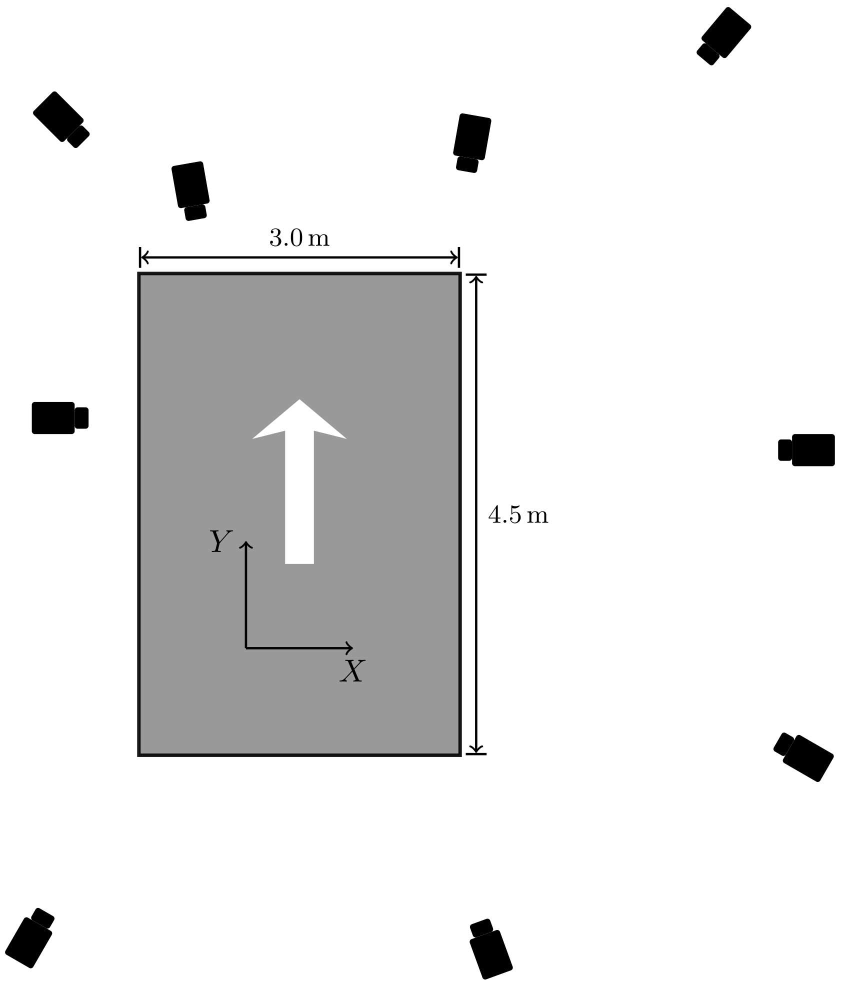

FIGURE 3.2: Treadmill and camera setup. Z-axis was directed out of the plane. Camera positions are estimates

Forty-one retro reflective markers attached to the athletes' skin and skiing equipment were tracked. The markers were placed on and between anatomical landmarks to track the motion of the athletes' segments and joints. Specifically, markers were placed on the tibialis anterior, knee joint (laterally), rectus femoris, trochanter major, anterior superior iliac spine, os sacrum, sternum, 10th thoracal vertebra, 12th rib, 7th cervical vertebra, acromion, biceps brachii, elbow joint (laterally), mid forearm, and on the distal end of the radius. One marker was attached to the lateral side of each ski boot near the ankle. A custom built hat, having five markers attached (top, left temple, right temple, left posterior, right posterior), was worn by all athletes. Additional markers were placed close to the distal tip on the poles and three markers were attached to each ski (posterior, anterior and 10 cm superior to the ski). Figure 3.3 shows the positioning of all markers on one of the subjects.

The trajectories of these markers were calculated using the QTM software. A few trajectories exhibited gaps which were filled by interpolation (short gaps) or by a PCA-based reconstruction algorithm [23]. Filtering of the data was not necessary. The center of mass

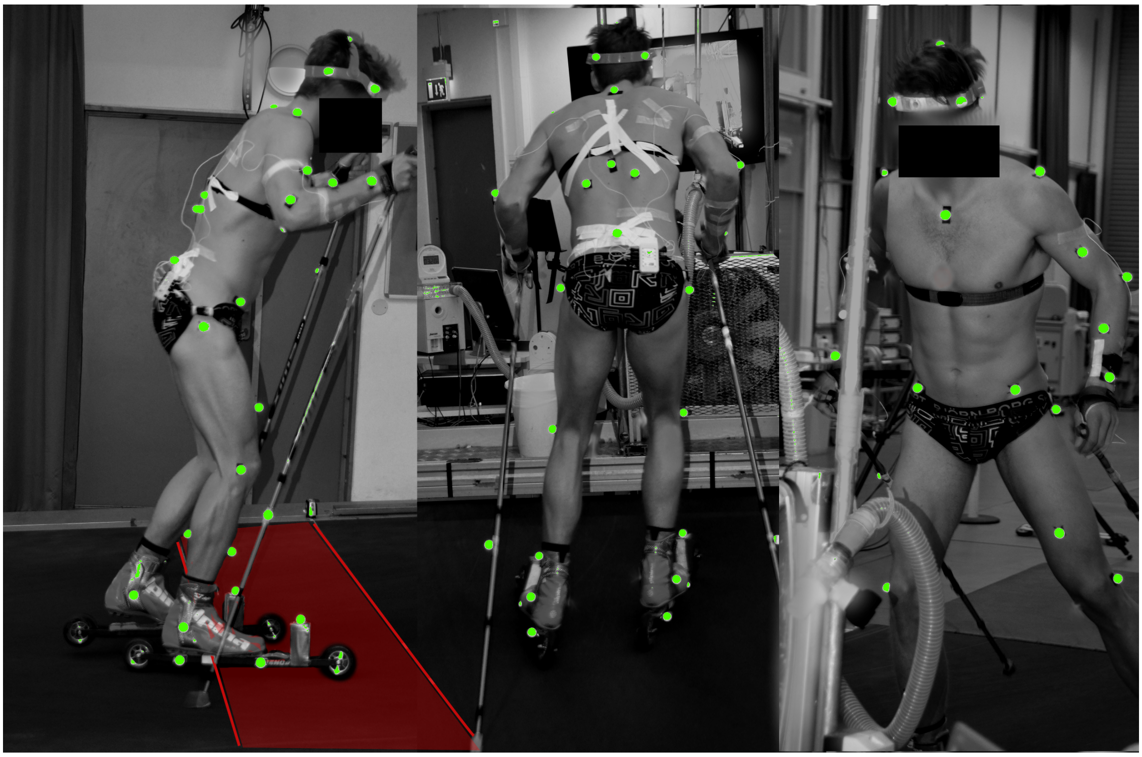

Figure 3.3: Positioning of retro-reflective markers, highlighted in green. The area marked in red shows the area delimited by two laser beams, which (during the performance test) corresponded to the zone where the speed was kept constant. If the athletes positioned themselves anterior or posterior to this area, the speed was increased/reduced by increments of 0.25 m/s

(COM) of the athletes (including equipment) was estimated by a 19-segment model using the software Visual3D (C-Motion, Inc., Germantown, MD, USA)[3]. All other data analysis was done using Matlab (The MathWorks, Natick, MA, USA). The coordinates of the 41 markers were expressed in a reference system originating in the center of mass position of the skier, with the X-axis pointing in the lateral direction compared to the treadmill belt, the Y-axis in anterior, and the Z-axis in vertical direction.

3.4.5 Data analysis: identification of movement components of interest

The data analysis procedure comprised four main steps: First, the kinematic data collected for each participant was normalized and scaled such that the movement patterns of all participants could be pooled and submitted to one comprehensive analysis. Second, a PCA was used to decompose the complex whole-body motion patterns of skating into one-dimensional, correlated movement components ("principal movements"). Third, features in the COM movement and in the principal movements were identified that appeared to change systematically with the rank of the skiers' skill level, even when accounting for the

---

[3] The COM model was mainly developed by Håvard Myklebust, PhD student at the Norwegian School of Sport Sciences

intra- and inter-subject variability of motion. Fourth, a statistical analysis was conducted to assess the specific features identified in step three. The following paragraphs describe these steps in detail.

Normalization and scaling

Twelve consecutive stride cycles, from the pole plant (right pole) on the right side to the succeeding pole plant on the right side, were selected for each athlete. The pole plants were identified as peak acceleration of the pole marker. Each stride cycle was resampled to 401 measurement points, giving a total of $n = 4812$ samples per athlete. For each time point t_i , $i \in [1, n]$ the coordinates of the 41 markers defined a $m = 123$ (i.e. $3 \cdot 41$) dimensional posture vector $\mathbf{p}(t_i)$. Each trial of a subject N defined a $n \times m$ matrix $\mathbf{M}_N$, where the columns corresponded to the marker coordinates, and the rows corresponded to the time frames. A *mean posture vector* ($\overline{\mathbf{p}_N}$) was calculated as

$$\overline{\mathbf{p}_N} = \frac{1}{n} \left(\sum_{i=1}^{n} M_{i,1} \, , \sum_{i=1}^{n} M_{i,2} \, , \ldots \sum_{i=1}^{n} M_{i,m} \right) \tag{3.7}$$

and subtracted from each row of the posture matrix $\mathbf{M}_N$, giving a new matrix $\mathbf{M}'_N$. To account for anthropometric differences, the scaling method proposed by Federolf et al. [21] was applied: the Euclidean norm d_i of all rows (i.e. posture vectors) was calculated and $\mathbf{M}'_N$ was divided by the averaged $\overline{d}_N$. Additionally, each row of $\mathbf{M}'_N$ was multiplied (by elementwise multiplication) with a 123-dimensional weight vector $\mathbf{w}$ representing the relative mass (according to Dempster and Gaughran [24]) of the body segment to which the marker was attached. If more than one marker was attached to a given segment, then the mass of the segment was divided equally over the corresponding markers. These two scaling procedures resulted in matrices $\mathbf{M}''_N$ for each subject N, which could now be pooled into a $Nn \times m$ pooled matrix $\mathbf{M}_{\text{pooled}}$, structured in the following way:

$$\mathbf{M}_{\text{pooled}} = \begin{pmatrix} \mathbf{M}''^{T}_1 & \mathbf{M}''^{T}_2 & \mathbf{M}''^{T}_3 & \ldots & \mathbf{M}''^{T}_N \end{pmatrix}^T \tag{3.8}$$

Principal component analysis and principal movements

A PCA conducted on $\mathbf{M}_{\text{pooled}}$, resulted in (i) a 123×123 dimensional matrix $\mathbf{PC} = [\mathbf{pc_1}, \mathbf{pc_2}, \ldots, \mathbf{pc_k}]$ containing the principal components vectors; (ii) a 123-dimensional eigenvalue vector $\boldsymbol{\lambda}$ consisting of the normalized eigenvalues contained in the corresponding $\mathbf{pc_k}$–vector; and (iii) the time evolution coefficients $\xi_{N,k}(t_i)$, i.e. the projection of the postural movements onto the principal component vectors. The complete posture of any time frame i could then be expressed as the sum of the mean posture $\mathbf{p}_N$ and a linear combination of the **pc**-vectors:

$$\mathbf{p}_N(t_i) = \overline{\mathbf{p}_N} + \mathbf{S} \cdot \sum_{k=1}^{123} \xi_{N,k}(t_i) \cdot \mathbf{pc}_k \tag{3.9}$$

where the scaling matrix $\mathbf{S}$ was defined as $\mathbf{S} = [\text{diag}(d^{-1} \cdot \mathbf{w})]^{-1}$. The 123 time evolution coefficients characterized changes in an athlete's posture, i.e. his postural movements. Each of these time evolution coefficients could individually be projected back onto the original coordinate system using the following relation:

$$\mathbf{pm}_{N,k}(t_i) = \overline{\mathbf{p}_N} + \mathbf{S} \cdot (\xi_{N,k}(t_i) \cdot \mathbf{pc}_k) \tag{3.10}$$

where **pm** stands for "principal movement"[18]. The **pm** represented multi segment movement patterns, i.e. components of the athletes' technique. They could be characterized qualitatively as movements by a stick figure, and analysed quantitatively through their time evolution coefficients $\xi_{N,k}(t_i)$. Their corresponding eigenvalues λ_k quantified the relative contribution of the **pm** to the total variance of the postural movements. Systematic differences in the athletes' techniques were then determined as differences in the time evolution coefficients as a whole or at specific time points.

Feature extraction

Line density plots of the time evolution coefficients were generated using all 72 stride cycles at the given effort level (6 athletes × 12 cycles). The individual lines were color coded according to the FIS sprint points ranking of the athletes. Thus, the line density plots accounted for the intra-subject variability in carrying out the skating steps and visualized inter-subject differences as a change in color. The line density plots were created by mapping all cycles into one graph and low-pass filtering in the vertical direction using a two-way FIR-filter with coefficients decreasing linearly to zero over a range of 7.5% of the length of the y-axis. Similar line density plots were created for the three components (in an external reference frame) of the COM movement to assess if characteristic differences in the overall motion patterns of the subjects existed.

Three types of features were evaluated. Differences in amplitude, denoted with an α, were measured as peak to peak (p2p) amplitude. If the signal contained higher harmonics than the cycle frequency, then the p2p amplitude was calculated for each sub cycle and averaged (feature α_{pc_3}). Differences in timing, denoted with a τ, were calculated using an unbiased cross correlation[25] of each time series (ξ or COM) with the corresponding time series representing the mean over all athletes. Three features, ϕ_{pc_4} and $\phi_{\text{pc}_{5,1/2}}$, could not be described using whole-cycle variables. Feature ϕ_{pc_4} was calculated as the difference between $\xi_4(t_i)$ in the interval $t_i, \in, [7.5, 12.5]\%$ of the stride cycle and the corresponding symmetric score 50% later in the stride cycle $t_i \in [57.5, 62.5]\%$. Features $\phi_{\text{pc}_{5,1/2}}$ were calculated as the p2p amplitudes between the pairs of peaks in ξ_5. The three types of features are summarized in 3.11

Feature	**Description**	**Quantification**
α	Difference in amplitude	Peak-to-peak
τ	Difference in timing	Unbiased cross correlations
ϕ	None of the above	Individual descriptions in the text

(3.11)

Statistics

The features of the movements that were deemed to indicate technique differences were tested for correlations with the FIS-point ranking of the athletes using the sample correlation coefficient r, defined by: [26, page 649]

$$r = \frac{S_{xy}}{\sqrt{S_{xx}} \cdot \sqrt{S_{yy}}} \tag{3.12}$$

also known as *Pearson's r*. Here $S_{xy} = \sum_{i=1}^{n}(x_i - \overline{x})(y_i - \overline{y})$, and $S_{xx} = \sum_{i=1}^{n}(x_i - \overline{x})^2$ (and similar for S_{yy}). To obtain an estimate of the significance of the correlation coefficients, the probability that there was no correlation (the null-hypothesis [26, page 418]) between the two variables of interest was tested. This was done by calculating the test statistic[26, page 654]

$$T = \frac{r\sqrt{N-2}}{\sqrt{1-r^2}} \tag{3.13}$$

If the null-hypothesis was true, the distribution of the the test statistic would be a Students t-distribution with $N-2$ degrees of freedom[4]. Hence, the probability of obtaining a less or equally likely test statistic could be calculated. The null hypothesis was rejected at a probability (p-value) < 0.05, and the observed correlation was assumed significant (denoted *). However, because the sample size in this study was small, and that we should not expect a strong correlation between the variables (many other factors than technique influence FIS-point ranking), correlations where the null-hypothesis could not be rejected at the $p < 0.05$ confidence level were also assessed. These are divided into two types: correlations with a p-value < 0.1 were considered trends, and denoted $^{\text{T}}$. Correlations with a p-value > 0.1 was considered not significant.

---

[4] This is only true if the variables are from a normal distribution. In this thesis, the normality of the variables were not tested.

All tests were conducted using the mean values over the 12 cycles of each subject.

3.4.6 Visualization and interpretation of technique differences

Technique differences identified in the time evolution coefficients are difficult to interpret for researchers and are not useful for athletes or coaches unless they can be visualized and communicated. To create a visual impression of the technique differences we "transplanted" certain movement components from one skier to another. This allowed creating two overlying stick figures; one containing the original movement of an athlete, and the other containing the same individual movement pattern except that one movement component had been exchanged with another skier's movement component. Thus, it could be visualized how the individual technique of one skier would change, if one principal movement would change in a desired way. The mathematical foundation for this hybrid movement pattern was given by

$$\mathbf{p}^{(q)}_{N_1 N_2}(t_i) = \overline{\mathbf{p}_{N_1}} + \mathbf{S} \cdot \left(\sum_{k=1, k \neq q}^{123} \xi_{N_1,k}(t_i) \cdot \mathbf{pc}_k + \sigma \cdot \xi_{N_2,q}(t_i) \cdot \mathbf{pc}_q \right) \tag{3.14}$$

Here N_1 represents the athlete whose movement is altered, and N_2 represents the athlete whose movement component q was transplanted. The additional factor σ introduced in this equation allowed an artificial amplification of this movement component (for $\sigma > 1$) to better visualize differences in the movement pattern. In that case $\xi_{N_1,q}(t_i)$ was also multiplied with σ when reconstructing the original movement pattern. This method could also be generalized to transplant more than just one movement component or to modify only specific $\xi_{N,k}(t_i)$ time intervals.

To interpret the consequences of observed differences in technique between athletes, we investigated if there existed interconnections between the measured variables. Specifically, features of principal movements that correlated with skill level were compared to COM movement. Hence, effects of postural movements on whole body movements could be determined. This was done using two approaches: 1) **pm** features (α, τ or ϕ, see 3.11) were tested for correlations with COM-features, and 2) use of potential energy was assessed by calculating the correlation coefficients between $\xi_k(t_i)$ and the vertical COM trajectory, for principal movement components k where potential energy was assumed to contribute. A higher correlation between ξ_k and the vertical COM trajectory was considered to imply a greater ability to utilize potential energy in the corresponding $\mathbf{pm}_k$.

3.5 Results

3.5.1 Skiing technique as characterized by principal movements

The first 5 principal movements, characterized by the time evolution coefficients and by stick figures representing associated changes in posture, are displayed in Figure 3.5. Together they covered 96.5 ± 0.4% and 96.1 ± 0.2% (maximal and submaximal intensity, respectively) of the total postural variance. $\mathbf{pm}_1$ captured a body lean in the lateral direction, and parts of the leg push in the sagittal plane. $\mathbf{pm}_2$ captured the hip flexion/extension movement, in addition to a pole push. $\mathbf{pm}_3$ showed an arm movement and pole swing corresponding to the poling action in the sagittal plane, and a symmetric hip ab-/adduction[5] in the coronal plane. $\mathbf{pm}_4$ showed a movement of the legs in both the sagittal (asymmetric movement) and coronal plane (symmetric movement), in addition to a small lateral translation and axial rotation of the hip. $\mathbf{pm}_5$ represented an asymmetric leg movement that captured parts of the lifting of the legs and skis. The relative cycle-to-cycle variability, quantified by the standard deviation from the mean cycle (shaded area in figure 3.5), seemed to increase with the order k of the principal movement.

The 10 first eigenvalues are displayed in figure 3.4. The variance contained in each **pc** showed a rapid decay, even on a logarithmic scale. We observed no substantial differences between the two effort levels in the lower order (i.e. $k \leq 10$) eigenvalues.

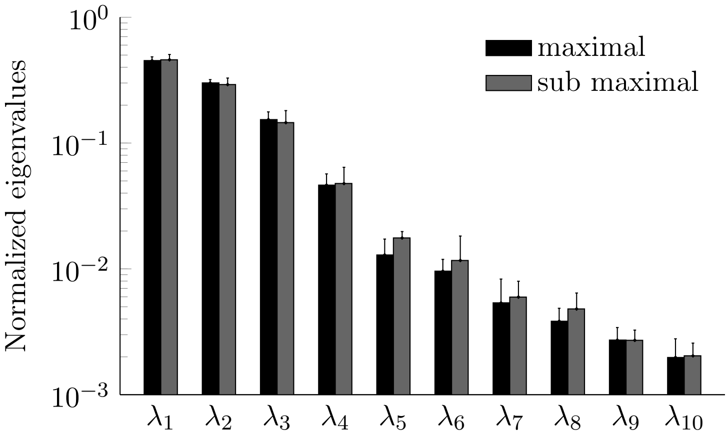

FIGURE 3.4: Log-plot of the first 10 normalized eigenvalues λ. Columns represent the subject mean, while the error bars indicate the subject-to-subject variability (standard deviation)

---

[5] The hip ab-/adduction is not apparent in Figure 3.5, because the figure only shows the sagittal plane.

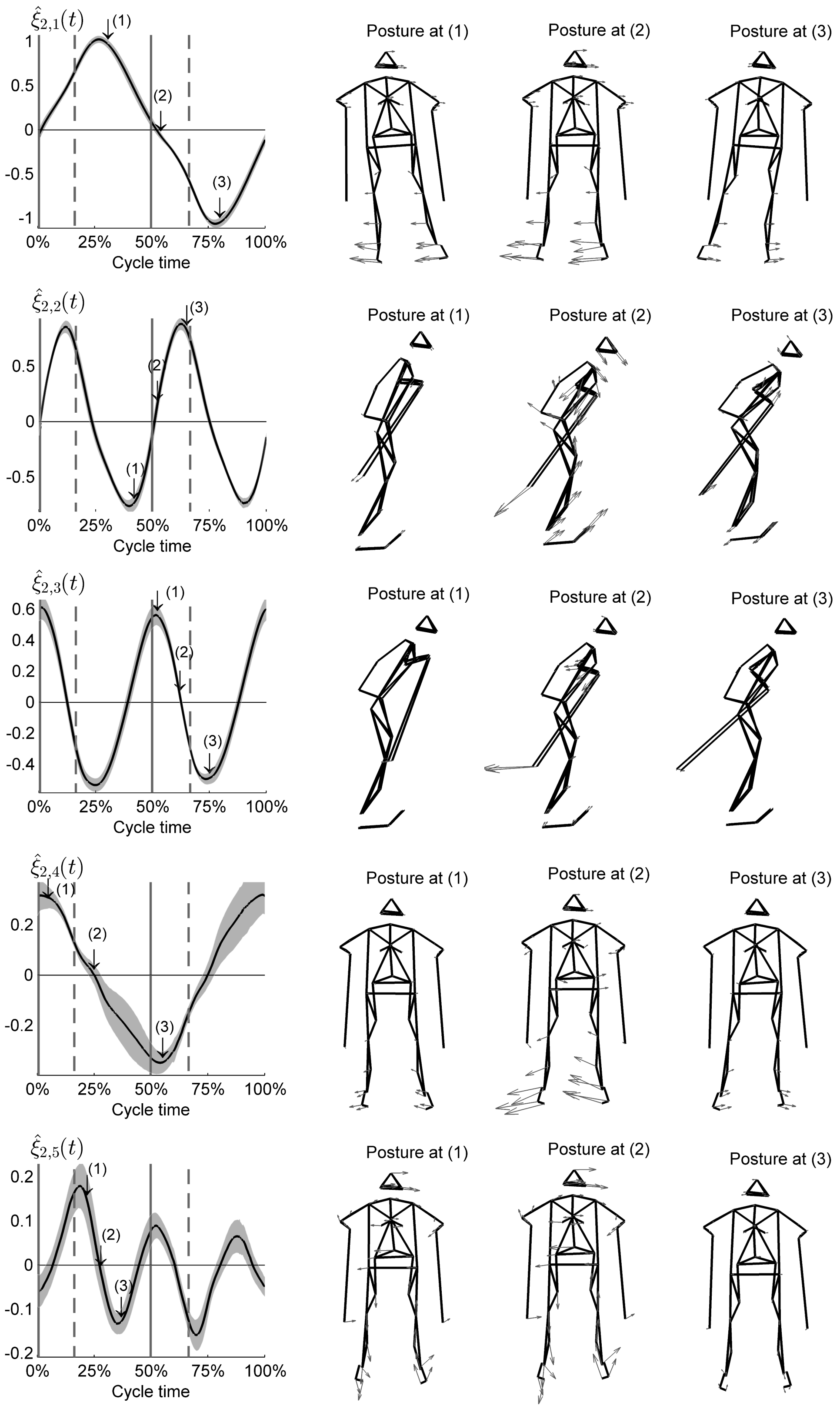

FIGURE 3.5: time evolution coefficients of the postural movements 1-5 (left column) and stick figures (right column) representing the corresponding posture at the indicated time points $(1, 2, 3)$. Arrows indicate the velocity vector of each marker at that time point. The scaling of the arrows vary for each k, and should thus not be compared across **pm**-s. The time evolution coefficients are the stride average of an example athlete, with shaded areas representing the cycle-to-cycle variability (std). Vertical lines indicate pole plants (solid) of pole leaves (dashed).

3.5.2 Assessment of the differences between skiers' techniques

COM movement

Two features of the COM movement (Figure 3.6 a-c) suggested a relationship with the athletes' FIS points. Statistical analysis (Table 3.1) indicated significant correlations for a time shift in the vertical COM movement (τ_{com_3}) for both the maximal and submaximal test, and for the lateral COM amplitude (α_{com_1}) in the submaximal test only. In the maximum effort test a trend was observed for α_{com_1}. The time shift implied that the best ranked skiers showed a lower relative COM position at the time of the pole plant. The magnitude of the timing differences between the three best ranked athletes and the three lowest ranked athletes were $31 \pm 4\,\mathrm{ms}$ and $35 \pm 7\,\mathrm{ms}$ (mean ± SEM) at maximal and submaximal intensity, respectively. This corresponded to roughly 2% of the cycle time or 4% of the vertical COM displacement time period.

The lateral movement of the COM indicated that the better ranked skiers used a smaller amplitude in the sideways movement, with the three best ranked skiers using $54 \pm 17\,\mathrm{mm}$ and $57 \pm 13\,\mathrm{mm}$ less amplitude in the maximal and submaximal tests, respectively. This amplitude difference was independent of the athletes' body height.

Principal movements

Five features of the first five time evolution coefficients (Figure 3.6 d-h) were submitted to the statistical analysis (Table 3.1). In the sub-maximal effort test, the features τ_{pc_2} and α_{pc_3} showed a significant correlation with the FIS point ranking, and ϕ_{pc_4} showed a trend. In the maximum effort test, τ_{pc_2} was significant and features ϕ_{pc_4} and $\phi_{\mathrm{pc}_{5,1}}$ showed a trend. These results indicated that the best ranked skiers flexed the hip ($\mathbf{pm}_2$) approximately $31 \pm 6\,\mathrm{ms}$ and $23 \pm 10\,\mathrm{ms}$ earlier (mean ± SEM, maximal and submaximal effort) compared to the lowest ranked athletes.

In the submaximal test the best skiers showed less amplitude in the arm movement and pole swing ($\mathbf{pm}_3$). The lateral translation and axial rotation of their hip ($\mathbf{pm}_4$) also showed a different characteristics, which led to a more medial positioning of the push ski, and a more lateral position of the glide ski at $7.5\% - 12.5\%$ and $57.5\% - 62.5\%$ of the stride cycle, i.e. during a brief period right after pole plant (Figure 3.7).

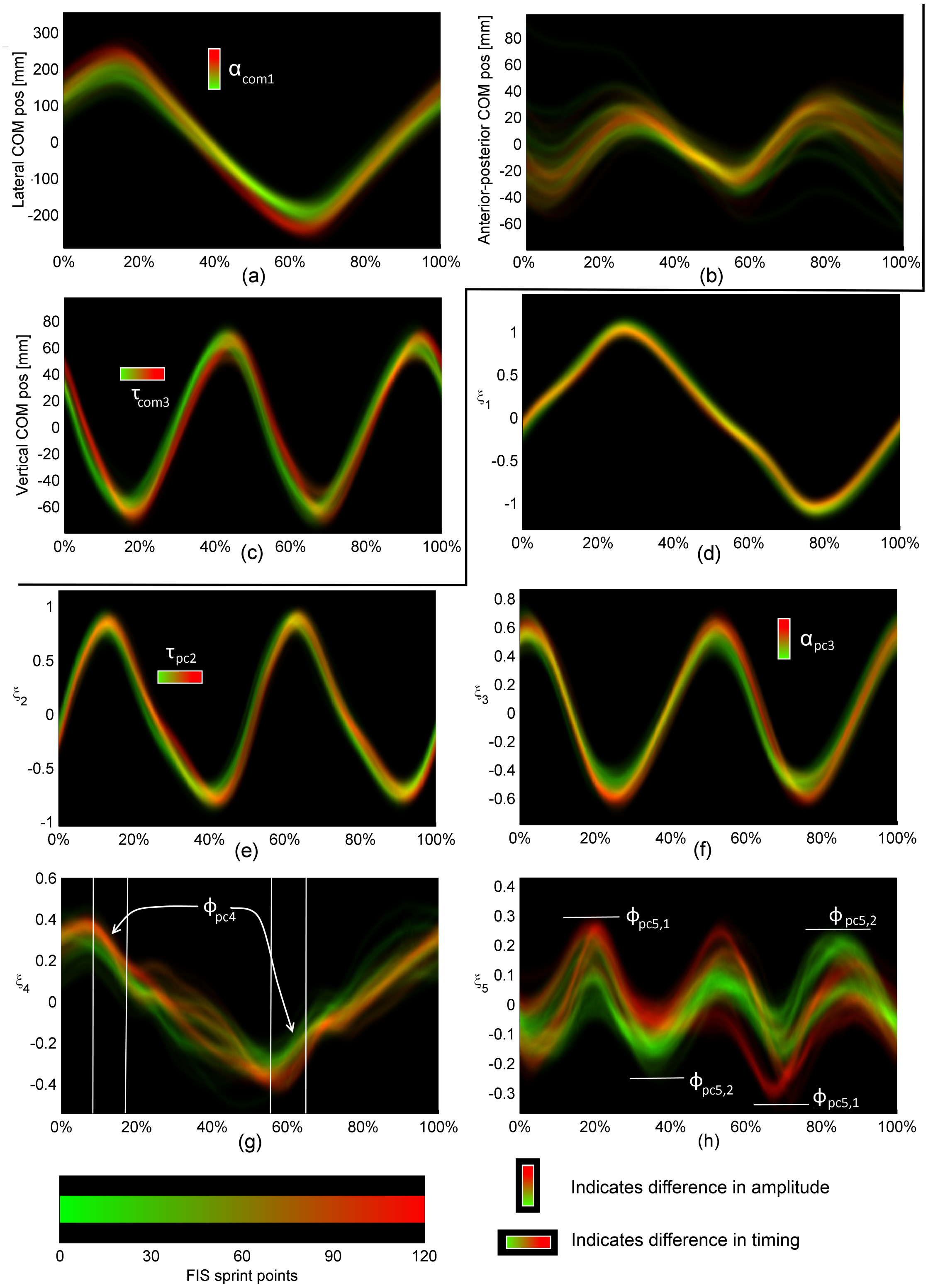

FIGURE 3.6: Line density plots of COM (a-c) and postural (d-h) movements from the maximal effort test. Areas where all skiers used the same technique appear yellow, green areas represent the best skiers, red areas represent the skiers with higher FIS-points. The annotations indicate features that were selected for further statistical evaluation: α indicates p2p amplitude differences; τ indicates a difference in timing; ϕ represents features that are described in the text.

TABLE 3.1: Correlation coefficients from comparison of technique features and FIS-point ranking in the maximal effort (max) and in the submaximal test (submax).

Reference in Fig 3.6	Description	Pearson's r	
		max	submax
	COM features		
$\alpha^{T}_{\mathrm{com}_1}$	p2p amplitude	0.76^{T}	0.96^{*}
$\tau^{*}_{\mathrm{com}_3}$	Timing difference	0.98^{*}	0.91^{*}
	Postural features		
$\tau^{*}_{\mathrm{pc}_2}$	Timing difference	0.86^{*}	0.93^{*}
α_{pc_3}	p2p amplitude	0.65	0.83^{*}
$\phi^{T}_{\mathrm{pc}_4}$	Amp. between lines	-0.74^{T}	-0.75^{T}
$\phi_{\mathrm{pc}_{5,1}}$	Knee ext. post pole strike	0.76^{T}	0.43
$\phi_{\mathrm{pc}_{5,2}}$	Knee ext. pre pole strike	-0.67	-0.58

* Significant to $p < 0.05$, ^{T} Trend ($p < 0.1$).

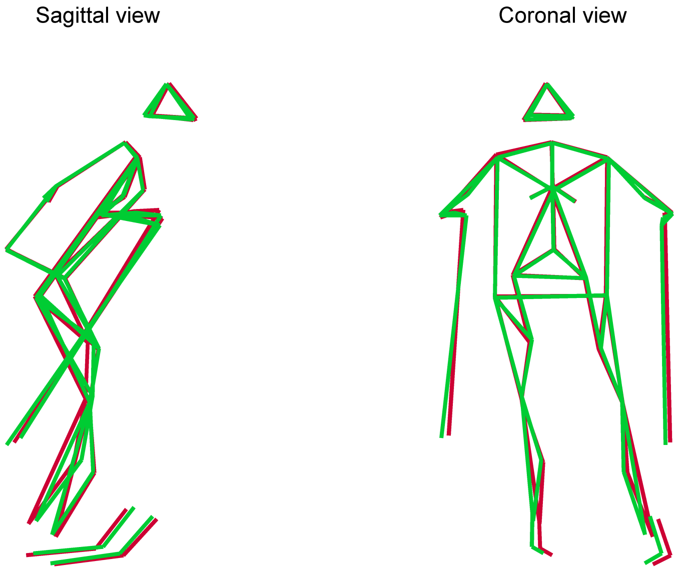

FIGURE 3.7: Hybrid movement pattern from the average movement of the three lowest ranked skiers, where $\hat{\xi}_4$ was replaced with the mean of the three best ranked skiers. Green lines: hybrid movement, red lines: average movement of the three lowest ranked skiers (for comparison). The $\hat{\xi}_4$-coefficients were amplified by a factor $\sigma = 2$ to emphasize the differences. It appeared that the difference in posture (here reconstructed at 10% of the stride cycle) consisted of a more medial position of the push ski, and a more lateral position of the glide ski at the start of the push phase

3.5.3 Relations between COM movement and principal movements

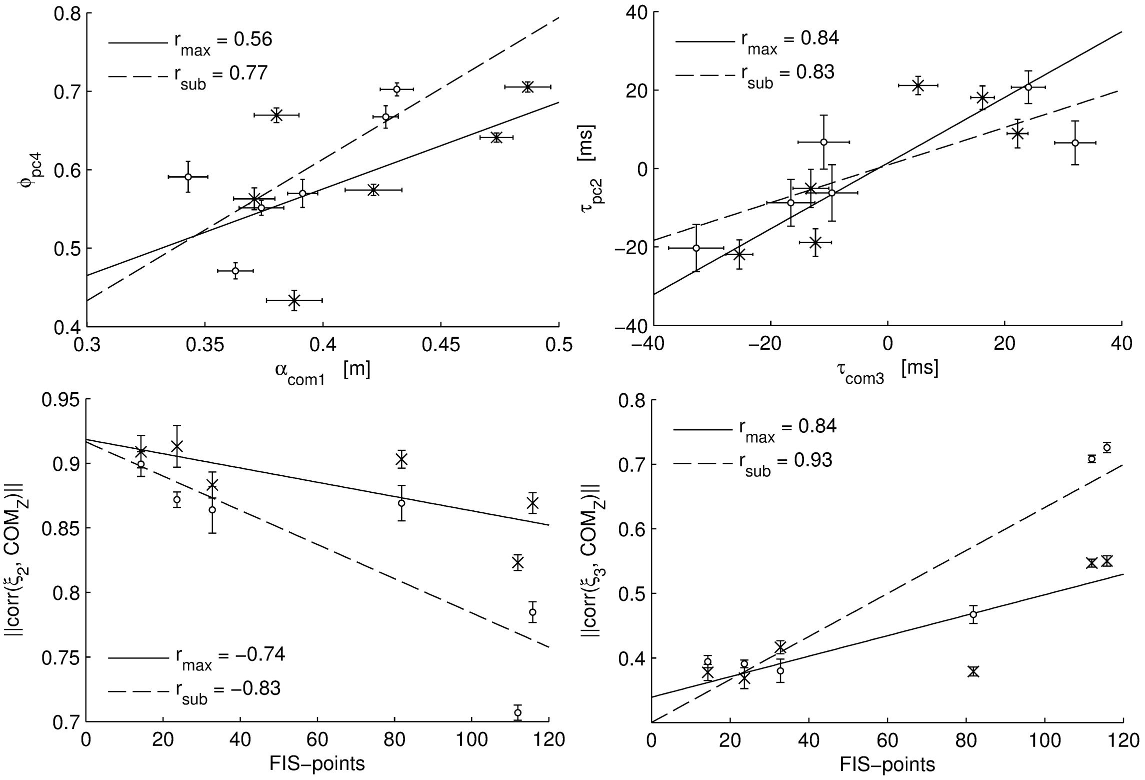

FIGURE 3.8: Top row: Correlations between COM and **pm** features. Bottom row: Correlation coefficients between vertical COM movement and $\xi_{2/3}$ correlated with FIS-points. crosses /solid line represent the maximal effort level, circles / dotted line represent submaximal effort. Error bars indicate the standard error of the mean (SEM)

Two of the **pm** features appeared to relate to features in the COM movement. First, the difference in the lateral COM amplitude (α_{com_1}) appeared to relate to the $\mathbf{pm}_4$ -features (ϕ_{pc_4}) characterizing lateral pelvis and leg motions and a pelvis rotation (Figure 3.8, upper left panel). However, submitting these features to a statistical analysis, the correlation indicated a trend only in the submaximal test ($p = 0.08$), not in the maximum effort test ($p = 0.24$). Second, the timing difference in the vertical COM movement (τ_{com_3}) correlated ($p < 0.05$) with the timing difference in the $\mathbf{pm}_2$ -movement (τ_{pc_2}) characterizing mainly hip flexion (Figure 3.8, upper right panel). A slope of 0.8 and 0.5 (maximal and submaximal) in the linear fit between the two features revealed that the time shift was more pronounced in the COM movement than in the hip flexion.

Correlation coefficients between the vertical COM trajectory and the time evolution coefficients $\xi_2(t_i)$ (hip flexion/pole push) and $\xi_3(t_i)$ (arm movement/pole swing) revealed a difference in the relative timing of the athletes. The best ranked athletes appeared to have a higher correlation between their vertical COM movement and $\xi_2(t_i)$ (figure 3.9, upper left panel), implying that their hip flexion was more synchronized in time with the vertical COM movement. This relation correlated significantly with the FIS point rating of the athletes at sub max effort, while a trend was observed at maximal effort (figure 3.8, lower left panel). Correlations between $\xi_3(t_i)$ and the vertical COM showed the opposite result: the lowest ranked athletes appeared to have larger correlation coefficients than the higher ranked athletes (figure 3.9, lower left panel). This relation correlated significantly with FIS-point ranking at both intensities (figure 3.8, lower right panel).

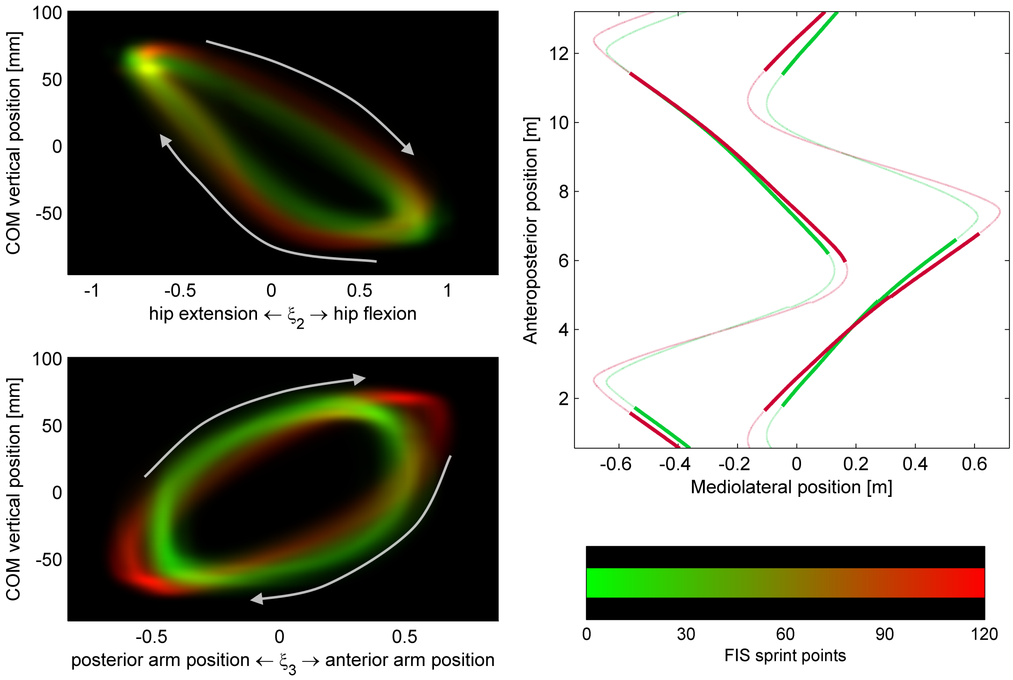

FIGURE 3.9: Top left panel: Vertical COM mass displacement showed a larger correlation with ξ_2 (representing hip flexion) for better skiers. Bottom left panel indicates that the opposite was true for ξ_3, which represented arm movement. Right panel: Ski trajectories of the three best ranked skiers (green lines) and the three lowest ranked skiers (red lines). It appeared that the best skiers started their gliding phase with a more lateral position of the ski, and finished in a more medial position. This plot is from the submaximal effort data set, but a similar pattern exists for the maximal effort data set.

3.6 Discussion

3.6.1 Findings

The findings of the current study support the hypothesis that even at the highest skill level systematic differences exist between the individual techniques of elite cross country skiers. This suggests that it is not only physiologic characteristics [2, 3], but also the skiing technique that distinguishes the best athletes from their peers.

Specifically, three aspects in the athletes techniques appeared to show a correlation to the athletes' ranking. The first aspect appeared as a timing difference in $\mathbf{pm}_2$, which captured a combination of hip flexion and aspects of the pole push. In higher ranked athletes this movement component was more correlated with the vertical COM motion (Figure 3.9, top left). These findings suggest that the best athletes coordinated their movements so that hip flexors and major muscle groups in the stomach necessary to perform $\mathbf{pm}_2$ worked in phase with release of potential energy. In contrast, the sagittal arm swing ($\mathbf{pm}_3$) was more correlated with vertical COM motion for the lower ranked skiers (Figure 3.9, bottom left). One interpretation of this is that these skiers to a smaller extent managed to coordinate major hip flexor muscles with the release of potential energy, and compensated by using the smaller extensor muscles in arms and shoulders.

This finding is consistent with some of the findings made in double poling by Holmberg et al. [7]. They observed that better skiers tended to have a smaller hip angle at the pole plant. They also suspected that better skiers were able to make use of potential energy more effectively, however, they were lacking a COM model to assess that suspicion. Due to the COM model used in the current study, a more explicit argument could be made.

The second technique aspect that correlated with the skiers' ranking was found as a difference in the amplitude of $\mathbf{pm}_3$, which captured a combination of sagittal-plane arm and pole movements and an ab/adduction of the hips. The differences in the $\mathbf{pm}_3$, together with specific features in the $\mathbf{pm}_4$ motion are likely the cause for slightly more bent ski trajectories (Figure 3.9, right), which enabled the best ranked skiers to better align their skis with the forward direction during the initial gliding phase, while showing a similar trajectory in the push-off phase. In the author's opinion, this difference in the ski trajectories affected the lateral COM motion, causing the better ranked skiers to exhibit a smaller lateral excursion (Figure 3.6 a).

All three aspects, better coordination of hip flexion and vertical COM motion, reduced lateral COM motion at the same forward propulsion, and straighter alignment of the skis in the gliding phase, are plausible potential causes that could lead to a more efficient skiing technique. However, while a causal relationship between principal movements and COM motion may be assumed (due to the definition of the COM), such a causal relationship between the technique differences and skier ranking can a priori not be assumed. A prospective study would be needed to prove that the observed technique differences can be improved by training and that these differences actually lead to a better skating performance. The hybrid movement patterns defined by equation 3.14 in the current paper may prove to be particularly useful in this context, since they offer a way of visualizing and thus effectively communicating technique differences to the athletes.

3.6.2 Method limitations

We argued that differences in the timing of movement components were caused by a different coordination of muscle activation. However, no measurements of muscle activation was performed, so such differences could not be directly observed. A possible extension to future studies could be to incorporate EMG measurements. Measurements of force (pole and plantar) could also add valuable information. Such studies has been performed in the classical DP technique [7], but no detailed studies incorporating both 3D kinematics, force and EMG measurements have yet been performed in the skating techniques.

PCA is a linear decomposition method. In this study it was applied to a system which perhaps is better represented in the angular domain. One possible improvement, suggested also by Troje [17], would be to represent the posture vector using joint or segment angles, instead of the Cartesian coordinates used in this study. However, for such calculations the exact joint locations are necessary. Otherwise, the computed angles are susceptible to errors, which might compromise results of the succeeding PCA.

The pooling procedure used in this study enabled a direct comparison of multi-segment movements between subjects. An individual-specific PCA could have revealed larger individual differences in technique, by defining subject specific principal movements. However, a direct comparison of the subjects would have been difficult. For that reason, the pooling procedure was deemed best suited for this study.

Finally, this study has been limited to analyse only dynamic movements. Static differences in posture, which is also a key aspect of technique, are not taken into account due to the normalization procedure. A possible extension to include both static and dynamic information in the analysis could be to follow the approach of Troje [17] more closely. He submitted both the average posture (static information), the dominant principal component vectors, and parameters that determined the time evolution coefficients (dynamic information) to a second PCA. With this approach, he assessed both static and dynamic differences in one comprehensive analysis. Such a method applied to this study would have resulted in an average technique, and principal component vectors that point in the directions of the largest technique variance within the athlete group. This would likely be highly effective to determine different technique strategies among the skiers.

Further limitations that are common to both this study and the IMU based study are discussed in the next chapter, followed by a combined conclusion of the two studies.

Chapter 4

Skiing technique assessed by inertial sensors

4.1 Introduction

The method described in chapter 3 is suitable when one has a large (but redundant) data set, most frequently available from measurements with 3D motion capture systems. However, the apparatus needed to do such measurements are both high cost, and large size. The measurement volume of this type of equipment is also limited, which in practice restricts many applications to a laboratory environment. Cross country skiing is an outdoor activity. Hence, any measurement system that can be used in the field will have a great advantage over a system that is restricted to the laboratory.

A system that shows potential to do such measurements in field, are suits embedded with inertial sensors. One such design has been developed by the commercial Xsens[1] company[27]. These suits often require movements that have periods of fixed contact with the ground (i.e. no sliding allowed), which is not the case for cross country skiing. However, Supej [28] showed that this suit could be combined with a high-end GPS unit. He tested the system on an alpine skiing course, and achieved an accuracy comparable (or better) than using traditional video based analysis. Still, there is an issue with the size, since high-end differential GPS receivers are relatively large size, and require the mounting of an antenna on the athletes back. This at least rules out the possibility to do in-competition measurements. Another issue is the cost of such equipment.

Although the cost of full body commercial sensor suits currently is rather high, mass production of miniature (MEMS[2]) inertial measurements units (IMUs) have made the

---

[1] Xsens Technologies B.V., P.O. Box 559, 7500 AN ENSCHEDE, THE NETHERLANDS

[2] Micro electro mechanical system

actual sensors low cost devices. Furthermore, these types of sensors are standard equipment in all current smart phones. Hence, a large part of the general public now have access to motion sensors, which potentially could be used to analyse movement patterns. Also, the sensors small size and light weight makes in-competition measurements a real prospect. Of course, the use of a single IMUs restrict the information we can collect. However, due to the availability of the sensors, it is tempting to study what information can in fact be determined by such a system.

4.2 Background

Several researchers have used single (or a few) IMUs to monitor human movement. Gait analysis has perhaps been the subject of most investigations [25, 29–32], but IMUs has also been applied to sport science[28, 33–36]. Two articles have this far used inertial sensors to investigate cross country skiing technique: Marsland et al. [37] investigated the use of a single IMU placed at the upper back, and concluded that they could visually identify what type of skiing technique was used from the sensor output. However, no algorithms for automatic detection of techniques were developed. Myklebust et al. [13] positioned a 3-axis accelerometer at the lower back (os sacrum), and concluded that the sensor was sensitive enough to record differences in the movement patterns of high level skiers. Also, they showed that individual skiers reproduced their own movement pattern, even when the measurements where separated by several months in time. Finally, they observed a difference in the vertical movement of the hip when comparing the V1 and the V2 techniques. They argued that this difference indicated a fundamental difference in way potential energy was utilized in the two techniques. This argument implied that the center of mass (COM) of the skiers was well approximated by the hip movement. They performed a 2D video analysis to investigate the relation of COM movements to hip movements, however, a proper 3D segmental analysis[29, 38] (SA) was not performed.

This study used a setup similar to that of Myklebust et al. [13], with one single IMU positioned at the athletes sacrum. However, the IMU used in this study also included a 3-axis gyroscope, which resulted in two improvements to the study by Myklebust et al. [13]: (1) the measurements of acceleration could be corrected to resemble measurements made in a laboratory reference frame, and (2) the measurements where not restricted to the translation of the pelvis, but included also rotations. Furthermore, measurements from the IMU could be directly compared with results from a 3D motion capture system (described in the previous chapter), enabling a validation of both the sensor accuracy, and a comparison to the COM trajectory as determined by a SA-model.

Positioning of the IMU at the sacrum (S1) was motivated by two factors: First, the COM was hypothesized to be located in proximity to S1. This has been investigated during gait by Floor-Westerdijk et al. [29], with the conclusion that the displacement of S1 and the COM (determined from a SA method) differed by $< 1\,\text{cm}$. The second arguments was more subjective, and was due to the authors perception that movements of the hip-region is considered a key aspect amongst XC-skiing practitioners.

The goals of this study was thus twofold: First we wanted to investigate the relation between pelvis movements and COM movements while roller skiing with the V2 technique. Second, we wanted to compare the movements recorded with the IMU to the results in chapter 3, and see if we could measure some of the same features that correlated with performance. Also, if the IMU revealed features that where not detected in chapter 3, a discussion of the relevance would be appropriate.

The first goal complemented the second to some degree, since several of the features that were revealed in chapter 3 were related to COM movements. For that reason, the relationship between the IMU measurements and the COM movements was considered to be of high interest. Although Floor-Westerdijk et al. [29] found that displacement of the S1 was a good indication of the COM displacement during gait, it is hypothesized in this study that the S1 movement and the COM movement does not correlate as well in the XC skiing V2 technique. This hypothesis was based on a larger range of motion for the pelvic region during V2 compared to gait. In particular, tilting of the pelvis was considered likely to affect the COM movement in both the vertical and anteroposterior directions. However, as pointed out earlier, an IMU can measure both pelvis orientation and translation. Therefore, this study also investigated whether information about the pelvis orientation could be used to improve COM estimates from the IMU, compared to the S1 displacement estimate alone.

4.3 Materials and Methods

The camera system has already been described in chapter 3, and the reader is referred to section 3.4.4 for details. The participants and testing procedure was also described in chapter 3, specifically sections 3.4.1-3.4.3.

The IMU was provided by Apertus (Apertus AS, Sykehusveien 3, 1385 Asker, Norway), and consisted of a triaxial vibratory MEMS gyroscope, and a triaxial MEMS accelerometer. The sensing elements where enclosed in a plastic casing with outer dimension $55 \times 38 \times 10\,\text{mm}$, and had a total mass of $25\,\text{g}$. Logging was done via a Bluetooth connection to a smart phone (Samsung Galaxy young) equipped with logging software developed by Apertus. Key specifications of the sensors are found in table 4.1.

TABLE 4.1: IMU specifications

Parameter	**Conditions**	**Value**	**Unit**
Sampling frequency (manufacturer)		100	[Hz]
Sampling frequency (measured)†		101.2	[Hz]
Clock frequency variation		± 1	[%]
Operating temperature range		−40 to +85	°C
Gyroscope			
Full scale range		± 250	[°/s]
Scale factor sensitivity		131	[LSB/(°/s)]
Scale factor variation	−40°C to +85°C	±2	[%]
Bias variation	−40°C to +85°C	± 20	[°/s]
Total RMS noise		0.05	[°/s]
Noise spectral density	At 10 Hz	0.005	[°/s/$\sqrt{\text{Hz}}$]
Nonlinearity	Best fit straight line, 25°C	0.2	[%]
Cross-Axis Sensitivity		± 2	[%]
Accelerometer			
Full scale range		± 2	[g]
Scale factor sensitivity		8192	[LSB/g]
Scale factor variation	−40°C to +85°C	±0.02	[%/°C]
Bias variation	0°C to 70°C	± 35 (60*)	[mg]
Noise spectral density	At 10 Hz	0.4 (0.6*)	[mg/$\sqrt{\text{Hz}}$]
Nonlinearity	Best fit straight line	0.5	[%]
Cross-Axis Sensitivity		± 2	[%]

† The sampling frequency appeared to differ from the value reported by the manufacturer. For that reason, the sampling frequency was measured experimentally by doing a long measurement of ten minutes, and comparing it to a more accurate clock.
* y-axis value in parenthesis

IMUs take measurements in a local coordinate frame that moves with the sensor housing. The mathematical foundation to transform the measurements from their local frame to some earth fixed frame is known as strapdown inertial navigation (SIN). This area is well researched[39], due to many commercial and military applications. However, understanding of the equations and theory behind SIN is not required to follow the argumentation and findings is this chapter. Therefore, this material has been moved to appendix A. In fact, the entire validation of the accuracy obtained from the IMU measurements has been relegated to appendix A, enabling this chapter to focus on what (skiing specific) conclusions can be drawn from the measurements.

4.3.1 Measurements

Measurements obtained from the IMU were the displacement of the sensor, denoted **S1**, along with its two first time derivatives, and the sensor orientation represented by the Euler angle vector $\boldsymbol{\theta} = (\theta_x, \theta_y, \theta_z)$. The axis system of the IMU was defined so that the y-axis pointed in the anterior direction, z-axis in the superior direction along the spine, while the x-axis completed the right handed coordinate frame. The Euler angles were based on a xyz-rotation order, so that θ_x represented pelvis tilt, θ_y lateral pelvis tilt, and θ_z pelvis rotation (see Figure 2.2, page 9).

To separate measurements based on inertial sensors from the marker based 3D motion capture system, a superscript $^{\mathrm{i}}$ was used to denote quantities obtained from inertial sensors, while $^{\mathrm{m}}$ represented quantities obtained from the marker based motion capture system. Capital letters XYZ denote the laboratory reference frame, while lower case xyz denote the IMU's local coordinate frame.

4.3.2 Data analysis

Twelve consecutive strides were analysed for each athlete at a given effort level, as described in the previous chapter. Each stride was re-sampled to 150 time points, using the cycle definition proposed in the introduction (Figure 1.1, page 2). The pole plants where detected by the 3D motion capture system as described in section 3.4.5, which in turn was synchronized with the IMU using the method described in section A.3 of the appendix.

COM models

In addition to the sacrum ($\mathrm{S1}^{\mathrm{i}}$) model, a simple model to improve the COM estimates from the IMU was developed. For this purpose, a three segment model representing the sagittal COM position of the skiers was chosen. This model was denoted $\mathrm{ES1}^{\mathrm{i}}$. The three segments were the upper body (ub), the thigh, and the shank (figure 4.1). In order to determine the COM of these segments using only output available from the IMU, three constraints was imposed on the system: (1) the ankle joint was assumed to be located directly under the sacrum, (2) the angle of the upper body with the vertical (θ_{ub}, figure 4.1) was assumed to move in phase with the pelvis tilt angle (θ_x^{i}) measured by the IMU, and (3) anthropometric differences between subjects were neglected.

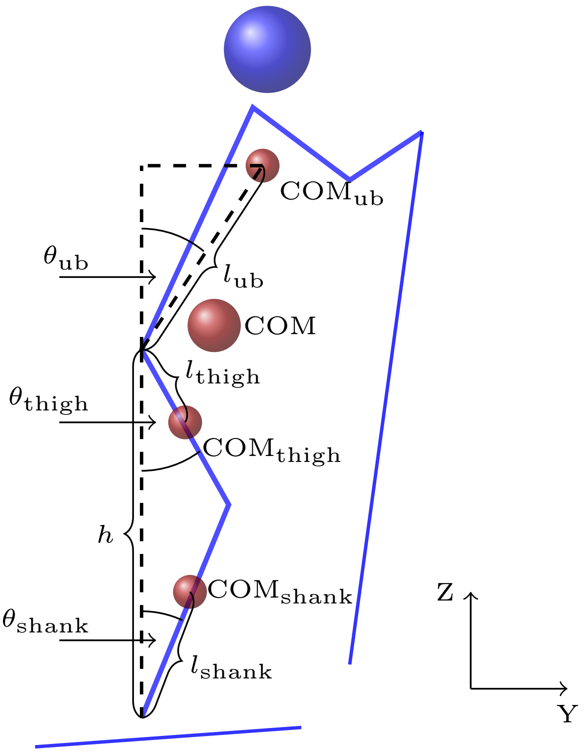

FIGURE 4.1: Simple three segment model for COM estimation in the sagittal plane. The three segments are shank, thigh, and upper body (ub). h is the vertical distance from the foot to the sacrum

Using vector notation, the COM of the skier could be approximated by the sum of the three segments, weighted by the mass m they represented:

$$\mathbf{COM} = \frac{m_{\text{shank}}\mathbf{COM}_{\text{shank}} + m_{\text{thigh}}\mathbf{COM}_{\text{thigh}} + m_{\text{ub}}\mathbf{COM}_{\text{ub}}}{m_{\text{shank}} + m_{\text{ub}} + m_{\text{ub}}} \tag{4.1}$$

To simplify the mathematical notation, we defined the mass vector $\mathbf{m}$ and displacement vectors $\mathbf{d}_Y$ and $\mathbf{d}_Z$:

$$\begin{aligned}
\mathbf{m} &= (m_{\text{shank}}, m_{\text{thigh}}, m_{\text{ub}}) \\
\mathbf{d_Y} &= (l_{\text{shank}} \sin\theta_{\text{shank}}, l_{\text{thigh}} \sin\theta_{\text{thigh}}, l_{\text{ub}} \sin\theta_{\text{ub}}) \\
\mathbf{d_Z} &= (l_{\text{shank}} \cos\theta_{\text{shank}}, l_{\text{thigh}}(1 - \cos\theta_{\text{thigh}}), l_{\text{ub}} \cos\theta_{\text{ub}})
\end{aligned} \tag{4.2}$$

Where l_{shank}, l_{thigh}, and l_{ub} are the distances between joints and the segment COM, as indicated in figure 4.1. Using this notation, equation 4.1 was rewritten into its antero-posterior (Y) and vertical (Z) components:

$$\begin{aligned}
COM_Y &= \frac{1}{||\mathbf{m}||}\mathbf{m} \cdot \mathbf{d}_Y + \mathrm{S1}_Y \\
COM_Z &= \frac{1}{||\mathbf{m}||}\mathbf{m} \cdot \mathbf{d}_Z + \mathrm{S1}_Z
\end{aligned} \tag{4.3}$$

Follwing constraint (1), it was possible to estimate the θ_{thigh} and θ_{shank}-angles, using knowledge of the vertical pelvis position h (figure 4.1), and the length of the thigh L_{thigh} and shank L_{shank} segments:

$$\begin{aligned} \theta_{\text{thigh}} &= \arccos\left(\frac{h^2 + L_{\text{thigh}} - L_{\text{shank}}}{2hL_{\text{thigh}}}\right) \\ \theta_{\text{shank}} &= \arccos\left(\frac{h^2 + L_{\text{shank}} - L_{\text{thigh}}}{2hL_{\text{shank}}}\right) \end{aligned} \tag{4.4}$$

By constraint (3), this implied that the only variable affecting the angles θ_{thigh} and θ_{shank} was the vertical position h of the sacrum. Furthermore, we restricted the model to measure only displacement. Hence, the vertical sacrum position h could be replaced by the displacement S1^{i}_{Z}, measured by the IMU, and equation 4.3 could be rewritten into the form:

$$\begin{aligned} COM_Y &= \mathcal{F}(\text{S1}^{\text{i}}_{Y}, \text{S1}^{\text{i}}_{Z}, \theta^{\text{i}}_{x}) \\ COM_Z &= \mathcal{F}(\text{S1}^{\text{i}}_{Z}, \theta^{\text{i}}_{x}) \end{aligned} \tag{4.5}$$

where the all variables could be measured by the IMU. The rest of the parameters in equation 4.3 were considered constants (constraint 3), and could be determined using knowledge of human anatomy, or by comparing the model to a more detailed COM model. In this study, the latter approach was chosen.

Acknowledging that this model is a very crude approach, it was considered sufficient to use a first order Taylor expansion in the implementation. Hence, the model to determine the COM in the vertical and antero-posterior directions was:

$$\begin{aligned} \text{ES1}^{\text{i}}_{Y} &= C_1\text{S1}^{\text{i}}_{Y} + C_2\text{S1}^{\text{i}}_{Z} + C_3\theta^{\text{i}}_{x} \\ \text{ES1}^{\text{i}}_{Z} &= C_4\text{S1}^{\text{i}}_{Z} + C_5\theta^{\text{i}}_{x} \end{aligned} \tag{4.6}$$

where the constants C_j were determined by minimizing the RMS difference between the ES1^{i} model and the 19 segment SA^{m} model described in chapter 3. The minimization was performed using the Nelder-Mead algorithm. The constants C_j were determined using statistical average values from all measurements. To eliminate bias caused by applying statistical values from a small sample size to the same sample, unique C_j were calculated for each trial k, by averaging over all trials except the k-th trial.

Feature extraction and statistics

Line density plots of the IMU measurements where calculated by the method described in 3.4.5, which allowed for identification of features that varied systematically with the athletes FIS-point ranking. Features that were identified using this approach was divided into three types: differences in timing (denoted with a τ), differences in amplitude (denoted α), and differences that where not adequately described using the two first approaches (denoted ϕ). Timing differences were quantified by an unbiased cross correlation of the time normalized measurements with the average measurement over all athletes, while amplitude was quantified as the peak-to-peak amplitude. Quantification of ϕ_{θ_z} was obtained by calculating the difference of the mean value of θ_z between $8 - 22\%$ and $58 - 72\%$ of the stride cycle.

Features of technique (α, τ or ϕ) that appeared to vary systematically with skill level were correlated (Pearson's correlation coefficient, r) against the athletes FIS-point ranking, as described in section 3.4.5. As in chapter 3, statistical significance was set at a p-value of $p < 0.05$, (denoted *). A p-value < 0.1 was considered a trend (denoted $^{\mathrm{T}}$)

4.4 Results

4.4.1 Assessment of COM models

Values of the weight coefficients C_j (equation 4.6) are found in table 4.2. Root mean square deviations between the SA^{m} model, the $\mathrm{ES1}^{\mathrm{i}}$, and the $\mathrm{S1}^{\mathrm{i}}$ model are displayed in table 4.3. The mean trajectories of the models for a typical subject is found in figure 4.2, along with the deviations of the IMU based models from the SA^{m} model.

TABLE 4.2: ES1 model coefficients

Coefficient	**Mean value**	**SEM**	**Unit**
C_1	0.28	0.04	[-]
C_2	0.21	0.01	[-]
C_3	0.00	0.02	[m/rad]
C_4	1.10	0.02	[-]
C_5	0.27	0.01	[m/rad]

The mean values were calculated by minimizing the RMS difference between SA^{m} and $\mathrm{ES1}^{\mathrm{i}}$ of all trials. The standard error of the mean (SEM) was obtained by minimizing the RMS difference for each trial separately. Due to the first order Taylor approximation in 4.6, units of m/rad was necessary for C_3 and C_5.

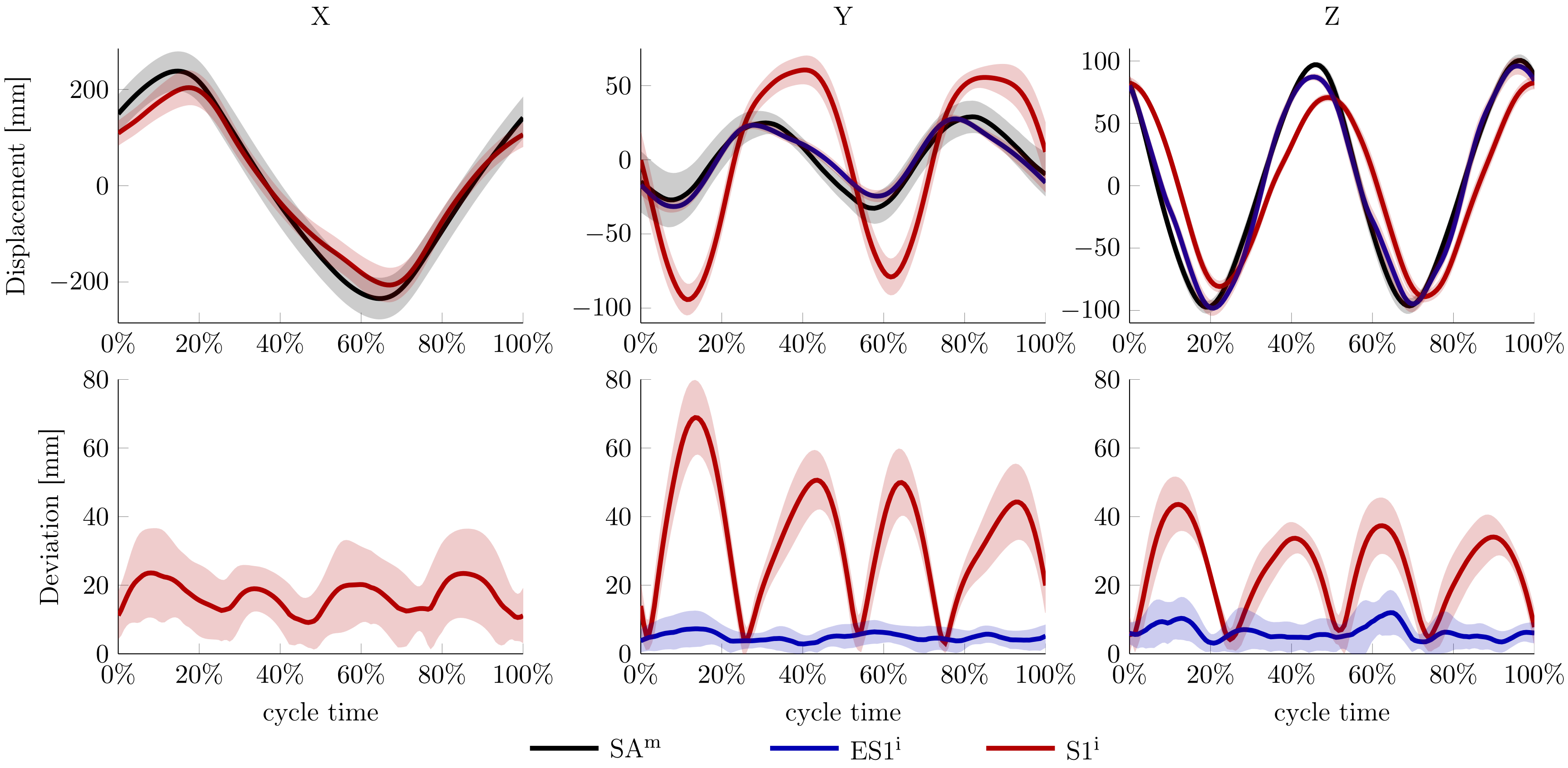

FIGURE 4.2: Top row: COM estimates from the SA^m model (black lines), and the IMU based $ES1^i$ (blue) and $S1^i$ (red) models for an example athlete. Lines represents the mean stride cycle, the shaded areas represent the cycle-to-cycle variability (standard deviation). Bottom row: Deviations of the IMU based models from the SA^m model (blue: $ES1^i$, red: $S1^i$). Lines represent the deviation of the mean stride cycles, averaged over all (11) measurements. Shaded area represents measurement-to-measurement variability (standard deviation).

TABLE 4.3: RMS deviation of IMU based COM models from the SA model.

Model	**X** [mm]		**Y** [mm]		**Z** [mm]	
$S1^i$	19 ± 5	(38 ± 16)	38 ± 6	(40 ± 7)	27 ± 4	(27 ± 5)
$ES1^i$			6 ± 2	(11 ± 7)	8 ± 2	$(\ 9 \pm 2)$

The main entries are deviations of each athletes average stride cycle (mean over all (11) measurements ± standard deviation). Values in parenthesis are RMS deviations during a single stride cycle (mean over all (132) strides ± standard deviation).

4.4.2 Assessment of the differences between skiers' techniques

A time shift in the vertical COM trajectory between the best ranked and the lower ranked skiers was apparent using both the $S1^i$ and $ES1^i$ models (Figure 4.3, left panel). This time shift correlated significantly with FIS-point ranking at both effort levels (Figure 4.4,left panel).

The amplitude of $S1_x$ also appeared to relate to FIS-point rating, where the best ranked skiers showed the smaller amplitude (Figure 4.3, upper right panel). The amplitude correlated significantly with FIS-point ranking at sub maximal effort level, and showed a trend at maximal effort (Figure 4.4, upper right panel).

The lower ranked skiers appeared to have a larger amplitude in the θ_z-angle during a short time period from $8 - 22\%$ and $58 - 72\%$, which corresponded approximately to the right and left leg push [6] (Figure 4.3, bottom right panel). However, statistical analysis revealed no significant correlation with FIS point ranking (Figure 4.4, bottom right panel).

No timing differences were observed in the pelvis tilt angle (θ_x).

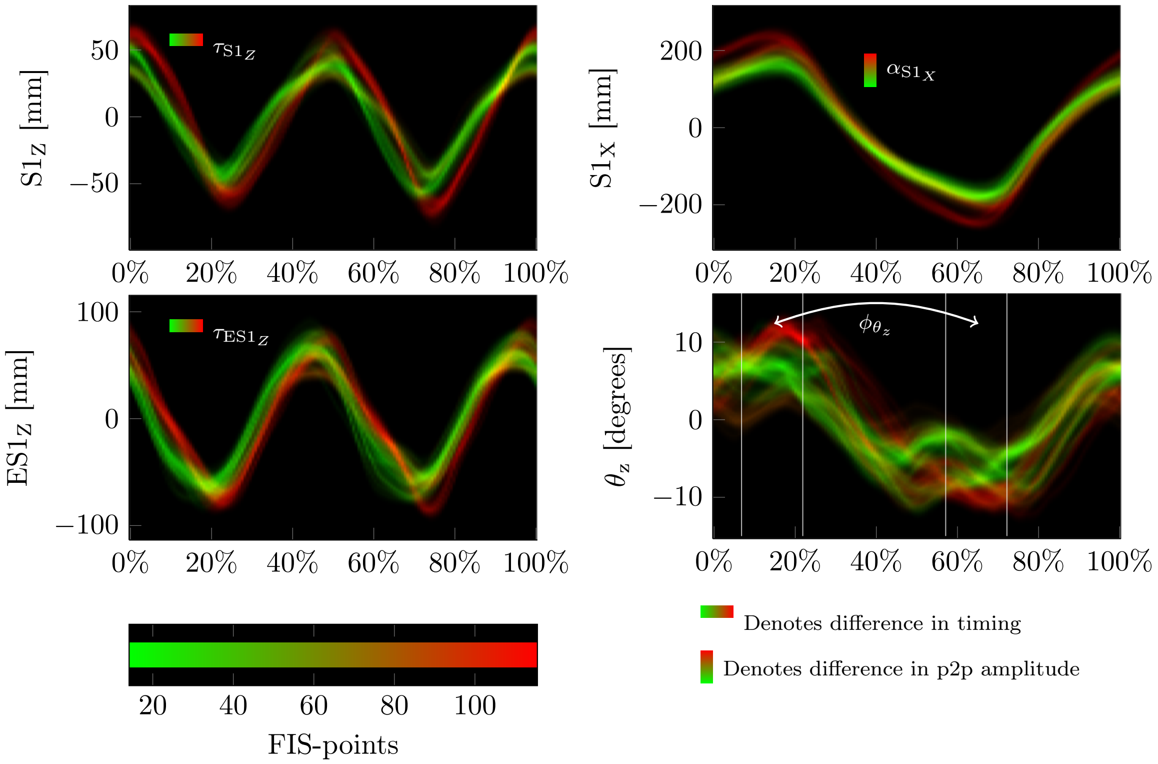

FIGURE 4.3: Line density plots of IMU COM models and θ_x movements. Areas where all skiers used the same technique appear yellow, green areas represent the top skiers, red areas represent the skiers with higher FIS-point rankings.

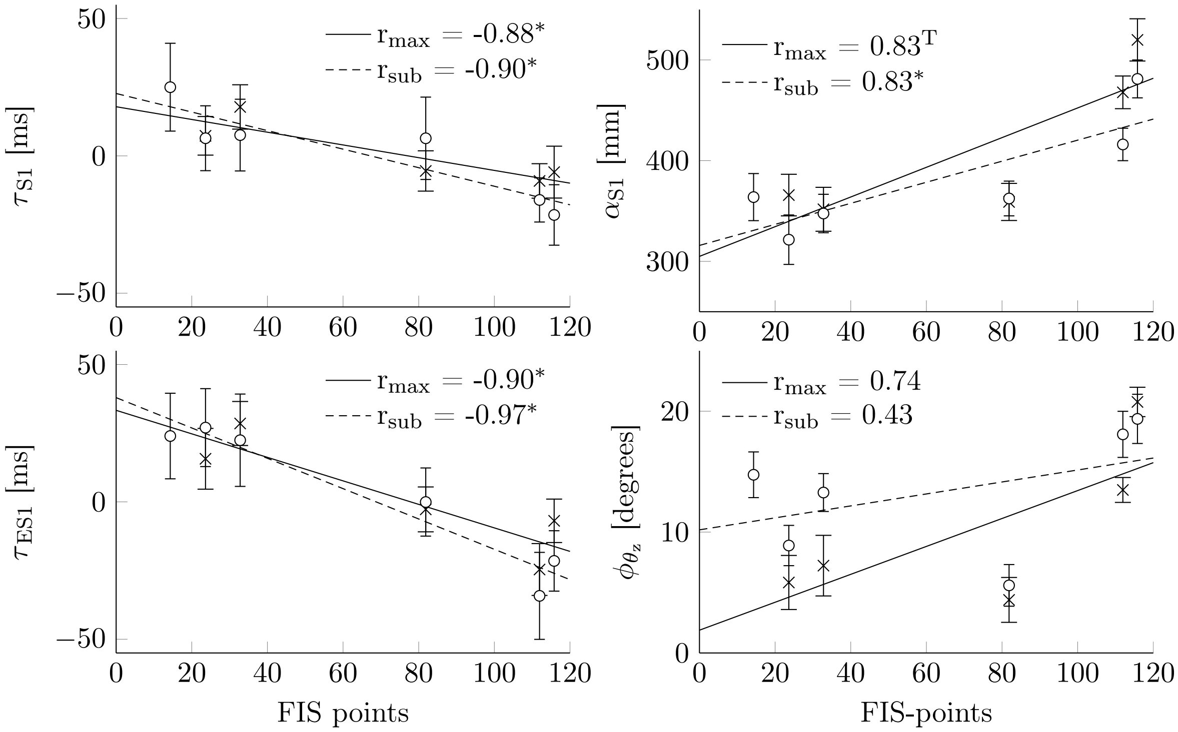

FIGURE 4.4: Correlations of technique features with FIS-point ranking. τ indicates a difference in timing, α a difference in amplitude. ϕ_{θ_z} denotes the mean amplitude between the white lines in Figure 4.3. x: maximal effort, o: submaximal effort

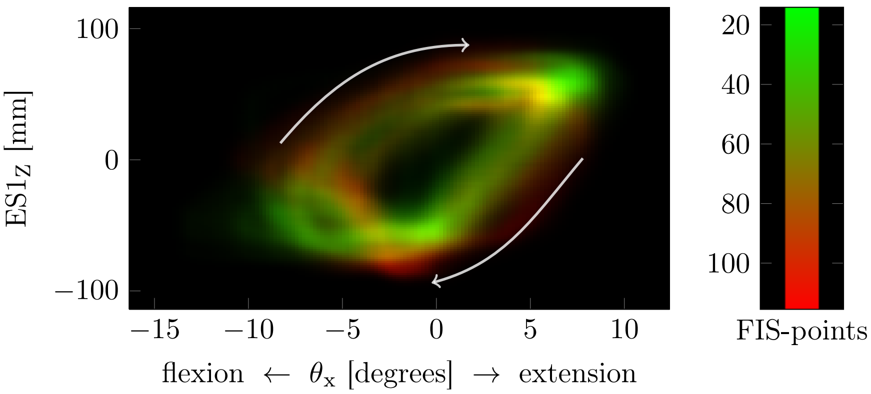

FIGURE 4.5: Line density plot of the pelvis tilt angle vs vertical COM, represented by the ES1 model. Better ranked skiers (green) appeared to have a larger correlation coefficient between the two time series

Relations between features of technique

Better ranked skiers appeared to have a higher correlation coefficient between their pelvis tilt angle (θ_x) and $ES1_Z$ (Figure 4.5), implying that the pelvis tilt and vertical COM movement was more synchronized in time. This relation correlated significantly with FIS-point ranking at maximal effort level, and qualified to a trend at sub maximal effort (Figure 4.6, left panel). Furthermore, the amplitude of the sideways S1 displacement (α_{S1_X}) showed a large correlation with the axial pelvis rotation during the push phase (ϕ_{θ_z}). This correlation was significant at maximal effort, and a trend at sub maximal effort (Figure 4.6, right panel).

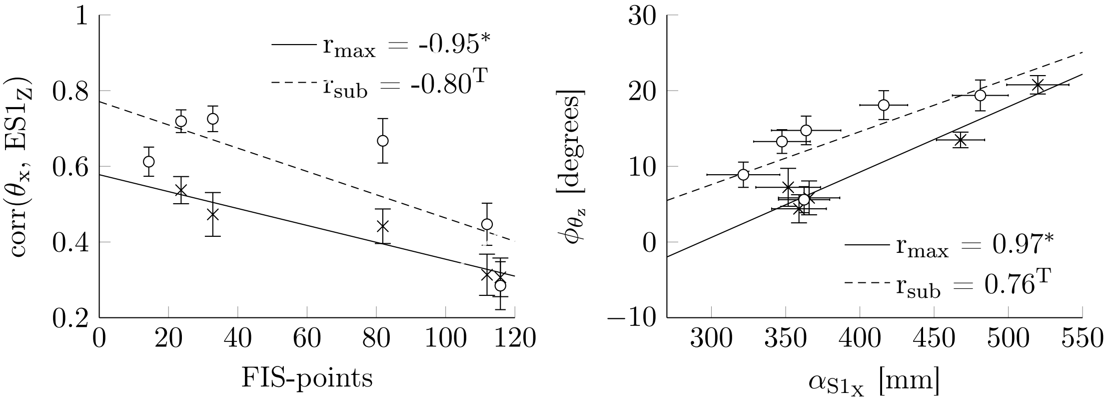

FIGURE 4.6: Left panel: better ranked skiers showed higher correlation coefficients between the pelvis tilt angle and vertical COM movement. Right panel: Sideways COM amplitude was highly correlated to the pelvis' axial rotation during the leg push. x: maximal effort, o: submaximal effort

4.5 Discussion

Due to the twofold purpose of this study, this discussion has two rather independent parts: (1) to discuss the validity of the two pelvis based COM models and (2) to discuss individual differences in technique.

4.5.1 Validity of COM models

The results presented in this study indicate that the sacrum model for COM estimation is not a valid model when applied to the XC-skiing V2 technique. The sacrum models COM movement satisfactory solely in the medio-lateral direction, where the sacrum and COM movements are in phase, and differ only slightly in amplitude. In the antero-posterior and vertical directions sacrum and COM movements are both out of phase, and the amplitudes differ substantially. However, this study also showed that the sacrum model could be extended with knowledge of the pelvis orientation, which resulted sagittal plane COM estimates that deviated $< 1\,\mathrm{cm}$ compared to a more detailed SA model.

The extended sacrum model was defined by inferring 3 constraints. The first constraint (restraining the ankle joint to be positioned directly under the sacrum) was probably the least realistic: the ankle moves both in the sagittal plane and the coronal plane in the V2 technique. For this reason, it is considered likely that an attempt to determine the model coefficients C_j by using anthropometric measures will give results that does not agree as well with the SA model. Arguably, fitting the coefficients using measurements from a more detailed model can correct for some of the constraints that the model was subjected to. For instance, if the angle between upper body COM and vertical (Figure 4.1) is not exactly in phase with the pelvis tilt angle (constraint 2), the C_3 and C_5 coefficients will have the optimal value to correct for the error in the constraint. This is of course under the assumption that the SA model corresponds to the true COM, and that the optimal solution was found during the numeric minimization.

The third constraint (neglection of anthropometric differences) could have been omitted by calculating subject specific model coefficients. Possibly, this could have improved the results. However, the aim of this study was to develop a model that can be used with input solely from one single inertial sensor. For that reason it was decided to use values based on the whole group, rather than making individual adaptations.

A further consideration is that all subjects in this study were elite skiers. Hence, it is reasonable to assume that their skiing styles are more similar than that of a group ranging from elite to recreational level subjects. If the method proposed in this study was applied to a group of skiers at more diverse levels, one must expect that this will influence the model coefficients, which again would likely give a larger deviation between the SA and ES1 model. For the same reason, the model coefficients presented in this study can not be assumed to have the same validity if applied to a group of recreational skiers.

Finally, the coefficients were determined by minimizing the RMS difference between the SA and ES1 model. This will ensure a model that is optimal in the RMS sense (again assuming that the SA model corresponds to the true COM, and that the optimal solution was found). However, this does not necessarily give an optimal model with respect to maximal deviations, or with respect to differentiation of the time series. The latter argument is especially important due to the relation between resultant force and linear acceleration of the COM. Therefore, it needs to be pointed out that the results presented here is restricted to COM displacement, and that no validation of COM acceleration has been attempted.

4.5.2 Differences in technique

The results in this study support the findings of Myklebust et al. [13], i.e. that a single IMU positioned at the sacrum is sensitive enough to record differences between skiers' movement patterns. Further, several of these features was directly related to findings described in chapter 3, which was based on substantially more detailed data. This indicates that a single inertial sensor can measure aspects of technique that are important to performance, and can be used to separate skiers even at an elite level.

Both the S1 and ES1 model revealed a time shift in the vertical COM trajectory, which corresponded to the results obtained from the SA-model described in chapter 3. As discussed in the previous section, the vertical S1 trajectory does not model COM satisfactory. However, both the S1 and ES1 model detected a similar time shift in the vertical trajectory. This suggests that the time shift was caused by movements in the legs, rather than tilting of the pelvis. This is further supported by no significant correlation between time shift in the pelvis tilt angle and FIS-point ranking. The result of these observations was that the best skiers had a higher correlation coefficient between their vertical COM trajectory (quantified by $\mathrm{ES1}_Z$), and the pelvis tilt. Arguably, this finding is closely related to the correlations between $\xi_2(t)$ and vertical COM (SA model) described in chapter 3. We speculate that the difference in coordination between upper body and lower body movements cause a more beneficial transfer of potential energy during the poling action, in the same way as suggested in chapter 3.

The best skiers showed a smaller sideways amplitude of the COM, as modelled by sacrum displacement. This feature was also observed and discussed using the SA model in chapter 3. Furthermore, this feature was closely linked to the pelvis orientation during the time of the leg push[6]. In the authors opinion, this close link is not surprising: a pelvis that is orientated with a large axial rotation during the leg push might influence the angling of the glide ski, again causing the larger lateral COM amplitude. This different angling of the skis was assessed qualitatively in Figure 3.9, and supports this hypothesis.

As discussed in chapter 3, a smaller lateral excursion of the COM at the same propulsion is likely to be a more beneficial skiing technique. However, it is not necessarily the optimal solution for all athletes. When skiing uphill, work against gravity needs to be done when moving in the forwards direction, while movement in the sideways direction is normally not not constrained by gravity. Hence, using less lateral COM excursion and a having a glide ski more aligned with the forward direction is a heavier gear, which perhaps is suitable for the very best skiers, but to demanding for others.

In chapter 1 it is pointed out that technique is *one* of the factors that influence performance. Hence, we should expect only a weak correlation between technique and performance, due to variations in other determinants. A major drawback in this study is thus the small sample size: any significant correlations with only 6 subjects needs to show a very strong correlation. For that reason, lack of statistical significance should not disqualify any features from further assessment. Neither should features whose correlations were deemed significant be judged important solely on that basis. Instead, interpretations of why these differences matter has been emphasized both in chapter 3 and the current study. Nonetheless, this thesis must be read mainly as a method study.

A final consideration is that both in this study and the study presented in chapter 3, skill level was quantified by FIS sprint point ranking. It is not obvious that elements of technique that are beneficial in sprint skiing are the same as those required for success in distance skiing. Hence, a correlation against FIS distance points might result in features that differ from the ones observed in these studies.

4.5.3 Prospects

The focus of this study was restricted to the V2 skiing technique, but there is no obvious reason why the same method should not apply to other skiing techniques. However, new studies are needed to confirm this.

The IMU proved able to capture differences in timing between upper body and lower body movements (from θ_x and $\mathrm{S1}_x$ / $\mathrm{ES1}_x$). Due to the similarity between the poling motion in the V2 skating technique and the classical double poling technique, we hypothesise that the features discussed in relation to use of potential energy in this study, also applies to double poling technique.

Furthermore, inertial sensors of similar quality that was used in this study is implemented in the hardware of all current smart phones. Hence, this kind of quantitative technique analysis might be made available at low cost for the general public, if the right software is installed on the device. Obviously, this is not only applicable to skiing, but also other sports or movement patterns. This possibility is discussed further in appendix B.

An obvious extension to this study would be to extend the amount of information by adding sensors at other body segments. For instance, the current measurements does not contain any information about the arm swing. Knowledge of the arm-movements could improve the COM model, and are also important aspects of skiing technique by themselves. However, as pointed out in the introduction to this study, commercial inertial sensor suits that can provide extensive measurements of human movement already exist[27]. The strength of the current study is the small size and low cost of the equipment, which suggests that these types of measurements can be performed in large volumes, both during regular training and in a competition situation.

Conclusion

Results in the two previous chapters suggest that coordination between major muscle groups related to hip flexion and vertical COM motion is important for performance in the V2 technique, and that this separates skiers even at an elite level. Furthermore, the best skiers showed a smaller lateral COM excursion while generating the same forward propulsion, which could indicate a more efficient technique. However, this observation can also be caused by the fact that a smaller lateral excursion is a heavier gear, which might not be optimal for the lower ranked skiers. Amplitude of the lateral COM excursion appeared to be linked to the axial rotation of the pelvis during the push phase, and to a more lateral position of the glide ski during approximately the same time period.

On a more general basis, both methods presented in chapter 3 and 4 proved able to reveal possible performance relevant features of technique in skiing. However, because of the small number of athletes included in these studies, and that athlete-specific adaptations might be of importance, the findings must be considered no more than interesting observations that can benefit from further scientific analysis.

In order to assess the claim of a different muscle activation coordination proposed in this thesis, further studies using EMG-equipment might be performed, preferentially in combination with motion capture equipment. It is emphasized that no causal relation between the features revealed in this thesis and skiing performance can be assumed. To prove such a relation, a prospective study were athletes train to improve the specific features must be conducted.

Another important limitation is that both studies excluded static differences in technique. These static differences might be just as performance relevant as the dynamics discussed in this thesis.

Appendix A

Validation of inertial sensors for technique analysis

A.1 Introduction

Motivation for use of inertial sensors to measure movement has already been made apparent in the previous chapter. What was not clarified in chapter 4 was how low grade inertial sensors can be used to provide high accuracy, drift free measurements of displacement. This has been subject to some investigation during the later years. Several researchers have found that measurements of displacement can be obtained with satisfactory accuracy, even when the IMU specifications report drift rates that suggests this is not feasible. This has been done by determining biomechanical and sport specific constraints that govern the movement, and then implementing these constraints in the inertial navigation algorithms [33, 35]. This study uses the same approach, however, the constraints that are used makes the method transferable to a large group of sports. The key limitations are that the movement patterns must be cyclic, with cycle durations $\sim 2\,\mathrm{s}$ or less, and that the average COM velocity is the same from cycle to cycle. Hence, others sports such as running, race walking and swimming might also be analysed using the same approach.

The main goal of this study is therefore to present a method that enables the use of low grade IMUs for technique analysis that applies to a large group of sports, and to validate the accuracy of such a method.

A.2 Theory

The equations and theory presented in this section is to a large extent based upon the textbook by Titterton and Weston [39].

A.2.1 Background

Inertial sensors are in the strict sense limited to two types of sensors: angular rate sensing devices (gyroscopes) and linear acceleration sensors (accelerometers). Combining these sensors into a inertial navigation system (INS) was first proposed by Boykow in the early 20. century [39, ch. 2.3]. During the 20. century there was a large amount of research on developing both high quality inertial sensors, and efficient INS algorithms. Lately, much attention has also been given to the development of miniature inertial sensors, abbreviated MEMS (micro electromechanical systems)[39, ch. 7]. These sensors have a very small size, and the production technique is highly suitable for mass production, making them low cost. Unfortunately, the specifications of the current low-grade MEMS inertial sensors are typically not good enough to construct a INS with acceptable accuracy for longer periods of time. However, if the system that is measured follows certain constraints, it might be feasible to use these types of sensors for short time inertial navigation.

Some different MEMS gyroscope designs have been developed. Most of them have in common that they are based on the *vibratory* gyroscope, and thus does not have the spinning mass of conventional gyroscopes. The vibratory gyro is based upon the principle of Coriolis acceleration. Different types of gyroscopes have been developed to utilize this phenomenon, both in MEMS and non-MEMS versions. Figure A.1 shows the working principle of one such design: the tuning fork gyroscope. The two ends are forced to vibrate at a certain amplitude A and angular frequency ω_r, but in opposite phase. If the tuning fork is rotated with an angular velocity ω_{in} about its sensitive axis (i.e. about the shaft), this will induce a Coriolis force F_c on the vibrating elements, following the relation:

$$F_c = 2m\omega_{in}A\omega_r\cos(\omega_r t) \tag{A.1}$$

where m is the mass of vibrating element. Since the two vibrating elements are in opposite phase, the Coriolis force will be in opposite direction, and in phase with the forced vibration modes. This will result in a measurable AC torque on the torsion bar, who's amplitude is proportional to the applied input angular velocity.

Accelerometers (in the conventional form) work by measuring the force working on some mass, referred to as a *proof mass*. Hence, an accelerometer in free fall (i.e. in an inertial frame) has an output equal to zero. Consequently, an accelerometer at rest on the surface

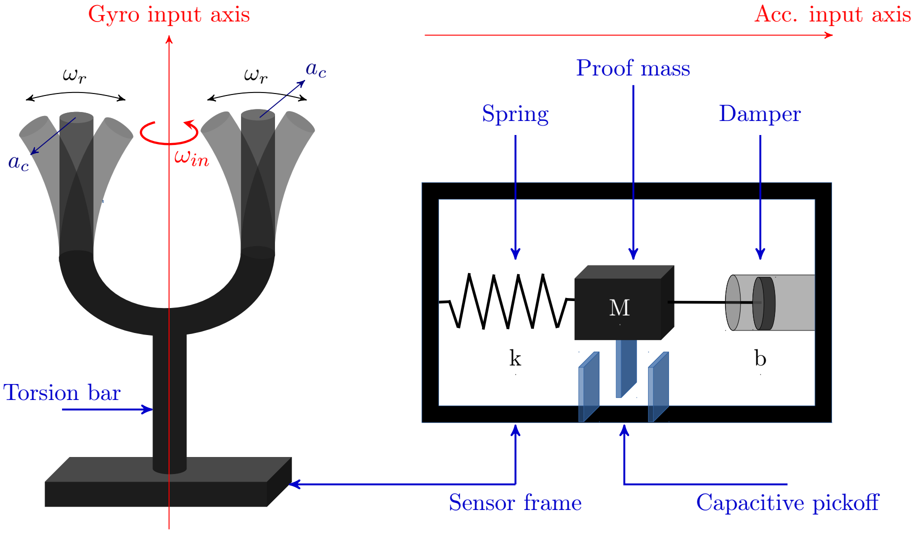

FIGURE A.1: Working principles of a vibratory gyroscope (left side) and accelerometer (right side). Both sensors are open loop. Gyroscope: the rods of the tuning fork are forced to vibrate in opposite phase, resulting in a Coriolis acceleration a_c of the rods when subject to a rotation about its sensitive axis. This will result in a torque that acts on the torsion bar. Accelerometer: The proof mass can be displaced along the sensitive axis. Due to the spring, the displacement is proportional to the applied linear acceleration (following Newtons 2. law). The displacement can be measured, for instance by a capacitive pickoff. (The illustrations are inspired by [39] and [40])

of the earth should have an output of $1g$ directed vertically upwards (i.e. the force exerted by the ground against gravity). The term *specific force* is frequently used to denote the output of an accelerometer. The specific force is then the sum of non-gravitational forces, divided by the proof mass[39, page 10]. Using Newtons 2. law, and knowledge of the spring constant k and damping coefficient b in figure A.1, it can be shown that the displacement of the proof mass (denoted x) is related to the specific force acting on the sensor frame (f) via the following equation[40]:

$$M\ddot{x}^2 + b\dot{x} + kx = Mf \tag{A.2}$$

It is apparent that the output of an accelerometer might produce an oscillatory output, due the the second order differential equation. For that reason, the damping coefficient is usually chosen so that the system is critically damped.

Most high end inertial sensors (both gyroscopes and accelerometers) actively suppress the displacements of the proof masses (called closed loop sensors). This solution offer better accuracy over a larger measurement range. However, this technique is still not common in low grade MEMS sensors, which operate using the open loop principle described in figure A.1.

A.2.2 Navigation frames

To make a successful INS it is necessary to have well defined reference frames. For the purpose of this study, we only need to define three reference frames: the *b-frame*, the *l-frame*, and the *sb-frame*.

The body frame (b-frame) is an orthogonal axis set where the axis move with the body it is attached to. Using anatomical terminology, it is customary to define axis that point in the anterior direction, lateral direction, and superior direction (Davis et al. [41]).

The lab frame (l-frame) is an earth fixed reference frame. Its origin is some point **r** on the surface of the earth (assumed to be relatively close to the origin of the body frame), whose axis move with the earth's surface. The z-axis point vertically upwards, while the x and y-axis are mutually orthogonal in the tangential horizontal plane.

The sb-frame (stabilized body frame) is an orthogonal axis set where the axis are fixed with respect to inertial space. For the purpose of this study, the l-frame is assumed to be an inertial frame. For that reason, the sb-frame differ from the l-frame only by a (constant) rotation of the axis system.

Notation: In addition to the notation specified in the introduction to this thesis, the following notation is used in this appendix:

- the dot-notation for time derivatives ($\frac{dt}{dt} = \dot{x}$ and $\frac{d^2t}{dt^2} = \ddot{x}$)
- a superscript denotes the frame of reference that a measurement is made ($\mathbf{q}^b$: vector quantity $\mathbf{q}$ expressed in the body frame)
- A matrix $\mathbf{C}$ transforming a vector from frame a to frame b is denoted $\mathbf{C}_a^b$

A.2.3 Strapdown inertial navigation equations

The IMU measures angular velocity $\boldsymbol{\omega}^b$ and specific force $\mathbf{f}^b$ in the b-frame. This frame can be related to the l-frame by a matrix multiplication:

$$\mathbf{q}^l(t) = \mathbf{C}_b^l(t)\mathbf{q}^b(t) \tag{A.3}$$

The 3×3 matrix $\mathbf{C}_b^l$ is called the *direction cosine* matrix, whose columns represent the unit vectors of the b-frame, projected onto the l-frame. Here $\mathbf{q}^b$ represents an arbitrary vector in the b-frame. Differentiating $\mathbf{C}_b^l$ with respect to time, we find (by definition):

$$\dot{\mathbf{C}}_b^l = \lim_{\delta t \to 0} \frac{\mathbf{C}_b^l(t + \delta t) - \mathbf{C}_b^l(t)}{\delta t} \tag{A.4}$$

The matrix $\mathbf{C}_b^l(t+\delta t)$ can be related to $\mathbf{C}_b^l(t)$ by multiplication of another direction cosine $\mathbf{A}(t)$, relating the b-frame at time t to the b-frame at time $t+\delta t$:

$$\mathbf{C}_b^l(t+\delta t) = \mathbf{C}_b^l(t) \cdot \mathbf{A}(t) \tag{A.5}$$

It can be shown that for small angle rotations, $\mathbf{A}(t)$ may be written as a skew symmetric matrix:

$$\mathbf{A}(t) = (\mathbf{I} + \boldsymbol{\delta\Psi}) \tag{A.6}$$

with $\mathbf{I}$ being the 3×3 identity matrix, and

$$\boldsymbol{\delta\Psi} = \begin{pmatrix} 0 & -\delta\theta_z & \delta\theta_x \\ \delta\theta_z & 0 & -\delta\theta_y \\ -\delta\theta_x & \delta\theta_y & 0 \end{pmatrix} \tag{A.7}$$

Here $\delta\theta_i$ represents a small rotation around one of the b-frame axis x,y or z. Putting the expression for $\mathbf{C}_b^l(t+\delta t)$ in eq. A.5 into eq. A.3, we obtain:

$$\dot{\mathbf{C}}_b^l = \mathbf{C}_b^l \lim_{\delta t \to 0} \frac{\boldsymbol{\delta\Psi}}{\delta t} \tag{A.8}$$

In the limit $\delta t \to 0$, $\boldsymbol{\delta\Psi}/\delta t$ is simply the skew symmetric form of the angular rate vector $\boldsymbol{\omega}_{lb}^b = [\omega_x, \omega_y, \omega_z]^{\mathrm{T}}$, which represents the turn rate of the b-frame with respect to the l-frame, expressed in body axes. Thus, the relation between the time evolution of the orientation of the b-frame with respect to the l-frame, and the turn rates expressed in body axis, is given by the differential equation:

$$\dot{\mathbf{C}}_b^l = \mathbf{C}_b^l \cdot \boldsymbol{\Omega}_{lb}^b \tag{A.9}$$

where

$$\boldsymbol{\Omega_{lb}^b} = [\boldsymbol{\omega_{lb}^b}]_\times = \begin{pmatrix} 0 & -\omega_z & \omega_x \\ \omega_z & 0 & -\omega_y \\ -\omega_x & \omega_y & 0 \end{pmatrix} \tag{A.10}$$

Relation to Euler angles

A transformation from one reference frame to another can be represented by three successive rotations about different axis. A sub group of these kind of rotations are known as Euler angles, which is made up of twelve different rotation conventions. For the application to anatomical angles, the following Euler angle convention was suggested by Davis et al. [41] (starting from the l-frame):

1. rotate an angle θ_x about the l-frame x-axis
2. rotate an angle θ_y about the new y-axis
3. rotate an angle θ_z about the new z-axis

The rotations about these axis can be expressed via the three direction cosines:

$$\mathbf{C}_x(\theta_x) = \begin{pmatrix} 1 & 0 & 0 \\ 0 & \cos\theta_x & \sin\theta_x \\ 0 & -\sin\theta_x & \cos\theta_x \end{pmatrix} \tag{A.11}$$

$$\mathbf{C}_y(\theta_y) = \begin{pmatrix} \cos\theta_y & 0 & -\sin\theta_y \\ 0 & 1 & 0 \\ \sin\theta_y & 0 & \cos\theta_y \end{pmatrix} \tag{A.12}$$

$$\mathbf{C}_z(\theta_z) = \begin{pmatrix} \cos\theta_z & \sin\theta_z & 0 \\ -\sin\theta_z & \cos\theta_z & 0 \\ 0 & 0 & 1 \end{pmatrix} \tag{A.13}$$

A transformation from laboratory to body axis is then given by the direction cosine $\mathbf{C}_l^b = \mathbf{C}_z\mathbf{C}_y\mathbf{C}_x$. Since the direction cosines are orthonormal, the inverse transform, i.e. the transform from body to laboratory axis, is simply given by the transpose of $\mathbf{C}_l^b$:

$$\mathbf{C}_b^l = \mathbf{C}_l^{b\mathrm{T}} \tag{A.14}$$

Writing out $\mathbf{C}_b^l$, we find:

$$\mathbf{C}_b^l = \begin{pmatrix} \cos\theta_y\cos\theta_z & \cos\theta_z\sin\theta_x\sin\theta_y - \cos\theta_x\sin\theta_z & \sin\theta_x\sin\theta_z + \cos\theta_x\cos\theta_z\sin\theta_y \\ \cos\theta_y\sin\theta_z & \cos\theta_x\cos\theta_z + \sin\theta_x\sin\theta_y\sin\theta_z & \cos\theta_x\sin\theta_y\sin\theta_z - \cos\theta_z\sin\theta_x \\ -\sin\theta_y & \cos\theta_y\sin\theta_x & \cos\theta_x\cos\theta_y \end{pmatrix} \tag{A.15}$$

From this we can compute the Euler angles, as defined above, using the following relations:

$$\begin{aligned}\theta_x &= \arctan\left(\frac{C_{3,2}}{C_{3,3}}\right)\\ \theta_y &= -\arcsin(C_{3,1})\\ \theta_z &= \arctan\left(\frac{C_{2,1}}{C_{1,1}}\right)\end{aligned} \tag{A.16}$$

where $C_{i,j}$ represents the i,j-th element of the $\mathbf{C}_b^l$-matrix

Navigation from specific force measurements

The transformation matrix $\mathbf{C}_b^l$ allows us to transform the measurements of specific force $\mathbf{f}$ from the b-frame to the l-frame. The acceleration of the b-frame with respect to the l-frame can be expressed in terms of the specific force measurements and the direction cosine in the following way [39, chapt 3]:

$$\ddot{\mathbf{p}}^l = \mathbf{C}_b^l \mathbf{f}^b - 2\boldsymbol{\omega}_{ie}^l \times \mathbf{v}_l^l + \mathbf{g}^l - \boldsymbol{\omega}_{ie}^l \times \left(\boldsymbol{\omega}_{ie}^l \times \mathbf{r}\right) \tag{A.17}$$

The shaded terms are corrections due to the earth's rotation: the light gray term corrects for the Coriolis acceleration, the dark gray term corrects for the centripetal acceleration. $\boldsymbol{\omega}_{ie}^l$ represents the angular rate vector of the earth with respect to an inertial frame, and $\mathbf{v}_l^l$ is the velocity of the b-frame with respect to the l-frame. $\mathbf{g}^l$ is the gravity vector, and $\mathbf{r}$ is a vector from the center of the earth to the origin of the lab frame. In this study we used sensors with low end specifications, and analysed systems moving at relatively low velocities ($|\mathbf{v}_l| < 5\,\mathrm{m/s}$). For that reason, the correction terms in equation A.17 can be ignored, and the navigation equation reduces to:

$$\ddot{\mathbf{p}}^l = \mathbf{C}_b^l \mathbf{f}^b + \mathbf{g}^l \tag{A.18}$$

The direction cosine $\mathbf{C}_b^l$ is updated in accordance with equation A.9, where $\boldsymbol{\Omega}_{lb}^b$ is the skew symmetric form of the angular rate vector of the b-frame with respect to the l-frame ($\boldsymbol{\omega}_{lb}^b$). This rate vector is related to the angular rate vector sensed by a gyroscope ($\boldsymbol{\omega}_{ib}^b$) through the equation:

$$\boldsymbol{\omega}_{lb}^b = \boldsymbol{\omega}_{ib}^b - \mathbf{C}_l^b \boldsymbol{\omega}_{ie}^l \tag{A.19}$$

For the purpose of this study the turn rate of the earth is neglected, because the sensors are not able to measure angular rates to this accuracy. Thus, the turn rates of the b-frame with respect to the l-frame is considered to be equivalent to the gyroscope output:

$$\boldsymbol{\omega}_{lb}^b = \boldsymbol{\omega}_{ib}^b \tag{A.20}$$

Using the result from equation A.18, the velocity and position of the b-frame can be expressed in the l-frame from the following equations:

$$\begin{aligned}\dot{\mathbf{p}}^l &= \int_{t_0}^{t_f} \ddot{\mathbf{p}}^l(t) + \dot{\mathbf{p}}^l(t_0) \\ \mathbf{p}^l &= \int_{t_0}^{t_f} \dot{\mathbf{p}}^l(t) + \mathbf{p}^l(t_0)\end{aligned} \tag{A.21}$$

where $\dot{\mathbf{p}}^l(t_0)$ and $\mathbf{p}^l(t_0)$ are the initial values of the velocity and position.

A.2.4 Alignment with the horizontal plane

If the IMU is stationary in the l-frame, the accelerometers will measure only the gravity vector (neglecting the centripetal acceleration correction term (eq A.17) due to the earth's rotation). From these measurements, one can solve a set of equations to align the z-axis of the IMU with the direction of the gravity vector. The geometry of the problem is apparent from figure A.2. If we imagine that we can physically rotate the system, the alignment procedure can be visualized in the following way:

1. Measure the specific force in body axis ($\mathbf{f}^b(t_1)$)
2. Determine the angle θ_x from:

$$\theta_x = \arctan\frac{f_y^b(t_1)}{f_z^b(t_1)} \tag{A.22}$$

3. Rotate the system an angle θ_x about the b-frame x-axis
4. Make a new measurement of the specific force $\mathbf{f}^b(t_2)$
5. Determine the angle θ_y

$$\theta_y = \arctan\frac{f_x^b(t_2)}{f_z^b(t_2)} \tag{A.23}$$

6. Rotate the system an angle $-\theta_y$ about the b-frame y-axis

Following this procedure, the IMU z-axis will be aligned with the gravity vector, and the x and y axis will be aligned with the horizontal plane. The direction of the axis in the horizontal plane can in theory be calculated by using a technique called gyrocompassing[39]. However, as this requires a gyroscope that is accurate enough to measure the earth's rotation, it is not applicable to the sensor used in this study.

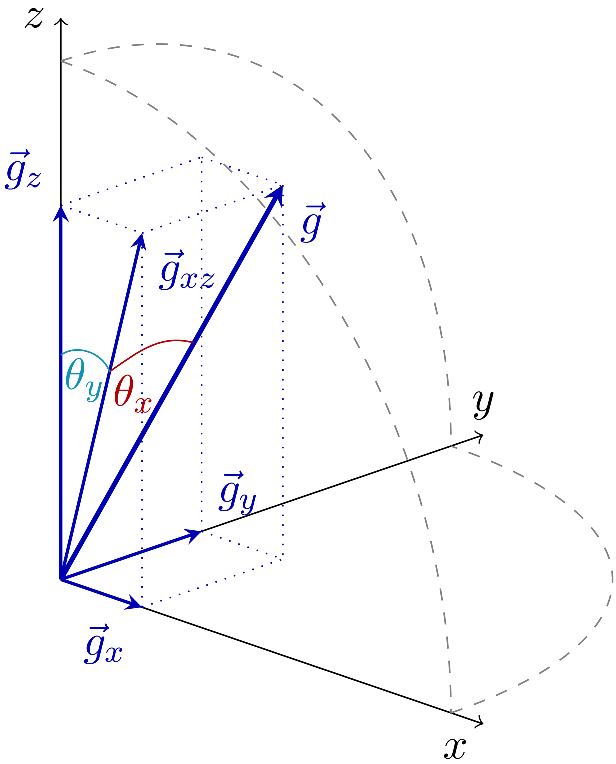

FIGURE A.2: Alignment of IMU z-axis with the gravity vector $\vec{g}$. The angle θ_x is related to the gravity components by $\tan\theta_x = g_y/g_z$, while θ_y can be related by $\tan\theta_y = g_x/g_z$

A.2.5 Computations

Orientation

In order to update the orientation of the IMU, the differential equation A.9 needs to be solved. From one computer update k, to the next update $k+1$, the solution to this equation can be written as:

$$\mathbf{C}_{k+1} = \mathbf{C}_k \exp\left(\int_{t_k}^{t_{k+1}} \mathbf{\Omega} \mathrm{d}t\right) \tag{A.24}$$

Assuming that the direction of the turn rate vector $\boldsymbol{\omega^i}$ remains fixed in inertial space over the time $\Delta t = t_{k+1} - t_k$, the integral can be written as:

$$\int_{t_k}^{t_{k+1}} \mathbf{\Omega} \mathrm{d}t = [\boldsymbol{\sigma}_\times] \tag{A.25}$$

where $[\boldsymbol{\sigma}_\times]$ is the skew symmetric form of the angle vector $\boldsymbol{\sigma}$. This vector has direction which specifies the rotation axis, and its magnitude is equal to the angle of rotation. Hence, equation A.24 reduces to:

$$\mathbf{C}_{k+1} = \mathbf{C}_k \mathbf{A}_k \tag{A.26}$$

with $\mathbf{A}_k = \exp\left([\boldsymbol{\sigma}_\times]\right)$. This exponential can be written as an expansion based on the definition of $\exp(\mathbf{x})$:

$$\mathbf{A}_k = \mathbf{I} + [\boldsymbol{\sigma}_\times] + \frac{[\boldsymbol{\sigma}_\times]^2}{2!} + \frac{[\boldsymbol{\sigma}_\times]^3}{3!} + \frac{[\boldsymbol{\sigma}_\times]^4}{4!} + \dots \tag{A.27}$$

From the shape of $[\boldsymbol{\sigma}_\times]$, it can be shown that $[\boldsymbol{\sigma}_\times]^n$ abides the following recursive relation:

$$\begin{aligned}
[\boldsymbol{\sigma}_\times] &= \begin{pmatrix} 0 & -\sigma_z & \sigma_y \\ \sigma_z & 0 & -\sigma_x \\ -\sigma_y & \sigma_x & 0 \end{pmatrix} \\
[\boldsymbol{\sigma}_\times]^2 &= \begin{pmatrix} -(\sigma_y^2+\sigma_z^2) & \sigma_x\sigma_y & \sigma_x\sigma_z \\ \sigma_x\sigma_y & -(\sigma_x^2+\sigma_z^2) & \sigma_y\sigma_z \\ \sigma_x\sigma_z & \sigma_y\sigma_z & -(\sigma_x^2+\sigma_y^2) \end{pmatrix} \\
[\boldsymbol{\sigma}_\times]^3 &= -\left(\sigma_x^2+\sigma_y^2+\sigma_z^2\right)[\boldsymbol{\sigma}_\times] \\
[\boldsymbol{\sigma}_\times]^4 &= -\left(\sigma_x^2+\sigma_y^2+\sigma_z^2\right)[\boldsymbol{\sigma}_\times]^2 \\
&\vdots
\end{aligned}$$

writing $\sigma^2 = \sigma_x^2+\sigma_y^2+\sigma_z^2$, we can rewrite $\mathbf{A}_k$:

$$\mathbf{A}_k = \mathbf{I} + \left(1 - \frac{\sigma^2}{3!} + \frac{\sigma^4}{5!} - \dots\right)[\boldsymbol{\sigma}_\times] + \left(\frac{1}{2!} - \frac{\sigma^2}{4!} + \frac{\sigma^4}{6!} - \dots\right)[\boldsymbol{\sigma}_\times]^2 \tag{A.28}$$

which can be written as:

$$\mathbf{A}_k = \mathbf{I} + \frac{\sin\sigma}{\sigma}[\boldsymbol{\sigma}_\times] + \frac{1-\cos\sigma}{\sigma^2}[\boldsymbol{\sigma}_\times]^2 \tag{A.29}$$

If this equation was implemented perfectly, and the assumption that the rotation axis remains fixed during one computer update is true, the computed orientation would be exact. In order to implement the equation A.29 in any practical situation, the functions will have to be truncated at some order in equation A.28. Defining:

$$\begin{aligned}
a_1 &= 1 - \frac{\sigma^2}{3!} + \frac{\sigma^4}{5!} - \dots \\
a_2 &= \frac{1}{2!} - \frac{\sigma^2}{4!} + \frac{\sigma^4}{6!} - \dots
\end{aligned}$$

then equation A.28 can be written as:

$$\mathbf{A}_k = \mathbf{I} + a_1[\boldsymbol{\sigma}_\times] + a_2[\boldsymbol{\sigma}_\times]^2 \tag{A.30}$$

a_1 and a_2 can then be truncated after a certain number of terms in order to achieve a desired accuracy. Including just the first term of a_1 gives a first order algorithm, truncating both a_1 and a_2 after the first term gives a second order algorithm.

A.2.6 Propagation of errors

Orientation algorithm truncation errors

If we denote the computed attitude matrix by $\hat{\mathbf{A}}_k$, assumed to be truncated at some order, and the true attitude matrix by $\mathbf{A}_k$, then we can define an error matrix $\mathbf{E}$:

$$\mathbf{E} = \mathbf{A}^T \hat{\mathbf{A}} - \mathbf{I} \tag{A.31}$$

From equation A.29 and A.30, we find that:

$$\begin{aligned} \mathbf{E} = \left(\sigma a_1 \cos\sigma - \sin\sigma + \sigma^2 a_2 \sin\sigma\right) \frac{[\boldsymbol{\sigma}_\times]}{\sigma} + \ldots \\ \left(1 - \cos\sigma - \sigma a_1 \sin\sigma + \sigma^2 a_2 \cos\sigma\right) \frac{[\boldsymbol{\sigma}_\times]^2}{\sigma^2} \end{aligned} \tag{A.32}$$

The first term will have the form of a skew symmetric matrix (from the $[\boldsymbol{\sigma}_\times]$-term), while the second term is a symmetric matrix (following $[\boldsymbol{\sigma}_\times]^2$). Thus, the error matrix can be written at the sum of a skew matrix $\mathbf{U}$, and a symmetric matrix $\mathbf{S}$.

Since $\mathbf{A}$ is an orthogonal matrix, the relation $\mathbf{A}^T\mathbf{A} = \mathbf{I}$ is satisfied. For the computed matrix, this implies:

$$\begin{aligned} \hat{\mathbf{A}}^T \hat{\mathbf{A}} &= [\mathbf{I} + \mathbf{E}^T][\mathbf{I} + \mathbf{E}] \\ &\approx \mathbf{I} + \mathbf{E} + \mathbf{E}^T \end{aligned} \tag{A.33}$$

Where we have terms higher than first order of the error matrix. Using that $\mathbf{S}^T = \mathbf{S}$ and$\mathbf{U}^T = -\mathbf{U}$, we find:

$$\hat{\mathbf{A}}^T \hat{\mathbf{A}} = \mathbf{I} - 2\mathbf{S} \tag{A.34}$$

$$\mathbf{A}^T \hat{\mathbf{A}} = \mathbf{I} + \mathbf{S} + \mathbf{U} \tag{A.35}$$

From A.34 it is apparent that $\mathbf{S}$ describes the deviation of $\hat{\mathbf{A}}$ from orthogonal form. If $\mathbf{S}$ is zero, then $\hat{\mathbf{A}}$ is an orthogonal matrix. $\mathbf{U}$ will then be a measure of the difference between the rotations given by $\hat{\mathbf{A}}$ and $\mathbf{A}$. A measure of the drift of the computed orientation matrix, denoted D_{dc}, can be represented by the root sum square of the upper or lower off diagonal elements of $\mathbf{U}$, divided by the update interval dt. Assuming rotation about the x-axis only (i.e $\boldsymbol{\sigma} = [\sigma,\ 0,\ 0]^T$), the drift term is given by:

$$D_{\mathrm{dc}} = \frac{1}{dt}\left(\sigma a_1 \cos\sigma - \sin\sigma + \sigma^2 a_2 \sin\sigma\right) \tag{A.36}$$

Rotation angle errors

In section A.2.5 the equations were based on the assumption that the direction of the rotation angle vector $\boldsymbol{\sigma}$ was constant during a computer cycle. If this was true, then $\boldsymbol{\sigma}$ could be computed by evaluating the integral:

$$\boldsymbol{\sigma} = \int_{t_k}^{t_{k+1}} \boldsymbol{\omega}\,\mathrm{d}t \tag{A.37}$$

In general, this assumption is not true, and we have:

$$\dot{\boldsymbol{\sigma}} = \boldsymbol{\omega} + \dot{\boldsymbol{\varepsilon}} \tag{A.38}$$

where $\boldsymbol{\omega}$ is the measurable angular motion, and $\dot{\boldsymbol{\varepsilon}}$ a component of the angular motion that is not possible to measure using inertial sensors. This error is frequently referred to as a *coning*-error, because the effect is most prominent when a single axis of a body spans a cone in space. The coning error is reduced with increased sampling frequency, but can also be reduced by applying an estimate of $\boldsymbol{\varepsilon}$. A method for estimating $\boldsymbol{\varepsilon}$ was proposed by Savage [42]. Defining $\boldsymbol{\delta\alpha}$ to be the estimate of $\boldsymbol{\varepsilon}$, he proposed the following correction:

$$\boldsymbol{\delta\alpha} = \int_{t_k}^{t_{k+1}} \boldsymbol{\alpha} \times \boldsymbol{\omega}\,dt \tag{A.39}$$

where:

$$\boldsymbol{\alpha} = \int_{t_k}^{t_{k+1}} \boldsymbol{\omega}\,dt \tag{A.40}$$

The rotation angle is then given by $\boldsymbol{\sigma} = \boldsymbol{\alpha}_{k+1} + \boldsymbol{\delta\alpha}_{k+1}$.

Magnitude of coning error

It can be shown that if a body oscillates about two axis, following the angular rate vector

$$\boldsymbol{\omega} = 2\pi f[\theta_x \cos 2\pi ft \quad \theta_y \cos(2\pi ft + \phi) \quad 0]^T$$

then a drift term about the z-axis will arise, according to the following relation: [39, chapt 11]

$$\dot{\varepsilon}_z = \pi f \theta_x \theta_y \sin\phi \left(1 - \frac{\sin 2\pi f dt}{2\pi f dt}\right) \tag{A.41}$$

Here θ_x and θ_y is the amplitude of the oscillations about the x and y axis, and$f$ is the frequency of the oscillations. The two oscillations differ in phase by ϕ, and dt is the computer update time. Hence, equation A.41 can be used to estimate the effect of drift in orientation due to coning motion, given initial estimates of the systems behaviour. If the drift term is negligible compared to the performance requirements, the correction term in equation A.39 can be omitted.

Position algorithm truncation errors

Sensor bias errors

From the equations A.21 and A.9, it is obvious that any bias in the accelerometer or gyroscope measurements will cause the orientation, acceleration, velocity and position to drift over time. A simplified analytical assessment of the propagation of errors can be done in the short time limit ($\Delta t << 84.4$ minutes, the Schuler period [39, chapt 12]).

Assuming a constant bias in the all angular rate measurements, denoted $\delta\omega$, we should expect a drift in the orientation estimate according to:

$$\delta\theta = \delta\omega \cdot t \tag{A.42}$$

Any drift about the vertical axis in the l-frame will not result in a misalignment with the gravity vector, but a drift about the two horizontal axis will. Thus, the drift in acceleration measurements due to gyroscope bias can be modelled as (using $\sin\theta \approx \theta$ and $\cos\theta \approx 1-\theta^2$):

$$\delta\ddot{\mathbf{p}} = \begin{pmatrix} g\delta\omega t \\ g\delta\omega t \\ \sqrt{2}g\delta\omega^2 t \end{pmatrix} \tag{A.43}$$

Assuming also a uniform bias in the acceleration values (δ_a), originating in the measurements from the accelerometer, we obtain the following estimates for drift in velocity and position:

$$\delta\dot{\mathbf{p}} = \begin{pmatrix} g\delta\omega\frac{t^2}{2} + \delta_a t \\ g\delta\omega\frac{t^2}{2} + \delta_a t \\ \sqrt{2}g\delta\omega^2\frac{t^2}{2} + \delta_a t \end{pmatrix} \qquad \delta\mathbf{p} = \begin{pmatrix} g\delta\omega\frac{t^3}{6} + \delta_a\frac{t^2}{2} \\ g\delta\omega\frac{t^3}{6} + \delta_a\frac{t^2}{2} \\ \sqrt{2}g\delta\omega^2\frac{t^3}{6} + \delta_a\frac{t^2}{2} \end{pmatrix} \tag{A.44}$$

A.2.7 Cross correlations

In the discrete domain, a cross correlation between two functions f and g is defined as:

$$(f \star g)[m] := \sum_{n=-\infty}^{\infty} f^*[n]g[n+m] \tag{A.45}$$

If the functions are not of infinite length, then one can also the define the *biased* and the *unbiased* cross correlations:

$$(f \star g)_{\text{biased}}[n] = \begin{cases} \dfrac{1}{N} \displaystyle\sum_{n=0}^{N-m-1} f^*[m]g[n+m] & \text{if } m \geq 0 \\ \dfrac{1}{N} \displaystyle\sum_{n=0}^{N+m-1} f^*[n-m]g[m] & \text{if } m < 0 \end{cases} \tag{A.46}$$

$$(f \star g)_{\text{unbiased}}[n] = \begin{cases} \dfrac{1}{N-m} \displaystyle\sum_{n=0}^{N-m-1} f^*[m]g[n+m] & \text{if } m \geq 0 \\ \dfrac{1}{N+m} \displaystyle\sum_{n=0}^{N+m-1} f^*[n-m]g[m] & \text{if } m < 0 \end{cases} \tag{A.47}$$

The difference between the biased and the unbiased version is apparent from figure A.3: both the biased and the unbiased cross correlations reaches a maximum when f and g are in phase, here illustrated by a sine (f) and a cosine (g). However, due the the scaling factor, the unbiased cross correlations are not sensitive to the change in overlap of the two functions.

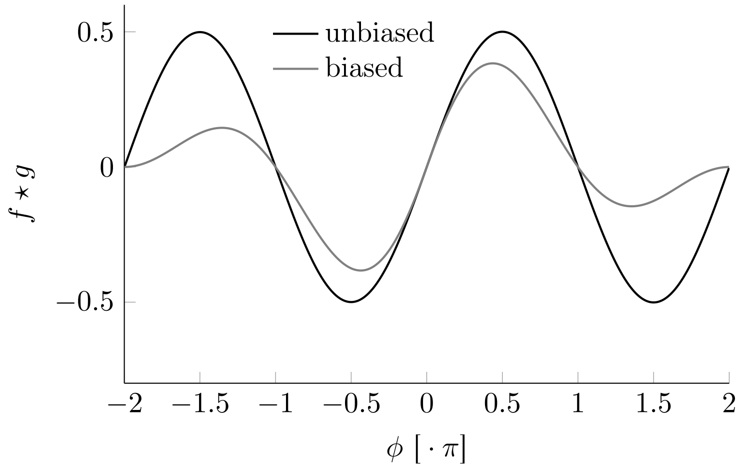

FIGURE A.3: Unbiased (black line) and biased (gray line) cross correlation of a sine and cosine function, defined in the domain $x \,\epsilon\, [0,\, 2\pi]$. The cross correlations are then defined in the domain $x \,\epsilon\, [-2\pi,\, 2\pi]$, i.e. the domain that there exists some overlap between the two functions. The unbiased cross correlation has equal maximums at both $\phi = \pi/2$ and $\phi = -3\pi/2$, where the functions are in phase. In contrast, the biased cross correlation has a smaller amplitude at $\phi = -3\pi/2$ than at $\phi = \pi/2$, due to the limited length of the functions.

A.3 Materials and methods

The materials used in this study was restricted to the 3D motion capture system described in chapter 3, and the inertial measurement unit described in chapter 4. The reader is referred to those chapter for details, but for the purpose of this validation study, some fulfilling information about the camera based system is presented here.

The reference frame used by the cameras was constructed using a proprietary metal frame with reflective markers (manufactured by Qualisys, Qualisys AB, Gothenburg, Sweden), which was placed on the treadmill when it was in a level position. The direction of the Y-axis was in the forward direction of the treadmill, the X-axis pointing sideways to the right (compared the the forward direction), and the Z-axis pointed vertically upwards. This assured that the XY-plane coincided with the horizontal plane. Any misalignments between the XY-frame used by the camera system and the horizontal plane, or the direction of the treadmill compared with the Y-axis, was considered negligible.

Only three of the retro reflective markers were used in this study: The sacrum marker (S1), which was placed on top of the IMU sensor housing (Figure A.5), and markers on the left and right anterior superior iliac spine (lASIS and rASIS. See Figure 2.2, page 9 for details on pelvis anatomy). The pelvis can be modelled as a rigid body. Hence, the S1, rASIS and lASIS could be used to define a local coordinate frame for the pelvis. The origin of this coordinate frame was at S1. The x-axis was parallel to the rASIS-lASIS vector, the y-axis passed through the rASIS-lASIS vector perpendicularly, and the z-axis was computed as the cross product of the x and y-axis. An illustration of this local coordinate frame is shown in figure A.4. The pelvis coordinate frame was then used to construct a direction cosine matrix, and the Euler angles $\boldsymbol{\theta} = (\theta_x, \theta_y, \theta_z)$ of the pelvis could be determined using eqations A.16. With the xyz rotation order, the angles corresponded to the pelvis tilt angle (θ_x), lateral tilt angle (θ_y) and pelvis rotation (θ_z). Figure 2.2, page 9 includes a illustration of the rotation axes.

In order to compare the velocity and acceleration computed from the IMU output, a numerical differentiation of the S1 position data had to be performed. For that reason, it was deemed necessary to low pass filter the position data. The filter used was a second order Butterworth filter with cutoff frequency 15 Hz. For the differentiation, a five point numerical approach[43] was used.

Synchronization

The camera system and the IMU did not support any direct synchronization of the signals, so a method to synchronize the two systems had to be developed. The start and stop of the

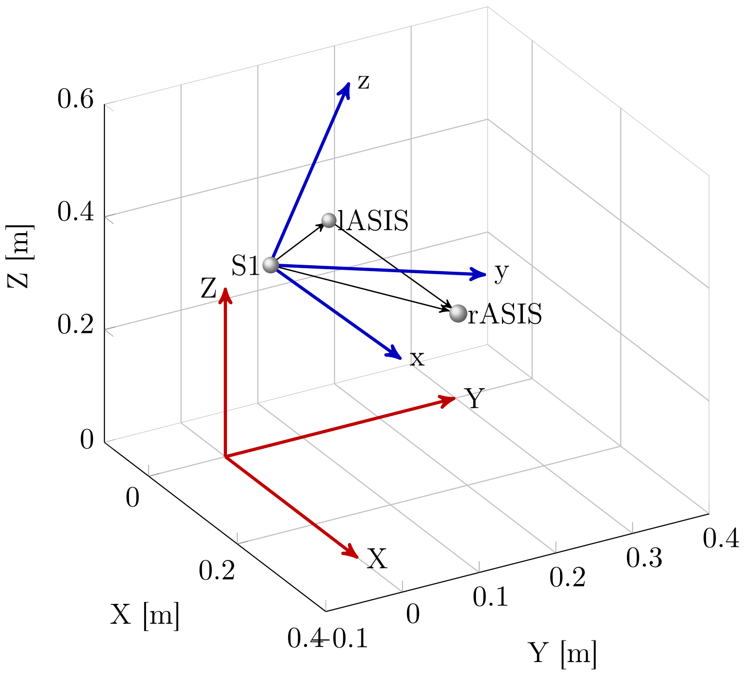

FIGURE A.4: Construction of the local pelvis coordinate frame. The x-axis was parallel to the rASIS-lASIS vector. The y-axis was in the S1-lASIS-rASIS plane, perpendicular to the x-axis. The z-axis was constructed to be mutually orthogonal to x and y-axis.

measurements was done manually, with estimated deviations between the two systems of $\sim 1\,\mathrm{s}$. In order to determine the synchronization error between the two systems, a method based on cross correlations was developed. The outline of the method was:

1. Differentiate the position of the S1 marker to find the acceleration ($\mathbf{a}_{\mathrm{S1}}$).
2. Add a component of gravity in the vertical direction ($\mathbf{f}_{\mathrm{S1}} = \mathbf{a}_{\mathrm{S1}} + \mathbf{g}$).
3. Calculate the vector norm of both the specific force measurement from the IMU ($|\mathbf{f}_{\mathrm{IMU}}|$), and the mimicked specific force measurement from the S1 marker ($|\mathbf{f}_{\mathrm{S1}}|$).
4. Re-sample the IMU-data to the camera system frame rate.
5. Cross correlate the two signals using equation A.47 (unbiased version) to find the time shift between the two signals.

One challenge with this method was the large variability in the clock frequency of the IMU (table 4.1). A variation in clock frequency of 1% was considered to give intolerable synchronization error. For this reason, points 4-5 above was repeated for many small variations in the sampling frequency of the IMU. This method allowed to determine both the synchronization error, and the sampling frequency of the IMU. A test of this method using controlled synchronization times and sample frequency deviations was performed.

The algorithm checked for variations in sample frequency in the range ±0.5%, using 501 equally spaced steps. From this test, the synchronization error was 0.007 ± 0.002 s, and the sampling frequency error was 0.01 ± 0.02 Hz. This was considered sufficient.

After the synchronization procedure, both signals where re-sampled to 100 Hz, which was close to the IMU original frequency. All inertial navigation calculations where done using data re-sampled to this frequency. This choice was made in order to have control of the actual sampling frequency (which appeared to vary slightly for the IMU), and to avoid using data up-sampled to a significantly higher rate than that at which the measurements where recorded.

IMU

Positioning: The IMU was adhered directly to the skin at the sacrum (S1, Figure 2.2) using a medical tape. It was oriented so that the axis pointed lateral to the right (x), anterior (y), and superior (z), as indicated in figure A.5.

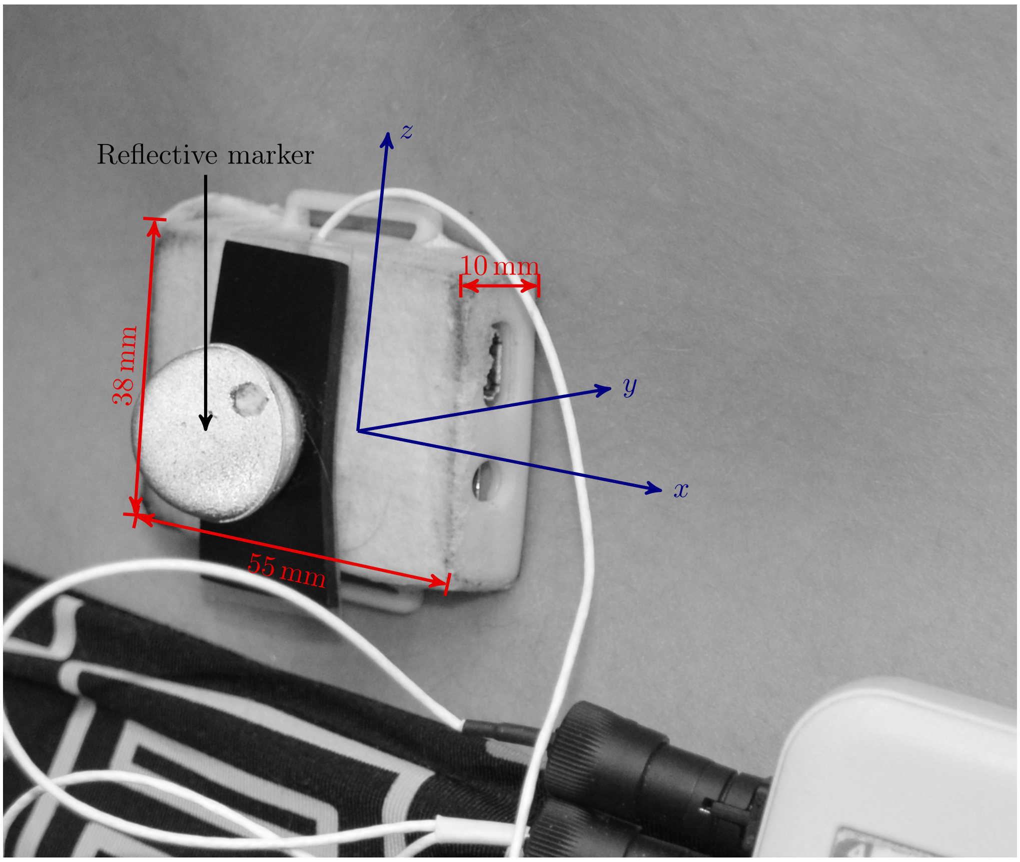

Figure A.5: Positioning of the IMU and S1 marker. The axis system indicates the direction of the IMU's axis. The wire going out from the IMU was from another accelerometer logging system, who's results is not used in this study.

Filtering: The output signals from the accelerometer and gyroscope where not filtered. An exception to this was the anti-aliasing filters applied during the re-sampling procedure under synchronization with the camera system. This decision was done based on the aim of this study, which was to mainly to investigate the validity of the displacement estimates. Since numerical integration by itself reduces high frequency noise, low pass filtering was considered unnecessary, along with the risk that all filtering corrupts the data to some degree.

Transformation to l-frame: In order to express the IMU measurements in the laboratory frame, a two step method was used. The first step consisted of correcting for the dynamic rotations caused by movement of the sensor during stride cycles. The second step was to align the axis of the fixed frame with the axis of the laboratory frame.

For the first step, the equations A.26 and A.30 was used. In order to determine the number of terms needed to compute $\mathbf{A}_k$ with sufficient accuracy, values for the maximal angular velocities during the measurements where put into equation A.36. The maximum angular velocity that the sensor measured during a typical stride cycle was $\sim 200^\circ/\mathrm{s}$. The estimated drift was then $< 0.1^\circ/\mathrm{s}$ for a first order algorithm , while a second order algorithm yielded a drift term $< 0.05^\circ/\mathrm{s}$. Over a typical measurement length of $\sim 20\,\mathrm{s}$, this corresponded to a drift of $< 2^\circ$ and $< 1^\circ$ respectively . These drift terms was considered to be small compared to the drift due to bias errors in the gyroscope measurement.

An error due to coning effect was calculated using estimates of $\theta_x = 15^\circ$, $\theta_y = 10^\circ$, $f = 1.5\,\mathrm{Hz}$ and $\phi = \pi/2$ in equation A.41. This resulted in an estimated orientation drift $< 1.1^\circ/\mathrm{s}$. These estimates were assumed to be worst case scenarios, however, it could not be ruled out that an error due the the coning effect would significantly influence the accuracy of the results.

With the drift estimates derived above, it was decided to do the calculations using two different algorithms: a first order algorithm without any coning correction term (denoted 1NCC), and a second order algorithm where a coning correction term was included (denoted 2CC). The rotation angle $\boldsymbol{\sigma}$ was in both cases computed by the trapeze method for numerical integration. In the non-corrected case, $\boldsymbol{\sigma}$ was considered equal to $\boldsymbol{\alpha}$ in equation A.40, while in the corrected algorithm, the correction term in equation A.39 was included.

In order to align the axis of the gyro stabilized frame with those of the laboratory frame, it was assumed that the yz-frame of the sensor frame would on average be aligned with the laboratory YZ-frame. The alignment of the two planes could then be achieved by calculating the Euler angles relating the body frame and the laboratory frame (eq A.16), subtracting the mean angles, and then calculating new direction cosines using these angles and equation A.15.

Since the laboratory XY-plane coincided with the horizontal plane, the xy-plane of the IMU needed to be aligned with the horizontal plane. This was done using the assumption that during the measurement time of twelve cycles ($\sim 20\,\mathrm{s}$), the mean acceleration that the IMU was subjected to was zero. This can be justified by (1) that the athletes are skiing at a constant speed, and (2) we take the mean over a whole number of stride cycles, so any variations in speed during a stride cycle should approximately cancel out. Under this assumption, the procedure outlined in section A.2.4 was valid, given that the instantaneous measurement of the specific force was replaced by the average over the measurement time. The angle around the x-axis could then be determined using equation A.22, and the IMU output could be rotated using the direction cosine $\mathbf{C}_x(\theta_x)$ given by equation A.11. The measurement of the specific force after this rotation was then put into equation A.12, giving the angle θ_y. Measurements in the gyro stabilized IMU frame could now be expressed in a frame that was aligned with the horizontal-plane via a the direction cosine:

$$\mathbf{C}_{sb}^{l} = \mathbf{C}_y(-\theta_y)\mathbf{C}_x(\theta_x) \tag{A.48}$$

where the index *sb* indicates a stabilized body frame.

Drift compensation: Under the assumption of a constant gyroscope bias error, the computed orientation of the gyro stabilized reference frame was considered to have a linear drift term. Since no real time computations was needed in this study, this linear drift was measured by calculating a linear fit to the Euler angles relating the body frame to the laboratory frame, and then subtracting the trend line.

The effect of the accelerometer bias error was reduced by imposing a constraint demanding that the acceleration of the sensor over the entire measurement period was zero.

Since there will always be some variation in the bias error, this assumption was only deemed adequate for the orientation computations. Because of the higher order drift terms in computing the velocity and displacement (equations A.44), the drift due to both accelerometer bias errors and gyroscope bias errors was considered to be to large if the integration was done over the entire measurement period of $\sim 20\,\mathrm{s}$. For that reason, it was decided to calculate the velocity and position over time intervals limited to the duration of each stride cycle. The velocity and position were calculated using equations A.21, where the integrals were evaluated using the trapeze method. The initial conditions $\dot{\mathbf{p}}(t_0)$ and $\mathbf{p}(t_0)$ were unknowns. This was solved by inferring two new assumptions: (1) The mean velocity was zero over each stride cycle, and (2) the mean position was zero over each stride cycle. The initial conditions were then found by first using initial values $\dot{\mathbf{p}}(t_0) = \mathbf{p}(t_0) = 0$, and then subtracting the mean velocity and displacement after the integrals were evaluated.

Calibration: The IMU was calibrated using a method proposed by Fong et al. [44]. The idea behind the method was to use the direction and magnitude of the gravity vector as a calibration constraint, both for the accelerometer and gyroscope calibration. The IMU was placed in 18 different orientations for a period of ~ 4 seconds. The accelerometer sensor could then be calibrated by minimizing the following cost function:

$$L_{\text{acc}}(\boldsymbol{\phi}_{acc}) = \sum_{k=1}^{18} \Big(1 - ||\mathbf{E}_{\text{acc}}(\mathbf{f}_k^b - \mathbf{b}_{\text{acc}})||^2\Big)^2 \tag{A.49}$$

where $\mathbf{f}_k^b$ was the mean specific force measurement from orientation k, $\mathbf{b}_{\text{acc}}$ was the accelerometer bias, and $\mathbf{E}_{\text{acc}} = \mathbf{MS}$ was the correction matrix, calculated from the scaling ($\mathbf{S}$, including cross axis terms) and axis misalignment matrices ($\mathbf{M}$):

$$\mathbf{S} = \begin{pmatrix} s_{xx} & s_{xy} & s_{xz} \\ s_{yx} & s_{yy} & s_{yz} \\ s_{zx} & s_{zy} & s_{zz} \end{pmatrix} \qquad \mathbf{M} = \begin{pmatrix} 1 & -\alpha_{yz} & \alpha_{zy} \\ 0 & 1 & -\alpha_{zx} \\ 0 & 0 & 1 \end{pmatrix}$$

The vector $\boldsymbol{\phi}_{\text{acc}}$ was made up of all the elements of the correction matrix $\mathbf{E}_{\text{acc}}$, and the bias vector $\mathbf{b}_{\text{acc}}$. The cost function L was minimized using the Nelder-Mead method for non-linear minimization. The calibration factors determined using this method gave the acceleration relative to the magnitude g of the local Earth gravitational field. In this study, g was set equal to $9.82\,\text{ms}^{-2}$.

The gyroscope bias vector $\mathbf{b}_{\text{gyro}}$ was calculated by averaging the output from a static measurement of duration 30 minutes. A correction matrix $\mathbf{E}_{\text{gyro}}$ was then calculated using a similar method as for the accelerometer. The cost function to be minimized was defined as:

$$L_{\text{gyro}}(\boldsymbol{\phi}_{\text{gyro}}) = \sum_{k=1}^{17} ||\mathbf{C}_k^{k+1}\mathbf{f}_k^b - \mathbf{f}_{k+1}^b||^2 \tag{A.50}$$

where $\mathbf{C}_k^{k+1}$ was the direction cosine relating body frame at orientation k to the body frame at orientation $k+1$. $\mathbf{C}_k^{k+1}$ was calculated using a second order strapdown integration algorithm (eq. A.30). The angular rate output from the sensors, denoted $\boldsymbol{\omega}_s^b$ was multiplied with the correction matrix $\mathbf{E}_{\text{gyro}}$, constructed in the same way as $\mathbf{E}_{\text{acc}}$. The resulting rates ($\boldsymbol{\omega}_c^b = \mathbf{E}_{\text{gyro}}\boldsymbol{\omega}_s^b$) where used as input to the strapdown orientation computations. The cost function was minimized using the same non linear minimization algorithm as above (Nelder-Mead), which resulted in a vector $\boldsymbol{\phi}_{\text{gyro}}$ where the entries made up the correction matrix $\mathbf{E}_{\text{gyro}}$

A.4 Results

Root mean square (RMS) and maximal (max) deviations between the position, velocity, acceleration and orientation calculated from the IMU output and the camera system are reported in tables A.1 and A.2. Entries in table A.1 are deviations for single stride cycles, while the results in table A.2 are obtained by first averaging over all twelve stride cycles, and then comparing the results. The latter method gave smaller deviations, since some of the random errors were reduced by the averaging.

In addition to the deviation along each axis, the Euclidean norm (denoted norm) is also reported. In the orientation estimates, the Euler angles relating the local pelvis coordinate frame to the lab frame is compared to the Euler angles relating the sensor frame to the lab frame.

Typical results from the IMU and camera system for one of the subjects is plotted in figures A.6 (displacement and velocity) and A.7 (acceleration and orientation).

The RMS deviation of the sensors displacement from the actual path (assumed to be represented correctly by the camera system) was $< 1.5\,\mathrm{cm}$ along the two horizontal axes, while it was $< 0.4\,\mathrm{cm}$ in the vertical direction. The maximal deviations where somewhat larger in magnitude, with the horizontal axes having values $< 4.5\,\mathrm{cm}$ and the vertical axis $< 1.0\,\mathrm{cm}$. If one is interested in only the average displacement over several strides, table A.2 shows that averaging over 12 strides reduced the deviation to $< 0.8\,\mathrm{cm}$ ($< 0.3\,\mathrm{cm}$ vertically) RMS, and $< 1.2\,\mathrm{cm}$ ($< 0.5\,\mathrm{cm}$ vertically) maximal deviation.

From tables A.1 and A.2, and figure A.7 (right panel), it appeared that the Euler angles relating the local pelvis frame to the lab frame differed to some degree from the Euler angles relating the IMUs orientation to the lab frame. This appeared to be especially apparent in the lateral tilt angle (θ_y), where the deviations were $\sim 2.5^\circ$ RMS ($\sim 5.5^\circ$ max). For comparison, the deviations between the axial rotation angles (θ_z) were $\sim 1^\circ$ RMS ($\sim 2^\circ$ max).

	Algorithm	RMS deviation				maximal deviation				unit
		X	Y	Z	norm	X	Y	Z	norm	
Displacement	1NCC	13 ± 6	12 ± 6	3 ± 1	19 ± 7	21 ± 11	20 ± 10	6 ± 3	36 ± 13	[mm]
	2CC	12 ± 6	12 ± 6	3 ± 1	19 ± 7	20 ± 12	21 ± 10	6 ± 2	35 ± 13	
Velocity	1NCC	41 ± 14	42 ± 15	18 ± 7	63 ± 18	94 ± 33	88 ± 32	44 ± 30	125 ± 45	[mm/s]
	2CC	37 ± 11	43 ± 15	17 ± 7	61 ± 16	86 ± 28	90 ± 32	43 ± 29	123 ± 44	
Acceleration	1NCC	67 ± 21	81 ± 23	58 ± 21	121 ± 35	220 ± 90	240 ± 90	200 ± 110	400 ± 150	[mg]
	2CC	67 ± 21	81 ± 23	57 ± 21	120 ± 35	220 ± 90	240 ± 100	200 ± 110	400 ± 150	
Orientation	1NCC	1.1 ± 0.3	2.6 ± 0.7	2.1 ± 0.6		1.9 ± 0.5	5.1 ± 1.6	3.8 ± 1.2		[degrees]
	2CC	1.1 ± 0.3	2.5 ± 0.6	2.0 ± 0.6		1.9 ± 0.5	4.8 ± 1.4	3.7 ± 1.1		

TABLE A.1: Deviations of kinetic variables between the IMU results and the camera system results. Left side: root mean square deviations, right side: maximal deviations. 1NCC mean results obtained by a first order algorithm with no coning correction, 2CC are results obtained by a second order algorithm with a coning correction term. The values are reported as the mean over all (132) measured stride cycles, ± the standard deviation

---

	Algorithm	RMS deviation				maximal deviation				unit
		X	Y	Z	norm	X	Y	Z	norm	
Displacement	1NCC	6.9 ± 2.1	7.7 ± 3.3	2.4 ± 0.8	10.8 ± 3.4	10.8 ± 3.7	11.3 ± 5.5	4.4 ± 1.5	16.8 ± 4.7	[mm]
	2CC	5.7 ± 1.3	7.7 ± 3.4	2.4 ± 0.8	10.1 ± 3.2	8.8 ± 2.1	11.3 ± 5.6	4.2 ± 1.5	16.5 ± 4.8	
Velocity	1NCC	32 ± 9	33 ± 12	14 ± 4	49 ± 14	75 ± 21	68 ± 26	31 ± 10	89 ± 25	[mm/s]
	2CC	29 ± 7	34 ± 13	13 ± 3	47 ± 13	67 ± 18	69 ± 27	31 ± 9	89 ± 27	
Acceleration	1NCC	35 ± 12	40 ± 14	30 ± 12	62 ± 21	98 ± 42	126 ± 65	91 ± 49	167 ± 75	[mg]
	2CC	35 ± 12	41 ± 14	30 ± 12	61 ± 21	97 ± 41	128 ± 65	92 ± 50	166 ± 75	
Orientation	1NCC	0.99 ± 0.27	2.52 ± 0.66	2.02 ± 0.58		1.69 ± 0.45	4.85 ± 1.45	3.58 ± 1.11		[degrees]
	2CC	0.99 ± 0.27	2.42 ± 0.57	1.96 ± 0.59		1.69 ± 0.44	4.57 ± 1.31	3.48 ± 1.09		

TABLE A.2: Deviations of kinetic variables between the IMU results and the camera system results. The results in this table are the deviations after averaging over all twelve stride cycles for each subject. Left side: root mean square deviations, right side: maximal deviations. 1NCC means results obtained by a first order algorithm with no coning correction, 2CC are results obtained by a second order algorithm with a coning correction term. The values are reported as the mean over all (11) measurements , ± the standard deviation

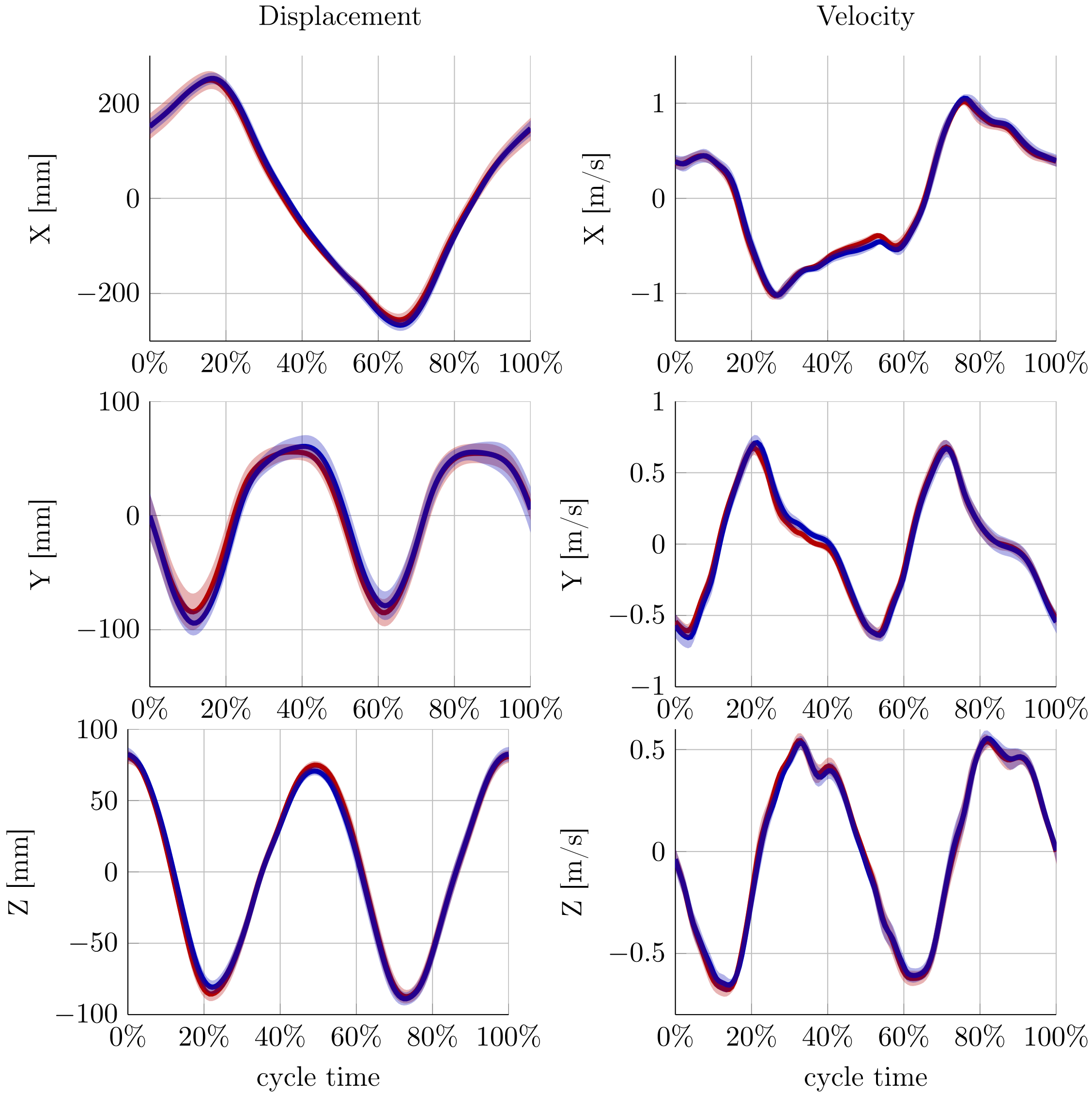

FIGURE A.6: Results of IMU computations for one of the subjects. Blue lines: IMU, red lines: Camera system. The results are the mean over 12 stride cycles, with the shaded area indicating the cycle-to-cycle variability. Left panel: displacement, right panel: velocity

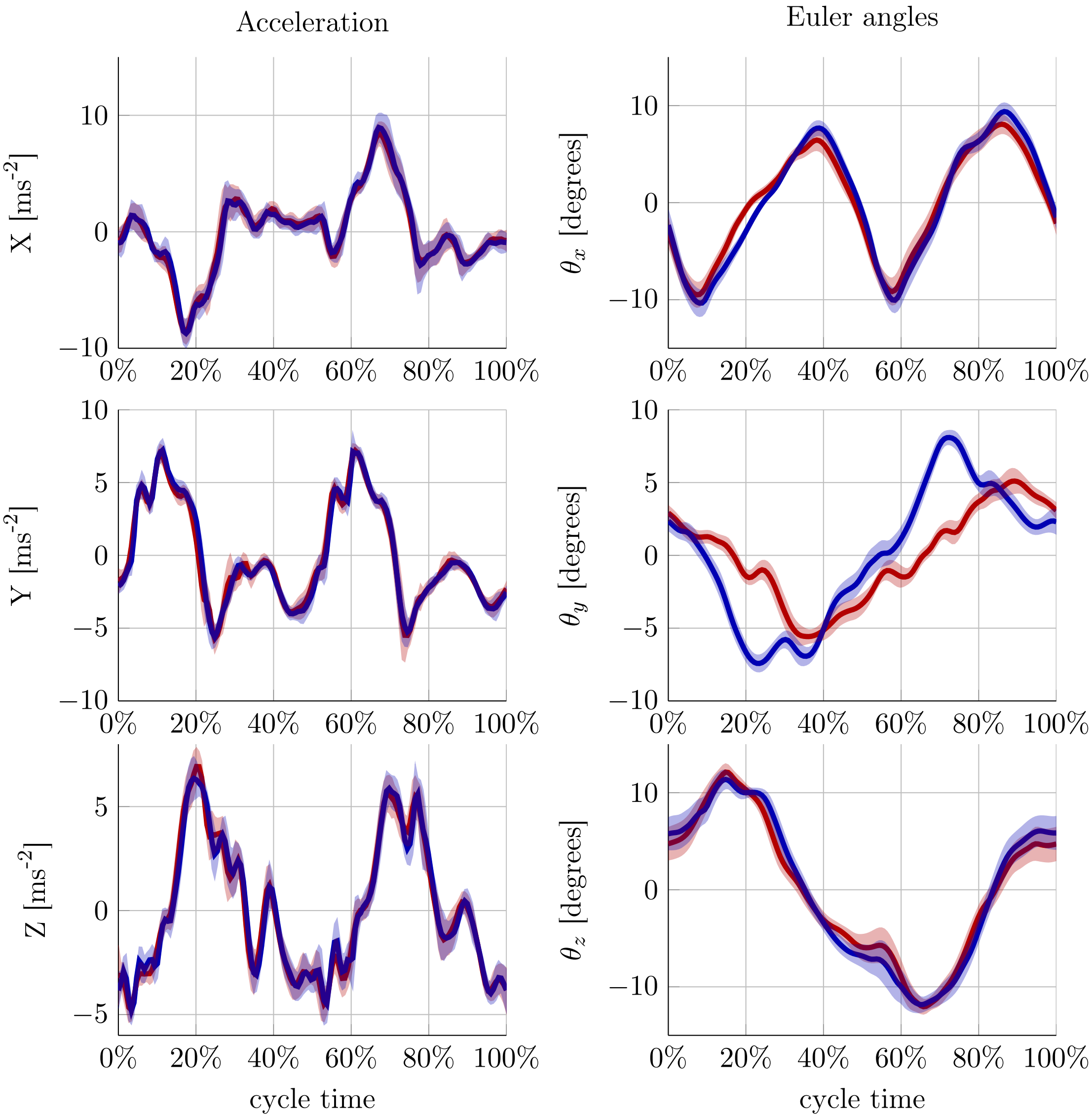

FIGURE A.7: Results of IMU computations for one of the subjects. Blue lines: IMU, red lines: Camera system. The results are the mean over 12 stride cycles, with the shaded area indicating the cycle-to-cycle variability. Left panel: acceleration, right panel: Euler angles

Tables A.1 and A.2 revealed minor differences in the results of the two different orientation algorithms that were used (1NCC and 2CC). Table A.3 show results of a direct comparison of the two algorithms. It appeared that the use of a higher order algorithm, with a coning correction term, did affect the results to a measurable degree. The effect of a higher order algorithm was most pronounced in the lateral (X) direction, with a reduction in the displacement deviation of -16.7% (RMS). The effect was more than twice as large at maximal effort compared to the sub maximal effort (-23.9% vs -10.0% respectively). The effect of the higher order algorithm on the anterior-posterior direction (Y) was not measurable, while the vertical direction was slightly improved at maximal intensity (-4.2%), but not at sub maximal intensity ($+0.1\%$)

Effort level	RMS deviation				maximal deviation			
	X	Y	Z	norm	X	Y	Z	norm
All	-16.7	0.4	-1.8	-6.8	-18.6	0.5	-4.3	-1.8
SUB	-10.0	0.0	0.1	-3.2	-15.3	-0.0	-2.1	-0.5
MAX	-23.9	1.1	-4.2	-11.5	-22.0	1.3	-6.1	-3.6

Table A.3: Percent-wise improvement of displacement calculations due to use of the 2CC algorithm rather than the 1NCC algorithm. All values are in %, minus signs mean a reduction in the deviation between the camera system and the IMU.

The relative deviations of the displacement, velocity and acceleration (i.e. divided by their range of motion) is presented in table A.4. It appeared that the relative deviation in the lateral and vertical direction was $< 3\%$ for all three kinematic variables. The anterior-posterior direction had somewhat larger relative deviations, where the largest deviations where found in the displacement calculations ($\sim 5\%$).

Kin. variable	Effort level	X [%]	Y [%]	Z [%]
Displacement	All	1.4 ± 0.2	5.1 ± 2.5	1.8 ± 0.7
	SUB	1.5 ± 0.3	6.0 ± 1.2	2.4 ± 0.4
	MAX	1.3 ± 0.3	4.2 ± 2.2	1.3 ± 0.8
Velocity	All	1.8 ± 0.4	2.8 ± 1.4	1.5 ± 0.5
	SUB	1.6 ± 0.4	2.9 ± 0.3	1.7 ± 0.2
	MAX	1.9 ± 0.4	2.7 ± 1.0	1.2 ± 0.4
Acceleration	All	2.3 ± 0.6	3.3 ± 1.0	2.6 ± 0.5
	SUB	2.1 ± 0.4	3.3 ± 0.5	2.4 ± 0.6
	MAX	2.4 ± 0.5	3.3 ± 0.7	2.7 ± 0.5

Table A.4: RMS deviations relative to the range of motion. The results was calculated using the mean over all stride cycles, using the 2CC algorithm. All: all trials, SUB: sub maximal effort trials, MAX: maximal effort trials

A.5 Discussion and conclusion

Displacement: It appears that in a controlled environment, the use of a low grade MEMS IMUs can give estimates of the displacement of an XC-skiers pelvis movement with an accuracy $< 1.5\,\text{cm}$ (RMS), or $< 0.8\,\text{cm}$ if it is sufficient to analyse just the mean over multiple strides. This accuracy is not as good as offered by 3D motion capture camera systems (which is typically some mm), but is sufficient to give high quality quantitative information about a skiers movement pattern. The findings is in agreement with the results reported by Floor-Westerdijk et al. [29] with respect to the accuracy of the sensor estimates. Also, they support the findings of Chardonnens et al. [33] and Dadashi et al. [35], who found that sub-INS quality sensors can give high quality measurements if the movements follows well defined constraints.

The accuracy of the displacement in the vertical direction was better than in the two horizontal directions. This difference is likely caused by the influence of gravity on the accelerometer measurements. This can be seen directly from equation A.44, or from a simple geometric consideration: the component of gravity affecting the vertical direction is proportional to $\cos(\delta\theta)$, with $\delta\theta$ being the misalignment error. In any horizontal direction, the component is proportional to $\sin(\delta\theta)$. For small misalignments, a 2. order Taylor expansion shows that the error due to misalignment with the vertical axis gives an error $\propto \delta\theta$ in the horizontal directions, while the error is $\propto \frac{1}{2}\delta\theta^2$ in vertical direction.

Velocity and acceleration: The velocity and acceleration can also be measured to a satisfactory degree using low grade MEMS sensors, with deviations $< 3.5\%$ compared to measurements made by a 3D motion capture system. However, due to numerical differentiation of the camera systems position estimates, it is not obvious what system offers the highest accuracy in these measurements.

Orientation: The orientation calculated by the IMU and the orientation from the camera system deviated by as much as 5° (maximal deviation). The deviations were largest in the θ_y-angle. Furthermore, some of the deviations appeared highly systematic (Figure A.7, right panel mid row). This suggest that some systematic error caused a misalignment between the sensor frame and the sacrum-rASIS-lASIS frame. In the author's opinion, the most likely cause of this is skin movement. The reflective markers where not anchored to the bony landmarks, which compromised the model of the pelvis as a rigid body. Furthermore, the IMU was also subject to skin movement. Arguably, the IMU axis of rotation that was most susceptible for this type of error was the y-axis, i.e. the axis directed perpendicular to the skin surface. This was also the axis where we observed the largest deviations.

Although the two coordinate frames do not align perfectly, the use of gyroscopic measurements from a sensor positioned at the S1 appear to give interesting information about the skier pelvis orientation.

A.5.1 Sources of error and improvements

The major sources of error when calculating the displacement of the sensor was considered to be the bias of the measurements from both the accelerometer and gyroscope sensors. For that reason, some heavy constraints were imposed on the system. These constraints where necessary to reduce drift, but they also reduced the sensitivity to large deviations from an average stride cycle. For instance, the largest deviation of the displacement measures during all measurements was 9 cm, which is almost 5 times larger than the typical maximal deviation. It is likely that errors this large was due to stride cycles that did not follow the imposed constraints.

A source of error that was not attempted corrected in this study was the misalignment angle between the direction of the treadmill (the Y-axis), and the direction of the sensor y-axis. It was assumed that this error was small, both due to the sensor housing having a relatively large flat side which was adhered directly to the skin, and that the skier would on average align his pelvis with the direction of travel. For future studies, the first error might be accounted for by having the subject perform some controlled motion. Some early tests have been performed where the subjects has been instructed to do a double poling motion, i.e. a movement that is restricted to the sagittal plane. The results of this method seem promising, however, since the subjects involved in this study did not do this kind of calibration movement, the error have to remain uncorrected.

The influence of temperature changes on the sensor output will also contribute to errors in the IMU calculations. However, it is apparent from table 4.1 that the scale factors change relatively little with temperature. The bias is more sensitive to change in temperature, but because of the precautions taken to compensate for sensors bias errors, the effect of temperature on the results is not considered a dominant factor.

Conclusion

It is possible to obtain high quality, drift free estimates of displacement using low cost IMUs, if (1) the movement pattern that is analysed is cyclic with periods $\sim 2\,\mathrm{s}$, and (2) the average velocity is constant from cycle to cycle. The light weight and small size of the sensors make in-competition measurement a possibility, and the low cost make sensors readily available.

Appendix B

Inertial sensors in smartphones

B.1 Introduction

Results presented earlier in this thesis suggests a single IMU, consisting of an accelerometer and a gyroscope, might provide measurements that capture interesting aspects of skiing technique. It has also been pointed out that these sensors are incorporated in current market smart phones, which suggests that skiers, both recreational and athletes, can measure their own skiing technique without the need for further equipment. This appendix investigates the validity of such a claim.

Several master theses at the University of Oslo have in the recent years investigated the possibility for inertial navigation using smart phones. Hamra [45] developed an application for logging of sensor data on an Android platform, which formed the basis for the theses of Kyllo [46], Mugisha [47], Lefoka [48]. The last three theses included measurements from a deterministic track generator, where the accuracy of the measurements could be assessed. The focus of all thesis were to model the sensor noise using Kalman filters. They report substantial improvements in the accuracy of position and velocity estimates by this approach.

The approach used in this appendix differ from that of the theses mentioned above, and instead builds on a priori knowledge of constraints that govern the system, similar to the approach in appendix A. However, the basic idea is the same: to analyse a system that moves in a deterministic manner, which enables an assessment of the accuracy of the method. Instead of a track generator, the phone was suspended from strings to make a simple pendulum.

B.2 Theory

This section will outline the equations that govern the movement of a simple pendulum, and deduce an analytical solution for measurements of specific force. For INS theory, the reader is referred to section A.2.

B.2.1 Pendulum dynamics

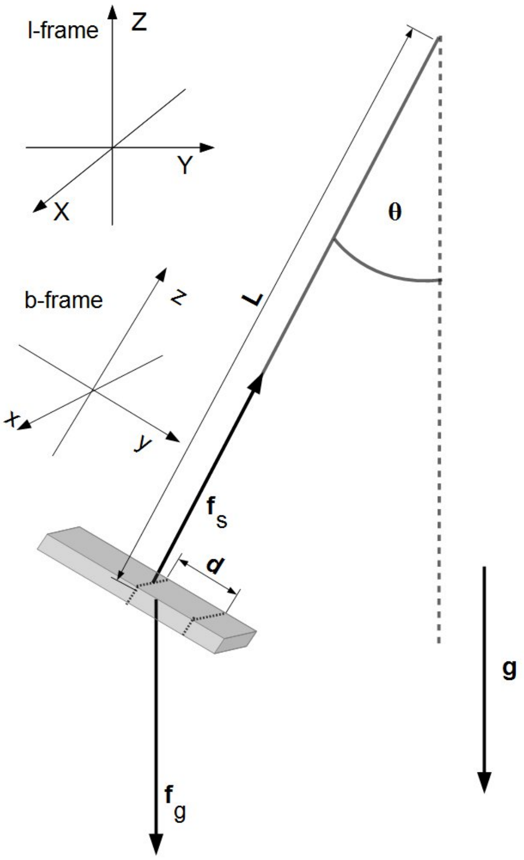

FIGURE B.1: Free body diagram showing the forces on the pendulum. The orientation of the body coordinate frame of the pendulum bob (b-frame), and the laboratory coordinate frame (l-frame) are illustrated for clarity.

We will consider the case of a simple pendulum, i.e. a pendulum bob of some point mass M, a massless and rigid pendulum rod of length L, and a frictionless suspension point. Furthermore, any effect of air resistance is neglected. A free body diagram of such a pendulum is found in Figure B.1. The movement of such a pendulum follows the differential equation

$$\ddot{\theta} + \frac{g}{L}\sin\theta = 0 \tag{B.1}$$

For small angles $\theta << 1$ (in radians), then $\sin\theta \approx \theta$. Under this assumption, equation B.1 reduces to that of a simple harmonic oscillation[49, page 436], which has a simple, closed form solution. With initial conditions of $\theta = \theta_0$ and $\dot{\theta} = 0$, the solution to equation B.1 is:

$$\theta(t) = \theta_0 \cos\left(\sqrt{\frac{g}{L}}t\right) \tag{B.2}$$

With the solution for $\theta(t)$ in equation B.2, and the geometry made apparent in Figure B.1, the position of the pendulum bob in the laboratory frame is easily obtained: [1]

$$\mathbf{x}^l = \begin{pmatrix} 0 \\ L\sin\theta \\ L(1-\cos\theta) \end{pmatrix} \tag{B.3}$$

By differentiation we also obtain the velocity and acceleration of the pendulum bob:

$$\dot{\mathbf{x}}^l = \begin{pmatrix} 0 \\ L\dot{\theta}\cos\theta \\ L\dot{\theta}\sin\theta \end{pmatrix} \tag{B.4}$$

$$\ddot{\mathbf{x}}^l = \begin{pmatrix} 0 \\ -(g\cos\theta + L\dot{\theta}^2)\sin\theta \\ (g\cos\theta + L\dot{\theta}^2)\cos\theta - g \end{pmatrix} \tag{B.5}$$

B.2.2 Specific force measurements

From Figure B.1 it is readily verified that the specific force[2] in the b-frame xy-plane is equal to zero, because the movement is not restricted in this plane. This is not the case along the z-axis, where both a component of gravity[3], and the centripetal acceleration term $L\dot{\theta}^2$ is acting. Hence, the specific force vector in the body frame is given by:

$$\mathbf{f}^b = \begin{pmatrix} 0 \\ 0 \\ g\cos\theta + L\dot{\theta}^2 \end{pmatrix} \tag{B.6}$$

---

[1] Here the origin is defined to be the position of the bob in the $\theta = 0$ position. This does not correspond to the axis system in Figure B.1, which is meant to indicate only the direction of the axes.

[2] The term specific force is outlined in chapter A.2

[3] More specifically, a component of the earth's force against gravity

Under the assumption that the yz plane is aligned with the YZ plane, a transformation between the b-frame and the l-frame can be be obtained by a left multiplication of the direction cosine $\mathbf{C}_x$ (equation A.11). Writing out the result, we find:

$$\mathbf{f}^l = \begin{pmatrix} 0 \\ -(g\cos\theta + L\dot{\theta}^2)\sin\theta \\ (g\cos\theta + L\dot{\theta}^2)\cos\theta \end{pmatrix} \tag{B.7}$$

As expected, the specific force in the laboratory frame (eq. B.7) is equal to the acceleration of the pendulum bob in the laboratory frame (eq. B.5) after subtraction of the gravity vector $\mathbf{g} = (0,\, 0,\, g)^T$.

B.2.3 Correction terms

If the sensing elements are not positioned at the center of mass (COM) of the pendulum bob, the analytical solutions derived in the previous sections will not be valid. This section will outline correction terms to account for the situation where the sensing elements are displaced some distance d along the y-axis of the b-frame (Figure B.1). We denote the correction terms $\mathbf{\Delta}$, $\dot{\mathbf{\Delta}}$, and $\ddot{\mathbf{\Delta}}$, so that the corrected solutions are:

$$\begin{aligned} \mathbf{x}_s &= \mathbf{x} + \mathbf{\Delta} \\ \dot{\mathbf{x}}_s &= \dot{\mathbf{x}} + \dot{\mathbf{\Delta}} \\ \ddot{\mathbf{x}}_s &= \ddot{\mathbf{x}} + \ddot{\mathbf{\Delta}} \end{aligned} \tag{B.8}$$

It is readily verified from simple geometry that the correction terms for $\mathbf{x}_s^l$ in the laboratory reference frame (denoted with a superscript ^{l}) are:

$$\mathbf{\Delta}^l = \begin{pmatrix} 0 \\ d\cos\theta \\ d\sin\theta \end{pmatrix} \tag{B.9}$$

By differentiation we also obtain correction terms for the velocity and acceleration:

$$\dot{\mathbf{\Delta}}^l = \begin{pmatrix} 0 \\ -d\dot{\theta}\sin\theta \\ d\dot{\theta}\cos\theta \end{pmatrix} \tag{B.10}$$

$$\ddot{\mathbf{\Delta}}^l = \begin{pmatrix} 0 \\ -d\left(\ddot{\theta}\sin\theta + \dot{\theta}^2\cos\theta\right) \\ d\left(\ddot{\theta}\cos\theta + \dot{\theta}^2\sin\theta\right) \end{pmatrix} \tag{B.11}$$

B.3 Materials and methods

The materials used for this experiment was a smart phone (Samsung Galaxy Nexus GT-I9250), some thin string, a yardstick and a laser level. A commercial logging software that enabled logging of sensor output (SensorInsider version 3.1.1), and a toolbox that included an accelerometer based level application (Smart Tools version 1.4) was installed on the phone. Included in the hardware of the phone was a MEMS accelerometer (Bosch BMA 250) and a MEMS gyroscope (Invensense MPU-3050). Key sensor specifications from the manufacturers are reproduced in table B.1.

TABLE B.1: Nexus sensor specifications

Gyroscope			
Full scale range		± 2000	[°/s]
Scale factor sensitivity		16.4	[LSB/(°/s)]
Scale factor variation	−40°C to +85°C	±2	[%]
Bias variation	−40°C to +85°C	± 0.03	[°/s/K]
Total RMS noise		0.1	[°/s]
Noise spectral density	at 10 Hz	0.01	[°/s/$\sqrt{\text{Hz}}$]
Nonlinearity	Best fit straight line, 25°C	0.2	[%]
Cross-Axis Sensitivity		± 2	[%]
Sample frequency†		1 (8)	[kHz]
Accelerometer			
Full scale range		± 2	[g]
Scale factor sensitivity		256	[LSB/g]
Scale factor variation	−40°C to +85°C	±0.02	[%/K]
Bias		± 80	[mg]
Bias variation	−40°C to +85°C	± 1	[mg/K]
Noise spectral density		0.8	[mg/$\sqrt{\text{Hz}}$]
Nonlinearity	Best fit straight line	0.5	[%FS]
Cross-Axis Sensitivity		± 1	[%]
Sample frequency†		2	[kHz]

† The sampling frequency used in these experiments where limited by the Android operating system software. This is described in detail later in the text

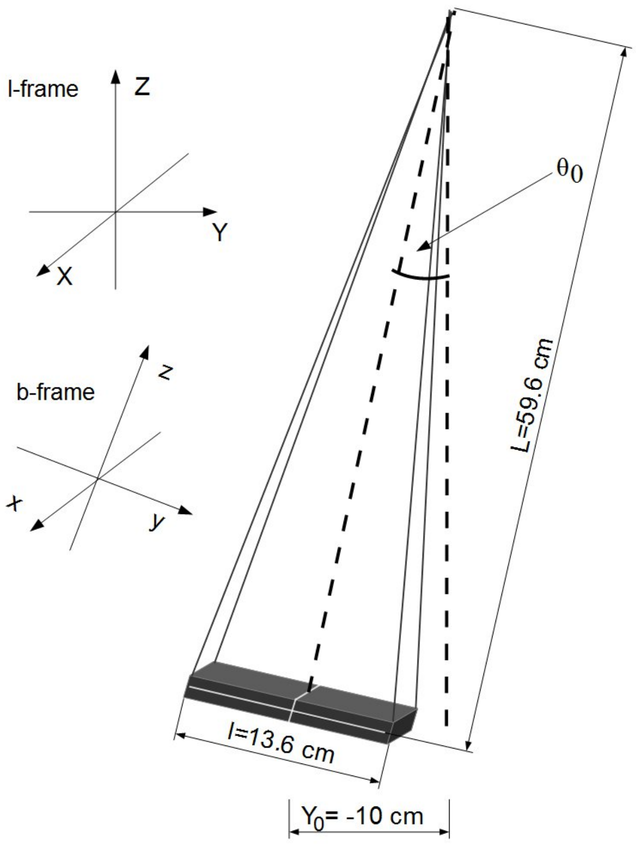

Figure B.2: Experimental setup of the pendulum.

B.3.1 Experimental setup

The phone was suspended from two strings, which were fitted so that the display-side of the phone was always perpendicular to the (ideal) pendulum rod (Figure B.2). Since the exact COM of the phone was unknown, the length of the idealized rod (L) was approximated with distance from the point of suspension to the center of the phone in the yz-plane, indicated with the crossing of two white lines in Figure B.2. This length was measured with a yardstick.

The position of accelerometer chip on the phones circuit-board was not known. However, a teardown of the phone[4] revealed that the most distal chips were positioned approximately 4 cm from the center in the y-direction. This corresponded to a maximal possible displacement $d = 4\,\text{cm}$ (Figure B.1) of the sensing element compared to the center line indicated in Figure B.2. Correction terms based on this value were estimated using equations B.9-B.11, and resulted in "worst case" solutions.

---

[4] http://www.ifixit.com/Teardown/Samsung+Galaxy+Nexus+Teardown/7182

The initial displacement in the y-direction was measured by mounting a laser level at the point of suspension, and a measuring the distance along the ground with a yardstick. This was done to ensure a starting angle of approximately 10°. This accuracy of this method was estimated to be only within $\pm 1\,\mathrm{cm}$. For this reason, the value of θ_0 that was used in the analytical solutions was instead determined from the gyroscopic output. Specifically, θ_0 was defined to be the half of the range of motion of the angle θ_x, averaged over the analysed periods of the pendulum.

Due to software limitations, it was not possible to set an exact sample frequency for the inertial sensors. Instead, a minimum time interval between samples of $dt = 0.01\,\mathrm{s}$ was selected.

The pitch and roll of the phone in the $\theta = 0$ position was both measured by a level application on the phone to be $< 1.1^\circ$, and is considered negligible.

B.3.2 Data analysis

The sensor data was exported into Matlab, which was used for all data analysis. First, the sensor data was interpolated to obtain measurements sampled at a constant rate of 100 Hz. This was done because the logging software did not support logging at an exact sample rate. Second, the data was passed through an algorithm that detected each time the pendulum passed the $\theta = 0$ position. This algorithm worked by low pass filtering the gyroscope output with a second order, zero lag Butterworth filter with cutoff frequency 5 Hz. The heavily filtered data was submitted to a peak detection algorithm[5]. It is obvious from equation B.2 that the angular velocity $\dot{\theta}$ has a maximum in the $\theta = 0$ position. Hence, the peaks of the low pass filtered ω_x (i.e. the angular rate about the sensor x-axis) determined the time points of each complete pendulum period. A total of 10 complete pendulum periods were submitted to further analysis.

The orientation of the phone, described by the Euler angles θ_x, θ_y, θ_z was calculated with a xyz rotation sequence, using the 2. order algorithm with the coning correction terms described in appendix A. As in appendix A, drift in the orientation estimates was reduced by subtraction of the linear trend line of the Euler angles. The initial conditions were set by subtracting the average orientation angles, so that the time average of the b-frame was aligned with the l-frame.

The acceleration, velocity and displacement in the inertial reference frame (which was assumed to coincide with the laboratory frame) was also calculated by a method equivalent to the method in appendix A: The average acceleration over all 10 pendulum periods was

---

[5] Matlab's findpeaks() was used for this purpose

first subtracted. Then a numerical integration using the trapeze method was performed for each pendulum period. The initial conditions for each period were determined by the assumption that both the average velocity and the average displacement were zero during each pendulum period.

The experimental data was not filtered, and no calibration of the sensor output was performed.

B.4 Results

The gyroscope estimate for the initial angle of the pendulum was $\theta_0 = 10.9 \pm 0.2°$. A comparison of specific force measurements from the accelerometer to the theoretical solution based on θ_0 and equation B.6 is presented in Figure B.3.

The phase space of θ for a pendulum in the small angle approximation makes an ellipse[6]. In Figure B.4 this is used to assess the orientation measurements. θ_x is plotted versus the angular rate ω_x^b (multiplied with the constant $\sqrt{L/g}$), which theoretically (under the small angle assumption) should form a circle.

The performance of the position, velocity, acceleration and orientation estimates are summarized in table B.2. This table reports the RMS deviations of the experimental estimates from the theoretical solutions in equations B.2-B.5. Figures B.5 and B.6 compare the same material graphically.

---

[6] This should be apparent from equation B.2, along with its time derivative.

Table B.2: RMS deviations between theoretical solution and experimental results

	Displacement [mm]		**Velocity** [mm/s]		**Acceleration** [mg]		**Orientation** [°]	
X	2.0 ± 0.7	(1.8)	9 ± 3	(7.3)	10.0 ± 0.4	(4.4)	0.49 ± 0.02	(0.47)
Y	5.4 ± 1.4	(5.1)	24 ± 5	(22)	13.8 ± 0.5	(9.5)	0.14 ± 0.01	(0.14)
Z	1.8 ± 0.8	(1.5)	9 ± 3	(6.2)	10.1 ± 1.1	(4.3)	0.32 ± 0.01	(0.31)
norm	6.1 ± 1.5	(5.6)	27 ± 5	(24)	19.9 ± 0.5	(11.0)		

Root mean square deviations between the theoretical COM solution (eq B.2-B.5) and experimental results. The results are reported as the mean over all pendulum periods ± the period-to-period standard deviation. Values in parenthesis are RMS deviations between the theoretical solution and the pendulum trajectory averaged over all (10) periods.

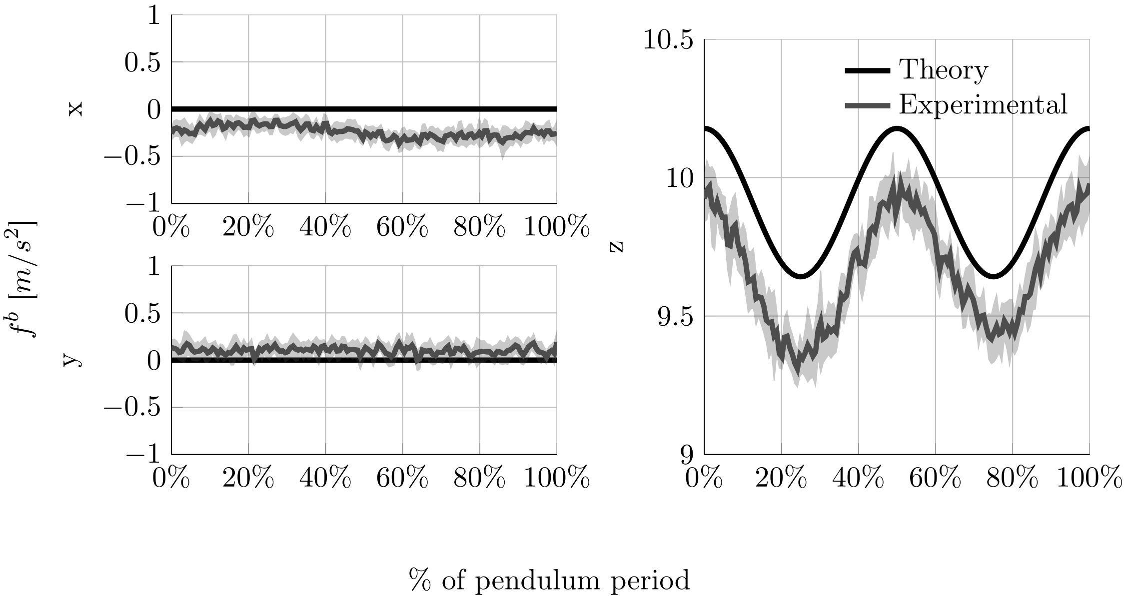

Figure B.3: Specific force measurements from the accelerometer during pendulum motion (gray line). Shaded area indicates the period-to-period std. Black line: theoretical solution for specific force measurements at the COM of the phone.

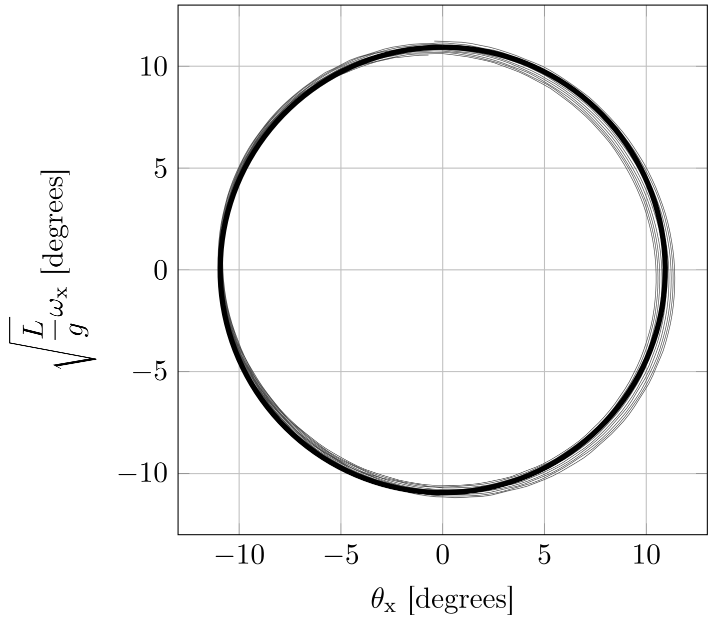

Figure B.4: Phase space of pendulum. Black line: theoretical solution, which forms a circle. Gray lines: Experimental samples from the 10 analysed pendulum periods.

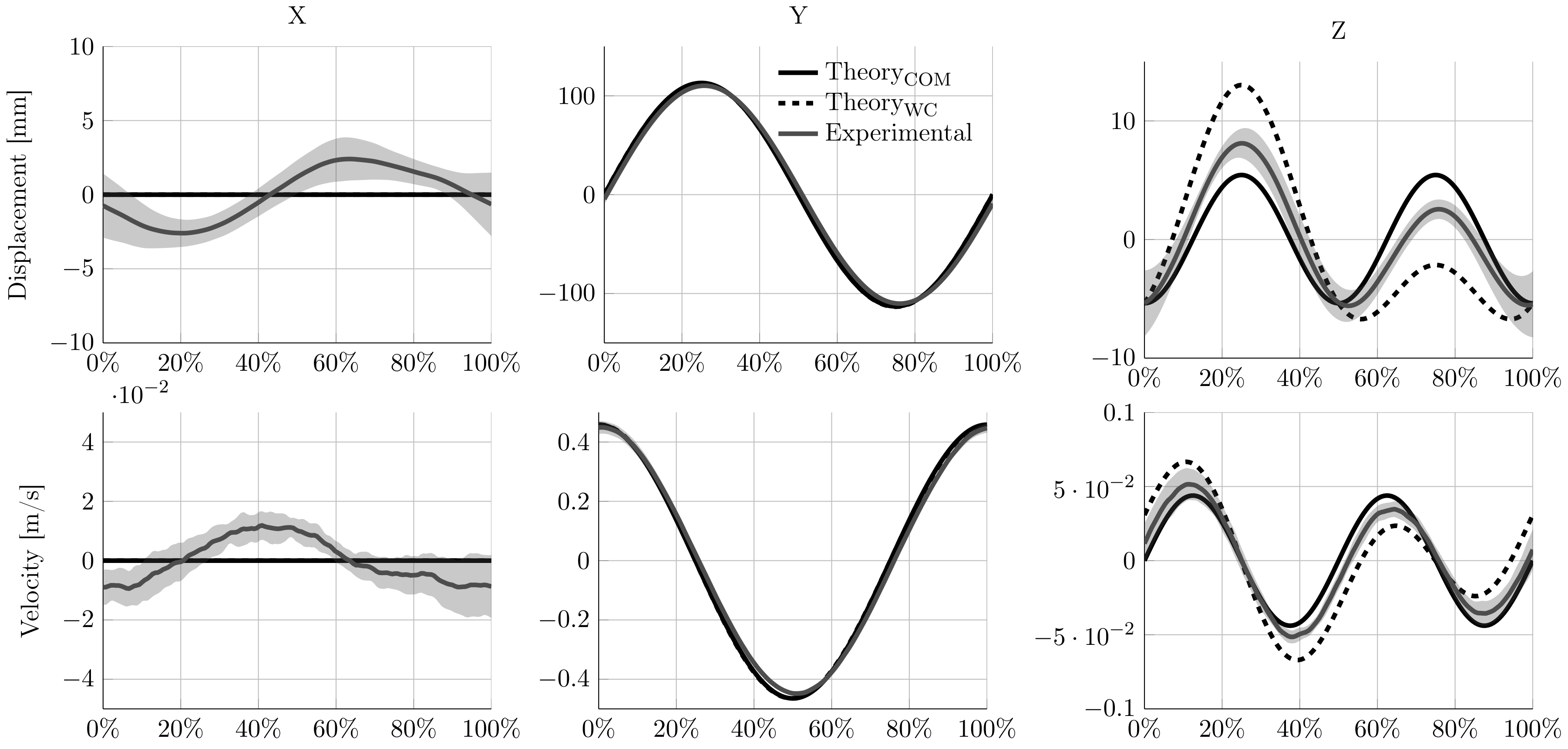

FIGURE B.5: Results of INS calculations: Displacement (top row) and velocity (bottom row). Black lines: theoretical solutions for COM (solid) and ”worst case” (WC, dotted). Gray lines represent the average over all (10) pendulum periods, the shaded area represents the period-to-period deviation (std)

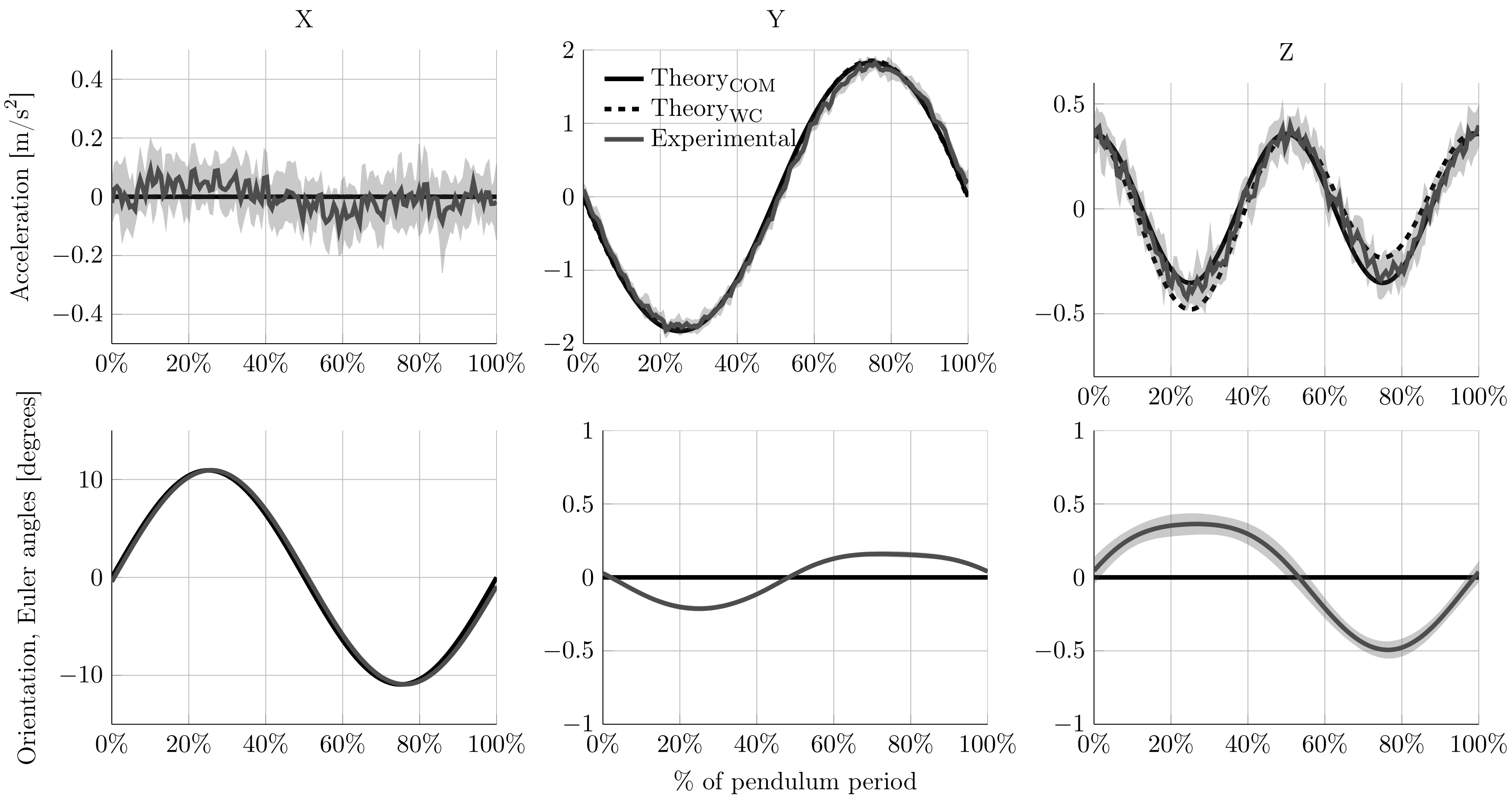

Figure B.6: Results of INS calculations: Acceleration (top row) and orientation (bottom row). Black lines: theoretical solutions for COM (solid) and "worst case" (WC, dotted). Gray lines represent the average over all (10) pendulum periods, the shaded area represents the period-to-period deviation (std)

B.5 Discussion and conclusion

The results of these experiments show that we can obtain high accuracy, drift free measurements of velocity and displacement from the MEMS inertial sensors incorporated in current market smart phones, given prior knowledge of the movement. We observed an accuracy similar to that obtained by the dedicated system described in appendix A, although the quality of the phone sensors had lower specifications than the dedicated system (table B.1 vs 4.1). However, some challenges were also revealed.

One challenge was that the positioning of the accelerometer chip on the phones circuit board. It is apparent from Figure B.5 that for small displacements, the exact position of the sensing element influenced the result substantially. An accurate determination of the accelerometer chip in the particular phone used in this experiment would have enabled a better assessment of the sensor performance. However, the aim of this experiment was to investigate the use of smart phones to measure detailed movement patterns. The unknown position of the sensing elements in then an inherent weakness in such analysis. Hence, an accurate determination of the sensing element was not considered relevant to investigate the aim of the study.

Another challenge appeared to be limitations in the software. The logging application was not able to log data at a constant rate. This problem was caused by either the logging application, or restrictions within the Android operating system. If the latter is the case, it might pose difficulties for the type of calculations presented in this appendix.

Although the challenges mentioned above show that there are some limitations by using sensors incorporated in smart phones rather than a dedicated system, it still appears possible to obtain interesting measurements with such a system. In fact, an application has been developed for the Apple IOS platform that utilizes the inertial sensors included in the Iphone to give feedback on XC skiing double poling technique (SmartSki, SmartSki Technologies AS, www.smartski.tictail.com).

It is evident from Figure B.3 that the sensor output deviated substantially from the theoretical model. Hence, a calibration of the sensors to obtain better estimates of the scale factors and offsets, for instance using the method suggested by Fong et al. [44], would likely have improved the results.

Conclusion

Inertial sensors in smart phones have the potential to give decent quality measurements of displacement (deviations of a few cm) and other kinematic variables, given that measured movement follows well defined constraints. The use of these types of sensors for integrated, on phone analysis appear feasible, but needs to overcome difficulties with uneven sampling frequency, and unknown sensor locations.

Bibliography

[1] Adrian Lees. Technique analysis in sports: a critical review. *Journal of Sport Sciences*, 20:813–828, 2002.

[2] Øyvind Sandbakk, Hans-Christer Holmberg, Stig Leirdal, and Gertjan Ettema. Metabolic rate and gross efficiency at high work rates in world class and national level sprint skiers. *European Journal of Applied Physiology*, 109:473–481, 2010.

[3] Thomas Losnegard, Håvard Myklebust, Matt Spencer, and Jostein Hallén. Seasonal variations in vo2 max, o2-cost, o2-deficit, and performance in elite cross-country skiers. *Journal of Strength and Conditioning Research*, 27(7):1780–1790, 2013.

[4] Roger Bartlett, Jon Wheat, and Matthew Robins. Is movement variability important for sports biomechanists? *Sports Biomechanics*, 6(2):224–243, MAY 2007. ISSN 1476-3141. doi: 10.1080/14763140701322994.

[5] Marcel R. Boulay, Olivier Serresse, Natalie Almeras, and Angelo Tremblay. Energy expenditure measurement in male cross-country skiers: comparison of two field methods. *Medicine and Science in Sports and Exercise*, 26:248–253, 1993.

[6] Bernhard Bilodeau, Marcel R. Boulay, and Benoit Roy. Propulsive and gliding phases in four cross-country skiing techniques. *Medicine and science in sports and exercise*, 24(8):917–925, 1991.

[7] Hans-Christer Holmberg, Stefan Lindinger, Thomas Stöggl, Erich Eitzlmaier, and Erich Müller. Biomechanical analysis of double poling in elite cross-country skiers. *Medicine and Science in Sports and Exercise*, 38(5):807–818, 2005.

[8] Hans-Christer Holmberg, Stefan Lindinger, Thomas StÖGgl, Glenn Bjorklund, and Erich Müller. Contribution of the legs to double-poling performance in elite cross-country skiers. *Medicine and Science in Sports and Exercise*, 1825-1860, 2006.

[9] Johnny Nilsson, Per Tveit, and Olav Eikrehagen. Effects of speed on temporal patterns in classical style and freestyle cross-country skiing. *Sports Biomechanics*, 3:85–108, 2007.

[10] Johnny Nilsson, Fredrik Tinmark, Kjartan Halvorsen, and Anton Arndt. Kinematic, kinetic and electromyographic adaptation to speed and resistance in double poling cross country skiing. *European Journal of Applied Physiology*, 113:1385–1394, 2013. doi: DOI10.1007/s00421-012-2568-5.

[11] Thomas Stöggl and Hans-Christer Holmberg. Force interaction and 3d pole movement in double poling. *Scandinavian Journal of Medicine & Science in Sports*, 21:393–404, 2011.

[12] Stefan Josef Lindinger, Caroline Gopfert, Thomas Stöggl, Erich Müller, and Hans-Christer Holmberg. Biomechanical pole and leg characteristics during uphill diagonal roller skiing. *Sports Biomechanics*, 8(4):318–333, 2009.

[13] H Myklebust, T Losnegard, and J Hallén. Differences in v1 and v2 ski skating techniques described by accelerometers. *Scandinavian journal of medicine & science in sports*, 2013. doi: 10.1111/sms.12106.

[14] Gerald A. Smith. Biomechanical analysis of cross-country skiing techniques. *Medicine and Science in Sports and Exercise*, 24(9):1015–1022, 1992.

[15] Anne Waugh and Allison Grant. *Ross and Wilson Anatomy and Physiology in Health and Illness.* Elsevier, 11 edition, 2010.

[16] Andreas Daffertshofer, Claudine J.C. Lamoth, Onno G. Meijer, and Peter J. Beek. PCA in studying coordination and variability: a tutorial. *Clinical biomechanics*, 8: 415–428, 2004.

[17] Nikolaus F. Troje. Decomposing biological motion: A framework for analysis and synthesis of human gait patterns. *Journal of Vision*, 2:371–387, 2002.

[18] P. Federolf, R. Reid, M. Gilgien, P. Haugen, and G. Smith. The application of principal component analysis to quantify technique in sports. *Scandinavian Journal of Medicine and Science in Sports*, pages doi: 10.1111/j.1600–0838.2012.01455.x, 2012.

[19] Kerstin Witte, Nico Ganter, Christian Baumgart, and Christian Peham. Applying a principal component analysis to movement coordination in sport. *Mathematical and Computer Modelling of Dynamical Systems*, 16(5):477–488, 2010. doi: 10.1080/13873954.2010.507079. URL `http://dx.doi.org/10.1080/13873954.2010.507079`.

[20] David C. Lay. *Linear Algebra and Its Applications.* Pearson Education, third edition, 2006.

[21] Peter Federolf, Lilian Roos, and Benno M. Nigg. Analysis of the multi-segmental postural movement strategies utilized in bipedal, tandem and one-leg stance as quantified

by a principal component decomposition of marker coordinates. *Journal of Biomechanics*, 46(15):2626–2633, 2013.

[22] Rules for FIS cross-country points, 2013-2014. URL `http://www.fis-ski.com/mm/Document/documentlibrary/Cross-Country/04/26/74/FISpointsrules2013-2014_finalversion_inclattachments_English.pdf`.

[23] Peter Andreas Federolf. A novel approach to solve the ”missing marker problem” in marker-based motion analysis that exploits the segment coordination patterns in multi-limb motion data. *Plos One*, 8:e78689– e78689, 2013. doi: 10.1371/journal.pone.0078689.

[24] Wilfrid Taylor Dempster and George R. L. Gaughran. Properties of body segments based on size and weight. *American Journal of Anatomy*, 120:33–54, 1967.

[25] Rolf Moe-Nilssen and Jorunn L. Helbostad. Estimation of gait cycle characteristics by trunk accelerometry. *Journal of Biomechanics*, 37:121–126, 2004.

[26] Jay L. Devore and Kenneth N. Berk. *Modern Mathematical Statistics with Applications*. Cengage Learning, 2007.

[27] Daniel Roetenberg, Henk Luinge, and Per Slycke. Xsens mvn: Full 6dof human motion tracking using miniature inertial sensors. Technical report, 2009. URL `www.xsens.com`.

[28] Matej Supej. 3D measurements of alpine skiing with an inertial sensor motion capture suit and gnss rtk system. *Journal of Sports Sciences*, 28:759–769, 2010.

[29] Marianne J Floor-Westerdijk, H Martin Schepers, Peter H Veltink, Edwin HF van Asseldonk, and Jaap H Buurke. Use of inertial sensors for ambulatory assessment of center-of-mass displacements during walking. *Biomedical Engineering, IEEE Transactions on*, 59(7):2080–2084, 2012.

[30] Justin J Kavanagh and Hylton B Menz. Accelerometry: a technique for quantifying movement patterns during walking. *Gait & Posture*, 28(1):1–15, 2008.

[31] Rolf Moe-Nilssen. A new method for evaluating motor control in gait under real-life environmental conditions. part 1: The instrument. *Clinical Biomechanics*, 13:320–327, 1998.

[32] Rolf Moe-Nilssen, Mona Kristin Aaslund, Caroline Hodt-Billington, and Jorunn L. Helbostad. Gait variability measures may represent different constructs. *Gait & Posture*, 32:98–101, 2010.

[33] Julien Chardonnens, Julien Favre, Florian Cuendet, Gerald Gremion, and Kamiar Aminian. A system to measure the kinematics during the entire ski jump sequence using inertial sensors. *Journal of Biomechanics*, 46:56–62, 2013.

[34] Julien Chardonnens, Julien Favre, Florian Cuendet, Gerald Gremion, and Kamiar Aminian. Characterization of lower-limbs inter-segment coordination during the take-off extension in ski jumping. *Human Movement Science*, 32:741–752, 2013.

[35] Farzin Dadashi, Farzin Dadashi, Gregoire P. Millet, and Kamiar Aminian. Front-crawl instantaneous velocity estimation using a wearable inertial measurement unit. *Sensors*, 12:12927–12939, 2012. doi: 10.3390/s121012927.

[36] Fazle Sadi and Richard Klukas. New jump trajectory determination method using low-cost mems sensor fusion and augmented observations for gps/ins integration. *GPS solutions*, 17(2):139–152, 2013.

[37] Finn Marsland, Keith Lyons, Judith Anson, Gordon Waddington, Colin Macintosh, and Dale Chapman. Identification of cross-country skiing movement patterns using micro-sensors. *sensors*, 12:5047–5066, 2012.

[38] M.H.A. Eames, A. Cosgrove, and R. Baker. Comparing methods of estimating the total body centre of mass in three-dimensions in normal and pathological gaits. *Human Movement Science*, 18:637–646, 1999.

[39] David Titterton and John Weston. *Strapdown Inertial Navigation Technology*. Radar, Sonar and Navigation Series. The Institution of Engineering and Technology, 2. edition, 2004.

[40] Jacob Fraden. *Handbook of Modern Sensors*. Springer, 3. edition, 2004.

[41] Roy B. Davis, Sylvia Ounpuu, Dennis Tyburski, and James R. Gage. A gait analysis data collection and reduction technique. *Human Movement Science*, 10:575–587, 1991.

[42] Paul G Savage. Strapdown system algorithms. AGARD Lecture Series No. 133, 'Advances in strapdown inertial systems', May 1984.

[43] Morten Hjorth-Jensen. Computational physics. Compendium used in FYS3150 at the University of Oslo, 2013.

[44] WT Fong, SK Ong, and AYC Nee. Methods for in-field user calibration of an inertial measurement unit without external equipment. *Measurement Science and Technology*, 19(8):085202, 2008.

[45] Sami Hamra. Treghetsnavigasjon implementert i android. Master's thesis, University of Oslo, 2011.

[46] Hågen Kyllo. Treghetsnavigasjon med smarttelefon. Master's thesis, University of Oslo, 2012.

[47] Diego Mugisha. Tns med lavkostsensorer. Master's thesis, University of Oslo, 2012.

[48] Petter Moagi Lefoka. Analyse av treghetsnavigasjons systemer. Master's thesis, University of Oslo, 2013.

[49] Hugh D. Young and Roger A. Freedman. *University Physics*. Pearson International Education, 12 edition, 2008.